August 2009

ISSN 1211—877X

CZECH AEROSPACE Proceedings

LETECKÝ zpravodaj

In this issue:

No. 2 / 2009

CZECH
AEROSPACE
Proceedings

JOURNAL FOR CZECH AEROSPACE RESEARCH

LETECKÝ
zpravodaj

Editorial address:
Aeronautical Research and Test Institute / VZLÚ, Plc.
Beranových 130, 199 05 Prague 9, Letňany
Czech Republic
Phone.: +420-225 115 223, Fax: +420-869 20 518

Editor-in-Chief: Ladislav Vymětal (e-mail: vymetal@vzlu.cz)
Editor & Litho: Stanislav Dudek (e-mail: dudek@vzlu.cz)

Publisher:
Czech Aerospace Manufacturers Association / ALV, Prague
Beranových 130, 199 05 Prague 9, Letňany
Czech Republic
ID. No. 65991303
Printing: Studio Winter Ltd. Prague

Periodicity: Three times per year. Press Reg. No. MK ČR E 181312.

Subscription and ordering information available at the editorial address. Legal liability for published manuscripts' originality holds the author. Manuscripts contributed are not returned automatically to authors unless otherwise agreed. Notes and rules for the authors are published at our Internet pages http://www.vzlu.cz/.

Czech AEROSPACE Proceedings
Letecký zpravodaj
2/2009

ISSN 1211 - 877X

Contents / Obsah

Calculation of Temperature Fields of Vibrating Composite Parts

Výpočet teplotních polí kmitajícího kompozitního dílu

Ing. Vilém Pompe, Ph.D. / VZLÚ, Plc., Prague, Aircraft Propellers Dept.

Composite parts vibrating on a resonant frequency produce heat which can be recorded by an infrared camera. The thermographs obtained have various forms of exploitation, e.g. inspection of local temperatures, contact free identification of natural vibration modes or selection of optimal location of strain gauges.

The thermographs are not always available and a theoretical analysis is necessary. FEM analysis and a set of experimental data can be used. A new computational method is tested using data obtained from measurements on composite propeller blades.

Kompozitní díl kmitající na rezonanční frekvenci produkuje teplo, které lze zachytit termovizní kamerou. Obdržené termogramy je pak možno využít k různým účelům, například pro kontrolu lokálních teplot, nebo pro bezkontaktní identifikaci vlastních tvarů kmitání, či k výběru vhodných míst pro instalaci tenzometrů.

V některých případech nelze získat termografické snímky a je nezbytné nahradit je výpočtem. K tomu je možno využít výsledky MKP výpočtu a materiálové konstanty, které jsou získávány experimentální cestou. Výpočtová metoda je v současnosti testována s využitím výsledků experimentu provedeného na kompozitních vrtulových listech.

Keywords: composite, temperature fields, FEM, thermographs, vibrations, propeller, blade.

1 Introduction

The heat-up of a vibrating body is a notorious phenomenon which may be put to various uses. Energy supplied for the vibration is attenuated, converted into heat, and it leaves the volume of the vibrating body through its surface. The escaping heat can be recorded by means of a thermographic camera and the obtained information can subsequently be assessed using an appropriate method.

For example, the comparison of thermographs of various bodies is typically used to disclose certain inherent defects. There are thermographic methods applied to assess the state of tension of bodies and, no less importantly, to assess local heat-up, which might prove critical for certain material groups. The Aeronautical Research and Test Institute also employ thermography as the method of contactless identification of natural vibration modes of composite propeller blades and optimization of the number and location of strain gauges for their modal testing during rotation.

One specifically problematic group comprises fatigue tests of composite parts (either simple samples or structural units, etc.) that have to take place at high deflection amplitudes and high testing frequencies. Potential spontaneous heat-up may pose the risk of overheating of the composite matrix and occurrence of irregular defect. This will cause distortion of the results, which can be avoided using appropriate combination of the testing frequency and the maximum deflection amplitude.

Symbols

ΔQ, Δq	Heat increase, specific heat increase	[J, J/kg]
C, c	Heat capacity, specific heat capacity	[J/K, J/kg.K]
ΔT	Temperature variation	[K, deg. C]
m	Mass	[kg]
ΔU	Strain energy increment	[J]
S	Area	[m², mm²]
t	Thickness	[m, mm]
ρ	Density	[kg/m³]
ξ	Loss coefficient	[1]
F	Active force	[N]
K	Stiffness	[N/m, N/mm]
Δl	Deflection, amplitude of deflection	[m, mm]
FEM	Finite Element Method	

Description of the Method

For the purposes of material heating, the following relation between heat and temperature is assumed (see e.g. [1]):

$$\Delta Q = C \cdot \Delta T \tag{1}$$

In order to deal with laminate material composed of individual monolayers the relation (1) has to be modified so that heat capacity of the laminate element is expressed as the sum of the capacities of the individual layers:

$$\Delta Q = \Delta T \cdot \sum_{i=1} c_i \cdot m_i \tag{2}$$

Relation (2) transcribed for one kilogram of material using area "S" of element "e" of the FEM mesh, thickness and density of individual monolayers:

$$\Delta q = \Delta T \cdot \frac{S_e \cdot \sum_{i=1}^{n} c_i \cdot t_i \cdot \rho_i}{m_e} \tag{3}$$

From which the specific heat capacity of the laminate element is derived as:

$$c_e = \frac{S_e \cdot \sum_{i=1}^{n} c_i \cdot t_i \cdot \rho_i}{m_e} \tag{4}$$

The value required for heating of one element can be expressed as:

$$\Delta Q_e = c_e \cdot m_e \cdot \Delta T_e \tag{5}$$

The vibrating body is deformed and accumulates mechanical energy one part of which is converted into heat through the process of loss. For the sake of simplicity we will limit ourselves to natural vibration modes and the corresponding frequencies.

Within one period the analyzed element "e" reaches two amplitudes, therefore it can be assumed that the corresponding heat loss relates to double amount of the value of the

maximum contained strain energy:

$$\Delta Q_e \approx 2 \cdot \Delta U_e \tag{6}$$

The escaped heat is assumed to be the multiple of this value, expressed as the loss coefficient:

$$\Delta Q_e = \xi \cdot 2 \cdot \Delta U_e \tag{7}$$

The relation (7) is incorporated in (5) and the change in temperature is expressed depending on material characteristics and strain energy of the element as:

$$\Delta T_e = \frac{2 \cdot \xi}{c_e \cdot m_e} \cdot \Delta U_e \tag{8}$$

The relation (8) yields a value corresponding to the steady state of the vibrating component. It does not depend on anisotropy directions, symmetry or balance of the composition of the laminate.

We will also want to convert the change in steady temperature fields depending on the change of the deflection amplitude. It is theoretically possible to determine the specific heat capacity and the density of each layer; however, it is problematic to provide the mathematical expression of the loss coefficient . The relation (8) may be simplified as:

$$\Delta T_e = A_e \cdot \Delta U_e \tag{9}$$

Constant of a particular laminate composition can be determined using a thermo camera; and provided the specific heat capacity, density and thickness of the layers are known even the loss coefficient ξ may be separated. These characteristics will be considered to be the material constants independent of deflection, frequency and temperature.

The conversion of temperature fields in relation to the height of deflection amplitude will be made using the following calculation of the proportion of strain energy on the element depending on the deflection ratio:

$$\Delta U_2 = \Delta U_1 \cdot \left(\frac{\Delta l_2}{\Delta l_1} \right)^2 \tag{10}$$

By incorporating relations (9), (10), reference temperature and experimentally measured temperature increment at a nominal deflection (amplitude) we can roughly calculate the new temperature for new nominal deflection of the system as follows:

$$T_2 = T_{ref} + \Delta T_{\exp} \cdot \left(\frac{\Delta l_2}{\Delta l_{\exp}} \right)^2 \tag{11}$$

Experimental Part

For the purposes of verification of the proposed temperature field calculation method a number of thermographic measurements of the vibrating composite propeller blade VZLÚ V45 took place. For the first three natural vibration modes a sequence of three amplitude heights at a reference point has been determined. The deflection amplitude was measured using a contactless laser sensor. The propeller blade was clamped in a special vibrator-activated fixture, and the effects of ambient temperature fields were partially eliminated by means of an insulating box. Fig.1 shows the measurement configuration, Figs. 2 and 3 represent an example of a thermograph and a corresponding FEM analysis. The configuration of the experimental part is based on results in [2].

Table 1 shows an example of the comparison of a thermograph with FEM analysis provided for the three most significant points. The VZLÚ V45 blade was excited to reach the third natural vibration mode and a thermograph of the suction side at reference amplitudes of 2, 4 and 6 mm was subsequently taken. The aim was to verify the applicability of the relation (11) for the conversion of temperature fields and to compare the measurement results with the theoretical calculation according to (8).

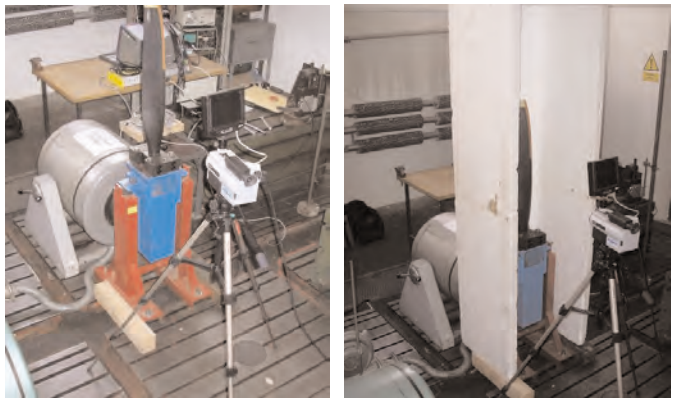

Fig. 1 — Composite propeller blade mounted in a special fixture for excitation of the first three natural vibration modes. The thermographs were taken using a thermal insulating box

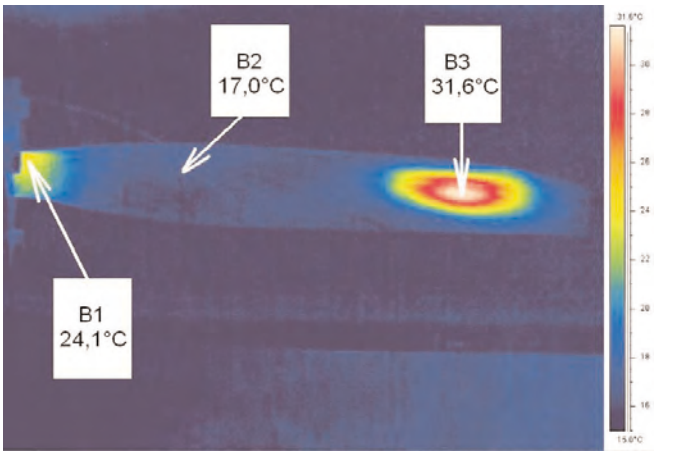

Fig. 2 — Thermograph of the third natural vibration mode, suction side of the blade VZLÚ V45

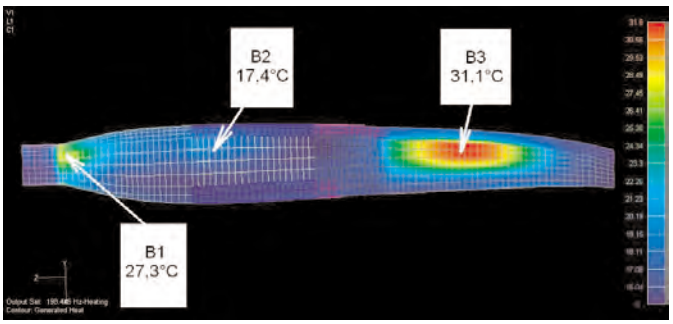

Fig. 3 — FEM analysis of thermal fields of the third natural vibration mode, suction side of the blade VZLÚ V45

Table 1 — Comparison of thermography results and the conversion of FEM results of the third natural vibration mode

Reference amplitude [mm]	2			4 (see Fig. 2 and 3)			6		
Point of temperature reading	B1	B2	B3	B1	B2	B3	B1	B2	B3
Thermography*	17.5	16.7	19.1	24.1	17.0	31.6	36.3	19.1	45.2**
FEM	19.3	16.8	20.1	27.3	17.4	31.1	43.7	21.6	51.3

*) Thermo camera FLIR SC-2000, resolution 0.1° C, -40 to +1500° C (three ranges), error ±2%.

**) The maximum measured temperature of 50.1° C i.e. a value much closer to FEM. has been detected in the close proximity.

Currently, no loss coefficients or specific heat capacities of individual layers, which at the same time represent the material function and volume fractions of the individual composite constituents, are available. Their measurement, or identification of an effective method of determination, will be subject to further development. At present, temperature fields are being calculated based on the FEM modal analysis and a reference thermograph using the following formula:

$$T_2 = T_{ref} + A \cdot \Delta U_{FEM} \cdot \left(\frac{\Delta l_2}{\Delta l_{\exp}} \right)^2 \qquad (12)$$

Conclusion

The method of calculation of temperature fields presented in this document is currently in the stage of experimental verification. The final aim of the researcher is to generalize this method so that it can be applied to any periodic mechanical load imposed on a composite material, i.e. not only in the case of natural vibration modes.

Furthermore, it is necessary to devise practically applicable methods of determination of requisite material constants. As concerns specific heat capacities it may be assumed that their values are calculable. Loss coefficients will presumably draw on empirical data obtained from measurements of typical material systems incorporating the effect of volume fraction of the individual composite constituents.

This paper has been drawn up as part of the research project MSM0001066904 *"Research in behaviour of composite materials in the primary structure of devices based on the principle of rotating lifting surface"*.

References

[1] Kmoníček, B., Sazima, M., Středa, I., Doubrava, J.: *Termomechanika*; Praha, ČVUT, 1987

[2] Andrýsek, V., Pompe, V.: *Metodika pro umístění tenzometrů při modálních zkouškách vrtulových listů*; Praha, VZLU Report R-4110, 2007

NASPRO 3.0 – Software Tool for Transformation and Vizualization of Aircraft Structure Modal Analysis Results

NASPRO 3.0 – programový prostředek pro transformaci a vizualizaci výsledků modální analýzy leteckých konstrukcí

Ing. David Gallovič, Ing. Jiří Čečrdle, Ph.D. / VZLÚ, Plc., Prague

The submitted paper presents a new software tool NASPRO 3.0 aimed at transformation and visualization of the aircraft modal characteristics. The mode shapes are visualized in the specific graphic format, which demonstrates in an appropriate way modal deformations of different structural parts, controls and tabs of the aircraft, phase shift relations and node lines positions. It is useful for direct visual comparison of analytical and experimental mode shapes, assessment of the mode shapes changes in the parametric analytical studies and during preparation of the ground vibration test and flight flutter test of the aircraft structure.

Předkládaný článek představuje nově vytvořený programový prostředek NASPRO 3.0, určený pro transformaci a vizuální zobrazení modálních charakteristik u leteckých konstrukcí. Pro zobrazení vlastních tvarů je použit specifický grafický formát, zobrazující vhodným způsobem deformace jednotlivých konstrukčních částí, řídicích ploch a plošek, fázové poměry a polohy uzlových čar. Uvedené zobrazení je vhodné pro vizuální srovnání analytických a experimentálních výsledků, vyhodnocení vlivů změn parametrů na modální charakteristiky u analytických studií a pro přípravu pozemní rezonanční zkoušky a letových flatrových zkoušek letecké konstrukce.

Keywords: aeroelasticity, ground vibration tests, mode shapes, node lines, NASPRO.

1 Introduction

Determination of the aircraft modal characteristics is an integral part of the aircraft certification process. Modal characteristics, it means natural frequencies, mode shapes, generalized masses and damping ratios of modes are important input data for evaluation of the aircraft aeroelastic (flutter) stability. Modal characteristics are investigated either experimentally or numerically. At VZLU, the NASTRAN FE - based system is used for numerical simulations. NASTRAN includes an aeroelastic module, which allows analyzing the aircraft aeroelasticity, in fact, with no limitation. For the experimental modal investigations, the PRODERA system is used. It allows harmonic or impulse excitation in 8 points and measuring structure response in 500 points.

2 Motivation

Standard commercial postprocessing tools integrated into FE systems offer tools like modal animations or axonometric visualization via deformed, fringe or vector plots for mode shapes visualization. However such visualization isn't sufficient for aircraft structures. Even the use of correlation criteria like MAC is problematic for identification of specific modes in some cases. For purposes of visual presentation, comparison,

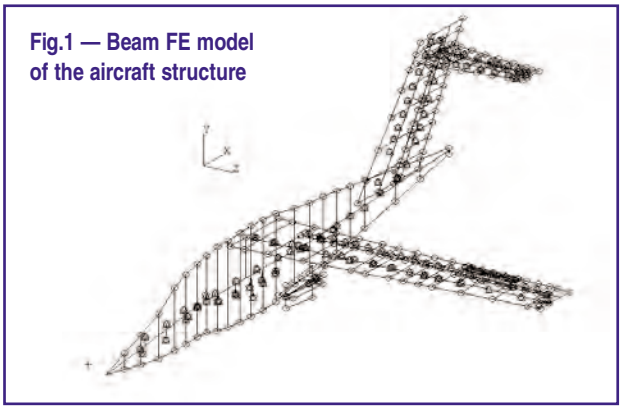

Fig.1 — Beam FE model of the aircraft structure

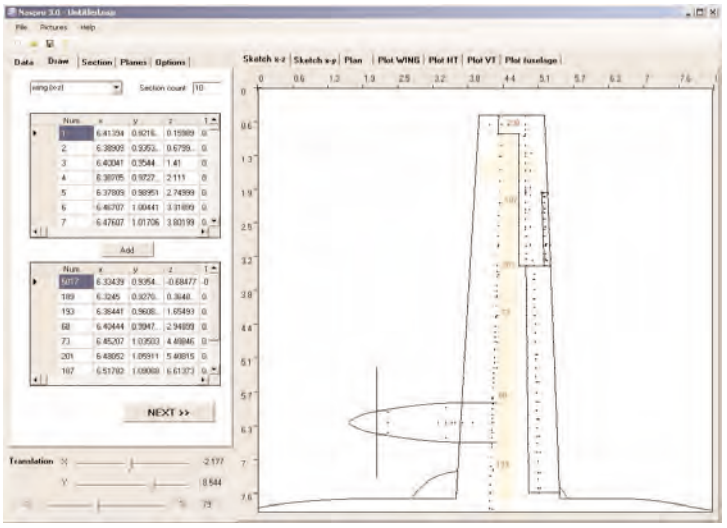

Fig. 2 — Program window - selection of nodes

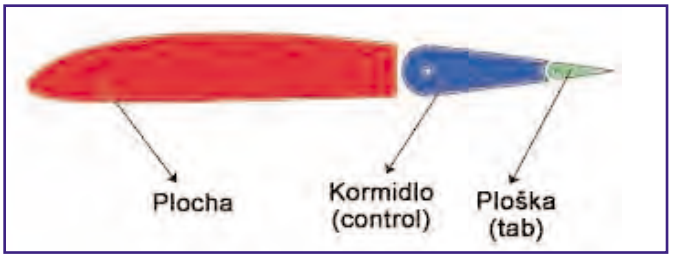

Fig. 3 — Types of structural parts (surface - control - tab)

assessment of differences and changes, a specific graphic format has been created [1]. This graphic standard demonstrates in an appropriate way modal deformations of different structural parts, controls and tabs of the aircraft, phase shift relations and the node lines positions. It is a standard output of the ground vibration tests (GVT) performed by the VZLU modal test laboratory. Therefore it is possible to use it for the direct visual comparison of analytical and experimental mode shapes. Such kind of analytical shapes visualization is useful in the preparation phase of GVT. The knowledge in the mode shapes and locations of the node lines is important for the appropriate emplacement of exciters and accelerometers during GVT. The node lines position is also required for the calculations of control surface dynamic balancing with respect to the other main mode shapes. Besides, it is also important for the preparation of flight flutter tests (FFT) for appropriate emplacement of the impulse rocket exciters, since the design of exciters installation usually precedes the GVT. Finally the visualization format is useful for assessment of the mode shapes changes in the parametric analytical studies as well.

For this purpose, the SW tool named NASPRO 2.0 has been developed in the early nineties. The program, built by the Turbo Pascal operated on the MS.DOS operating system. However, this tool is unserviceable today. Moreover, the source code is not at disposal, therefore any improvement is impossible. The new SW tool NASPRO 3.0 replaces this obsolete tool.

3 Program Description

The name of the program (NASPRO) is assembled from the words NAStran and PROdera. The program is assigned for the postprocessing of the modal analysis of the aircraft structure beam FE model (see Fig. 1) performed by means of the NASTRAN program system, solution 103 (normal modes). The program input is a NASTRAN text output file (*.f06 file) and the *.dxf graphic files with the aircraft geometry (plan view, side view). The program is divided into several parts. The part ”draw“ is assigned for selection of the FE model nodes, which are used for the transformation of the modal deformations (see Fig. 2). The part ”section“ is assigned for definition of sections, which the deformations will be pictured in. The part ”planes“ is assigned for the definition of the structural parts, controls and tabs and their reference axes. The part ”options“ consists of the tools for adjusting and handling with the picture. The program output consists of the basic aircraft visualization (plan view, side view) with relative deformations in the defined sections, node lines or node points (out of the plan view outline) and the supplementary visualization describing the phase relations among the structural parts (part ”plan“). Besides, program provides the graphs of the translational and rotational deformation amplitudes in the reference axes of the structural parts (part ”plot“) and finally the table of summary information (modes, frequencies, generalized masses).

The NASTRAN output file (*.f06 file) is opened (short data format is required) and the nodes coordinates and modal deformations are imported. The sketch of the aircraft (plan view, side view) is imported from the dxf files. The data format dxf is easy to create, edit or re-import. Apart from the AutoCAD, the dxf data format is supported by the various graphic tools like Corel Draw or Adobe Illustrator. The global coordinate system has an x-axis in the longitudinal direction, the y-axis is in the vertical direction, and the z-axis is in lateral direction. As the next step, the user defines the structural parts, controls and tabs. The structural parts are sorted by the type (surface / body, control, tab — see Fig. 3) and by the direction of the reference axis (wing, fin, fuselage). Also, the sections to draw the deformations in are selected. The modal deformations are transformed from the specified FE nodes to the reference axes of surfaces / bodies or to the pivot axes of controls and tabs by means of the cubic spline. The leading and trailing edges are defined as well (see Fig. 4). Finally the specific mode shape is selected and the visualization is drawn.

The mode shape vizualization consists of the basic aircraft visualization (plan view, side view, front view — see Fig. 5) with relative deformations in the defined sections. In-plane deformations are visualized by means of the arrows placed in

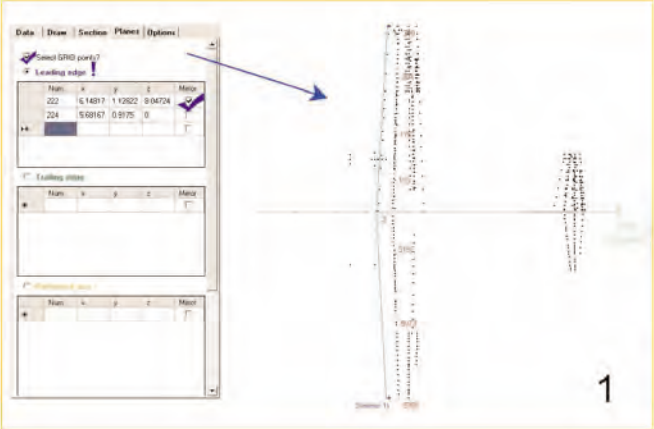

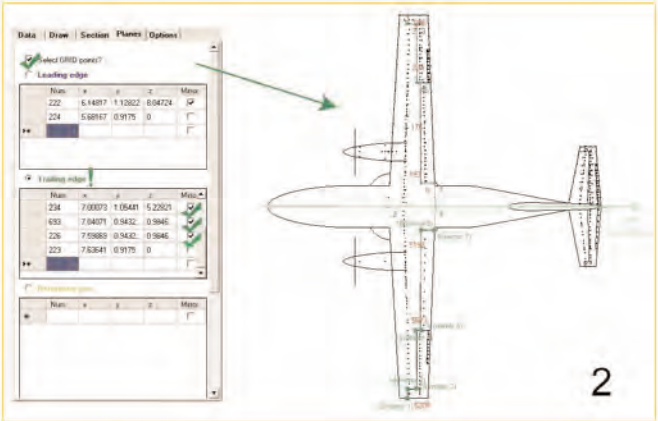

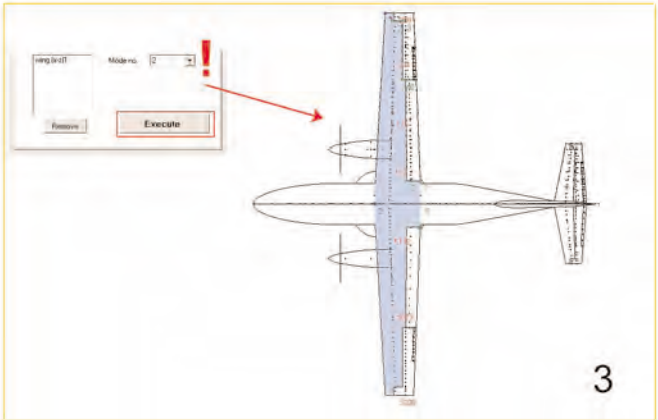

Fig. 4 — Leading / trailing edges definition

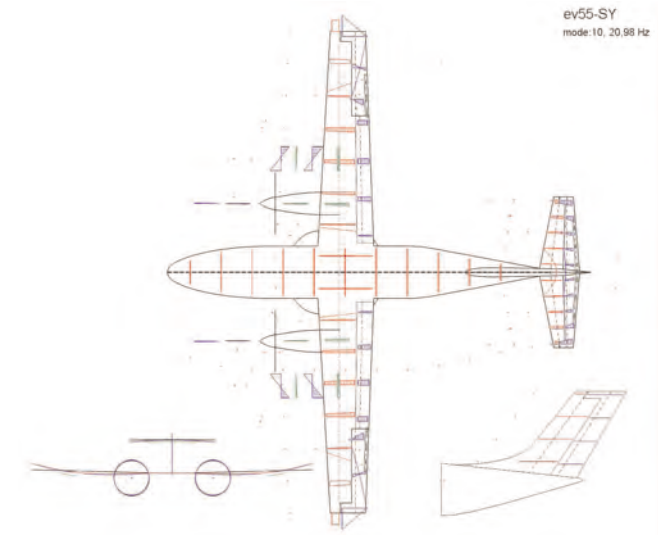

Fig. 5 — Program NASPRO - mode shape visualization (twin turbo-prop)

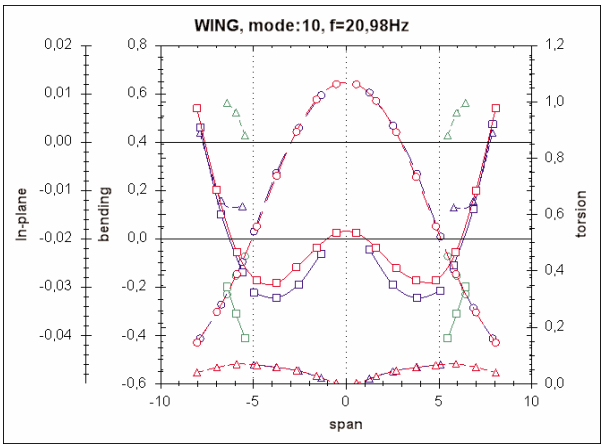

Fig. 6 — Program NASPRO - deformation curves

front of the leading edge. Node lines are visualized inside the outline of the plan view and side view respectively. Outside of the outline are visualized node points in the selected sections. The deformations of the engines are drawn by a specific way. Main visualization also includes the supplementary visualization describing the phase relations among the structural parts. Besides that, program provides the graphs of the translational and rotational deformation amplitudes in the reference axes of the structural parts (see Fig. 6) and finally the table of summary information (modes, frequencies, generalized masses).

Program includes various checking tools to avoid the user-made faults. Program is serviceable for any kind of the aircraft design configuration in terms of the number and configuration of the lifting surfaces, tail, engines, pods etc. or any part of the aircraft respectively. Program was created by means of the C# programming environment. It is operable on the common ver-

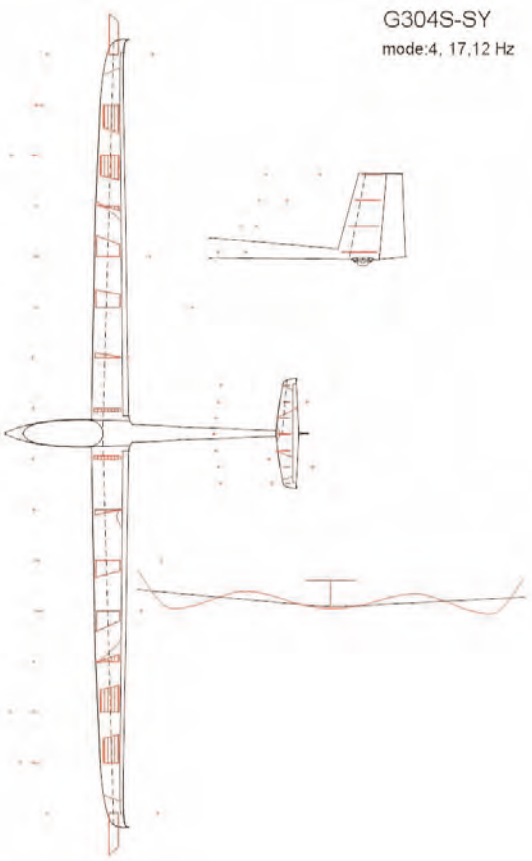

Fig. 7 — Program NASPRO - mode shape visualization (glider)

sions of the MS/Windows system. Program is equipped with the graphic user interface; it fulfills standard requirements regarding the user comfort or standard operations (export, saving, printing, etc.).

Program debugging was performed on the example of twin wing-mounted-engine utility 11-seat turboprop aircraft (EV-55) and a single-seat glider (G-304S).

4 Conclusion

Submitted paper presents a new software tool for transformation and visualization of the aircraft structure modal characteristics. It replaces the 18-years old obsolete tool, which is unserviceable today. The new tool will be used during development of new aircraft and research projects at VZLU as well. Based on software experience gained further improvements and modifications will follow.

Acknowledgement

The paper was created in the frame of the project MSMT 0001066903 *"Research on Strength of Low-weight Structures with Special Regard to Airplane Structures"* funded from the Ministry of Education, Youth and Sports of the Czech Republic.

References

[1] Latýn, M.: *Základní technické požadavky pro zpracování výsledků pozemních rezonančních zkoušek letounů, prováděných měřícím zařízením VZLÚ "Prodera 83"*; Report Let n.p. Kunovice, LET 9/4510/84, 1984

[2] Gallovič, D.: *Vývoj softwaru pro transformaci výsledků modální analýzy leteckých konstrukcí*; M.Sc. thesis, Czech Technical University Prague, Department of Aerospace Engineering, 2008/2009

[3] Hruška, M. - Fiala, J.: *Program NASPRO pro transformaci výsledků modální analýzy provedené systémem MSC.NASTRAN do výstupního formátu pozemní rezonanční zkoušky*; (uživatelská příručka verze 2.00), Report VZLU a.s., R-2735/94, 1994

[4] Černý, O.: *Teorie a praxe modálních zkoušek konstrukcí letadel*; Report VZLU a.s., R-2689/92, 1992

[5] Čečrdle, J.; Maleček, J.; Losík, V.: *Výpočet modálních charakteristik letounu EV-55*; Report VZLU a.s., R-4265, 2008

[6] Čečrdle, J.: *Dynamický MKP model letounu EV-55 (Verze V2)*; Report VZLU a.s., R-4271, 2007

Sensor Analysis for TEASER Project

Analýza senzoru pro projekt TEASER

Viktor Fedosov / VZLÚ, Plc., Prague

The article is focused on the Czech high sensitive electrostatic accelerometer MAC04TS on board the Russian small satellite. The paper provides an analysis of the instrument performance. In the first part the accelerometer system is analyzed. The behavior of the test mass and its capacitive feedback system is simulated in the time and the frequency domain for one degree of freedom in linear channel. The second part of the analysis presents the simulation results of the accelerometer measurements on board the satellite during orbit flight. For the simulation of non-gravitational forces in relation to orbit and spacecraft parameters one used non-conservative perturbations models developed by Astronomical institutes of Czech Academy of Sciences. Details of the simulation and discussion on its results are presented.

Keywords: non-gravitational perturbations, accelerometer, simulation.

Introduction

The MAC04TS is a new modification of the special device designed for measurement of spacecraft accelerations arising from the influence of non-gravitational perturbations like air drag, direct solar radiation pressure and other non-conservative forces. The influence of the upper atmosphere is not negligible and the effects of the non-gravitational forces, primarily of the radiation origin — direct solar radiation pressure, reflected radiation, infrared radiation are equally important for satellites tracking and forecasting their orbital and rotational motion. The instrument was developed and prepared to integration with the spacecraft and to operation in orbit in the frame of the project TEASER (***T**echnological **E**xperiment **A**nd **S**pace **E**nvironment **R**esistance*) which is financed by Ministry of Industry and Trade of the Czech Republic. The main aim of the project is verification of the microaccelerometer MAC04TS performance in orbit by direct measurements of the non-gravitational forces acting on the satellite. The obtained measurements will be analyzed on base of the comparison with data derived from satellite orbit determination and orbit evolution during satellite flight (data processing procedure is not discussed here). Following terms of the performances will be verified by analysis of the measured data: measurement noise in acceleration units, instrument bias, scale factor and sensitivity in each axis and their temperature dependencies.

Accelerometer

The principle of the device is very simple, see Fig. 1. The microaccelerometer's sensor is composed of a cubic proof mass free flowing in the cubic cavity. The proof-mass is moving freely between the electrodes C_1, C_2 and C'_1, C'_2 which measure the capacitance with respect to the walls of the external cubic cavity. The centre of the sensor should be placed in the spacecraft's centre of gravity. Proof mass is separated from external influences by satellite structure and microaccelerometer construction. Free motion of the proof mass is realized by virtue of only gravitational law. The cavity is rigidly connected to the satellite body. Gravitational and also all other perturbing forces acting on a satellite produce its acceleration and it is the same as the cavity acceleration. Capacitance is changing according to translation (x) as well as rotation (ϕ) displacement of

the proof-mass due to the difference between the acceleration of the cavity and the acceleration of the proof mass. The changing of the capacitance is detected by Position Detectors (D; D'). After mixing (S, S') with Polarization Voltage, capacitance is transformed into control tension U_x, U_ϕ which returns the proof-mass into its original location (centre of the cavity) by an electrostatic feed back servomechanism. In such case the electrostatic servomechanism must generate force to the proof mass which is proportional to the sum of all non-gravitational accelerations of the spacecraft. Proof mass is produced from quartz glass and the cavity is composed of six prisms from the same material. The detail description of the device is given by **Chvojka, Fedosov, 2006**.

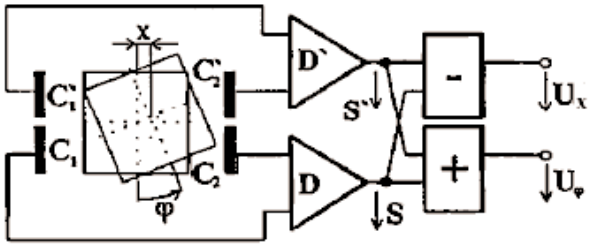

Figure 1 — Principle of the accelerometer

Model of measurement

The measurement model determines the connection between the accelerations due to non-gravitational perturbations acting on the satellite and the output of the accelerometer. We have to take into account that in real situation existence of displacement of the accelerometer relative to the center of mass of the satellite will cause that not only accelerations due to the non-conservative forces, but also accelerations due to gravitational forces and angular motion act on the proof mass. Hence, the measurement model we can describe is as follows:

$$\bar{\Gamma}_A = (G_{ij} + \bar{\omega}\bar{\omega} + \bar{\omega}')\bar{\delta r} + \bar{\Gamma} \qquad (1)$$

where:

- Γ_A - acceleration of the proof mass
- G_{ij} - matrix of gravity gradients
- ω - angular velocity of the satellite
- ω' - angular acceleration of the satellite
- δr - displacement of the accelerometer from the spacecraft center of mass
- Γ - non-gravitation acceleration

In this study, the displacement from the spacecraft center of mass has been neglected. In this case, the acceleration of the proof mass will be defined by magnitude of the summarized perturbation acceleration. Thereinafter, for simplification, we will examine one axis which relates with flight direction of the satellite (X axis).There, dominant non-gravitational perturbation is drag. Thus, the acceleration of the proof mass becomes (in X axis):

$$\bar{\Gamma}_A = \bar{\Gamma}_{DRAG} \qquad (2)$$

In other side, with respect to feedback control system (Fig. 2, see Fedosov, Chvojka, 2006) we can express acceleration of the proof-mass as function of the control voltage U_x and proof-mass shift (x):

$$\Gamma_x = \frac{4}{m} \cdot \frac{C}{D} \cdot \left(\frac{x}{D} - \frac{U_x}{U_0}\right) \qquad (3)$$

where:

- U_x - regulator compensative voltage: $U_x = K_D \cdot x \cdot H_1(s)$
- m - mass of proof mass
- D - the distance between electrode and the proof mass in the central position
- C - the capacitance between one electrode and the proof mass
- U_o - polarization voltage = 10(V)
- K_D - POSDET Sensitivity
- $H_1(s)$ - regulator transfer function.

The PD regulator is used for proof mass control position. It is characterized by proportional part with gain:

$$H_{1P} = -\frac{1200}{151}$$

And by derivative part with transfer function:

$$H_{1D} = \frac{0.217s + 1}{0.0366s + 1}$$

Simulation

The simulation was executed in frequency and time domain. Scheme presented in Fig. 2 and in compliance with equations (2, 3) was modeled in SIMULINK for instrument behavior analysis. In time domain we will examine one translation control circuit facing in direction opposite to spacecraft velocity (in direction of perturbation called the drag). Simulation time is equal to one orbit. Suppose, that a spacecraft which is characterized by size (0.5 x 0.5 x 0.7 [m]) and mass (70 [kg]) moves in orbit with following parameters:

- orbit period - 101,3 minutes;
- circular orbit;
- altitude - 820 km;
- inclination - 98,8°
- perigee argument - 66,5°
- eccentricity - 0,00112

Orientation of the spacecraft is unchangeable during one revolution and axis of the spacecraft reference system are directed according to nominal orbit operation (Y is orientated to the Sun, Z - to the Nadir, X - flight direction). Accordingly, drag force (R) is possible to calculate as

$$R = \frac{1}{2} C_D \rho A V^2$$

here:

- C_D is aerodynamic drag coefficient, for the simulation case = 2.5
- A is effective cross-sectional area of the spacecraft = 0.305 m^2
- ρ is thermosphere (high atmosphere density), for the simulation case ρ is calculated by using of the thermosphere model TD88 in relation to reference environmental condition (solar flux and geomagnetic parameter) and spacecraft orbital parameters. Detailed description of TD88 is given by **Sehnal, Pospisilova, 1988**.
- V is spacecraft velocity relative to atmosphere rotation, for the simulation case it is possible to define high atmosphere as statically and V is equal to the spacecraft absolute velocity. Thus, spacecraft acceleration due to drag force is $\Gamma_{Drag} = R/m$, here m is S/C mass.

Simulation Results

The Diagram 1 shows time variations of the ρ and Γ_{Drag} during one revolution of the spacecraft for the project TEASER conditions. The response of the accelerometer control system is represented by Diagram 2 (including control circuit thermal dependence). The diagrams 3 and 4 give us overall picture about ACC amplitude frequency characteristics. In Diagram 3 we can observe the regulator proportional part response from 0.0001 Hz up to 1 Hz and the derivative regulator part response with maximum value at 1 Hz. Frequency response of the instrument open loop transfer function is shown in Diagram 4 in a fine scale, the response curve turns the point (-1, 0j).

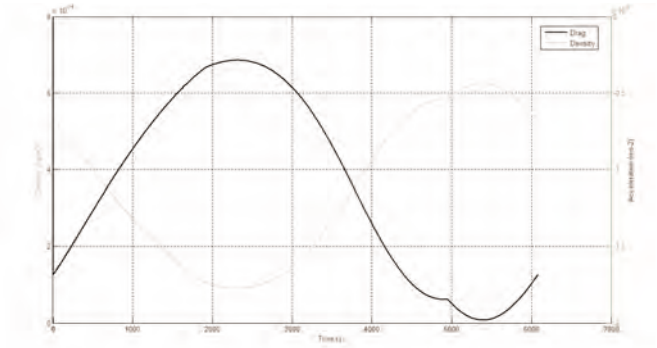

Diagram 1 — Atmosphere density and drag variation during one revolution

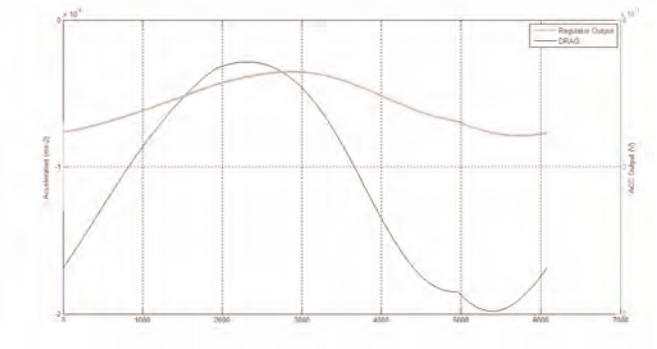

Diagram 2 — Drag acceleration vs. accelerometer output (V)

Bias of the measurement channel: -1. 3102E-7 [ms^{-2}]
Sensitivity of the measurement channel: 3.4954 [ms^{-2} /V]
Noise of the measurement channel at 1E-4 -0.1 [Hz] is close to white: ~2.2E-10 [$ms^{-2}/Hz^{1/2}$]

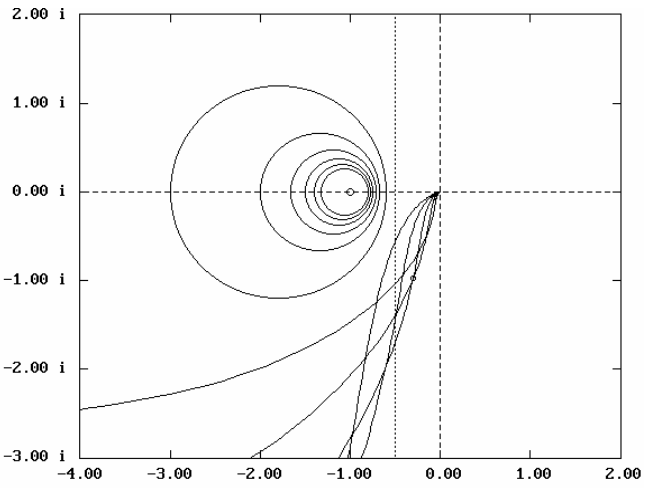

Diagram 4 — Instrument open loop transfer function characteristic

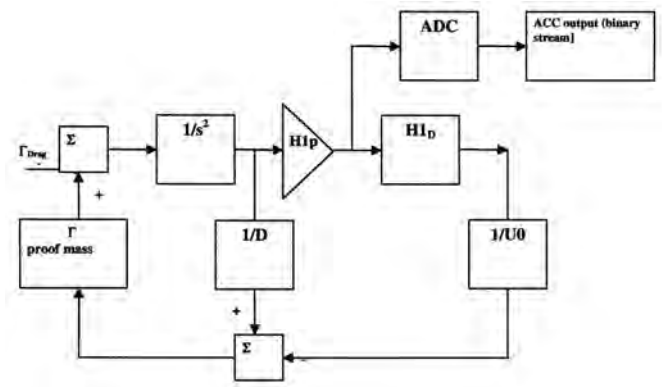

Fig. 2 — Block diagram of the accelerometer feedback control in one axis

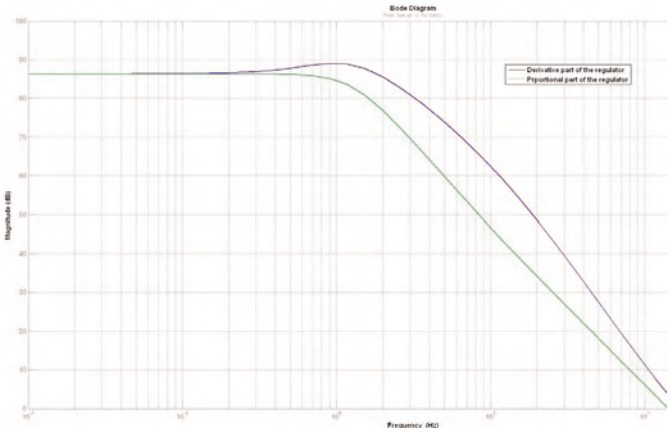

Diagram 3 — Instrument Amplitude - frequency characteristic

References

[1] L. Sehnal. L. Pospishilova: *Thermospheric Model TD88*; // Astronomical Institute Czechoslovak Academy of Sciences, Preprint N67, 1988

[2] V. Fedosov, M. Chvojka: *The High Sensitivity Microaccelerometer MAC (Development and Application)*; // Proceedings of 13th Saint Petersburg International Conference on Integrated Navigation Systems, pp 357 -360, 2006

[3] M. Rodrigues, B. Foulon, F. Liorzou, P. Touboul: *Flight Experience on CHAMP and CRACE with Ultra-sensitive Accelerometers and Return for LISA*; // Institute Physics Publishing, Class Quantum Gravity 20, pp 291-300, 2003

[4] G. Taratynova: *O dvizhenii ISZ v necentralnom pole tyagoteniya Zemlji pri nalichii soprotivleniya atmosfery*; Uspechy fizicheskikh nauk, Tom LXIII, 1957

Propeller Control Loop Model Development and Simulation of Transient Behavior

Vývoj modelu regulační smyčky vrtule a simulace přechodových stavů

Ing. Jaroslav Braťka / VZLÚ, Plc., Prague

This article describes a propeller control loop model for the transient analysis of a small two shaft turboprop engines rated up to 500 kW and presents dynamic simulation results of a new conceptual control system solution. Mathematical models of each component are described with the aid of unsteady one-dimensional equations and steady-state components characteristics. Basic governing equations are derived from integral forms of standard PID algorithm. Equation sets are solved using MATLAB - Simulink software package. Special efforts have been made to built realistic non-linear models both a controlled system (it means mechanically linked a free turbine, a gear box and a propeller) and hydraulic elements of the control system. The model also includes effect of ambient conditions like as air temperature, pressure altitude and air speed in boundaries defined in IS Atmosphere. Exclude of a control block, the model solves tasks in physical units which is important for easier imagination of real engine behavior and comparison with test data. Simulated results demonstrate control loop behavior in different operational situations and conditions and determine parameters limits of control system components.

Tento článek popisuje model regulační smyčky vrtule malého dvouhřídelového turbovrtulového motoru do výkonu 500 kW, který je určen pro analýzu dynamického chování smyčky a presentuje výsledky simulací nového koncepčního řešení řídícího systému. Matematické modely jednotlivých komponent jsou vytvořeny pomocí diferenciálních jednodimenzionálch rovnic a statických charakteristik jednotlivých prvků smyčky. Základní algoritmus řízení je vytvořen na základě standardního PID algoritmu. Soustava rovnic je řešena v programovém prostředí MATLAB - Simulink. Zvláštní důraz byl kladen na vytvoření realistického nelineárního modelu jak regulované soustavy (tj. mechanicky propojené soustavy volná turbína, převodovka a vrtule) tak hydraulických prvků řídicího systému. Model rovněž zahrnuje vliv vnějších podmínek jako jsou teplota vzduchu, tlaková výška a rychlost letu v rámci definic ISA. Vyjma bloku řízení pracuje model v reálných fyzikálních jednotkách, což zjednodušuje představu o chování smyčky v různých provozních situacích a umožňuje porovnání s výsledky experimentů. Výsledky simulací ukazují dynamické chování regulační smyčky v různých provozních situacích a definují limity parametrů jednotlivých prvků řídící smyčky.

Keywords: mathematical model, propeller control system, dynamic behavior simulation.

Introduction

In the present days there is strong pressure to apply new trends and new technologies in propeller control. Hence there were proposed new conceptual schemes. The common goals of these proposals are:

- integration of both the gas generator and the propeller controls in a single electronic control unit;
- single lever power plant control;
- fully electrically controlled engine without mechanical linkages between an aircraft cockpit and an engine;
- minimization of hydraulic elements number;
- reducing of control system power consumption;
- high reliability and intelligent capability for self diagnostic and maintenance support.

One of more new conceptual schemes is direct control of oil flow by oil pump speed control in a propeller control loop. This solution was evoked by progress in area of brushless DC motors and its control. Using control loop modeling it was worked up an analysis from point of system dynamic behavior view and they were also defined critical part parameters. The analysis was made for a double shaft turboprop engine with power rate up to 500 kW and a single acting propeller of ”pressure to decrease pitch“ type.

Brief function description

The propeller control system is schematically shown in Fig. 1. The main part of this control system is an electrically driven gear pump which delivers pressurized oil to a propeller hydraulic actuator. The pump is fed from engine lube oil system. A beta valve, which is placed between pump and an actuator, ensures that the propeller blades does not travel below the in-flight low-pitch position (so-called a hydraulic lock) and also hydraulically connects a rotated propeller shaft with oil duct in a gear box casing. Pressurized oil is led into a propeller actuator via a hollow propeller shaft. The part of oil flow is passed via an orifice back to a tank. In the stable state the pump covers only flow through the orifice. If it is needed to decrease blade pitch the control unit increases pump speed whereby increases flow and pressure and oil flows to the actuator. And on the contrary, in case of blade pitch increasing the control unit decreases pump speed and oil can flow from the actuator out. If the rate of blade increasing is insufficient the control unit opens a solenoid valve and increases flow out.

Propeller control loop modeling

The overall model is composed of modular blocks represented by individual subsystems such as propeller subsystem, hydraulic subsystem and a control unit.

Propeller subsystem

The propeller subsystem is controlled system and it is composed of mechanically coupled a power turbine, a gear box and

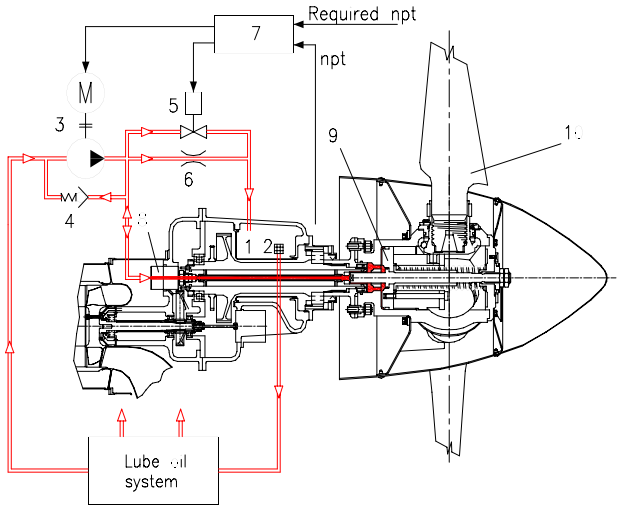

Fig. 1

Hydraulic subsystem

The hydraulic subsystem comprises of the propeller pump with the relief valve, the hydraulic actuator, the beta valve and the relief block. The features of each component can significantly affect behavior of the system hence it is interest to create a realistic model in real units which will be simulate pressure and flow include parasitic influences. Figure 3 shows a schematic diagram of the hydraulic subsystem and Figure 4 shows diagram of the model.

a propeller. Its purpose is conversion of energy transferred from a gas generator to a power turbine on a thrust vector. The controlled parameter of this system is propeller speed. From mathematical viewpoint, it is nonlinear system with one degree of freedom. Following parameters characterize the system:

P_T . . . . . .Power of power turbine
P_P . . . . . .Power of propeller
TRQ_P . .Torque moment of propeller
TRQ_T . .torque moment of power turbine
ω . . . . . .Angular velocity of propeller
φ . . . . . .Propeller blade pitch
D . . . . . .Propeller diameter
J . . . . . .Sum of inertia moments of power turbine, gear box and propeller corrected to propeller speed.
C_p . . . . . .Propeller torque coefficient

Propeller blade pitch (φ) is the manipulated variable and external influences like deviation of ambient temperature from standard (*delta T*), pressure altitude (h) and flight velocity (v) represent disturbing variables.

Modeling dynamic behavior is based on solution of the following equations:

$$J\dot{\omega} = (TRQ\_T) - (TRQ\_P)$$

$$TRQ\_P = \frac{Pp}{\omega} \quad ; \quad TRQ\_T = \frac{Pt}{\omega}$$

$$P_p = C_P \, \rho \, n^3 \, D^5$$

$$\lambda = \frac{v}{nD}$$

Block diagram of propeller subsystem model is depicted in Figure 2.

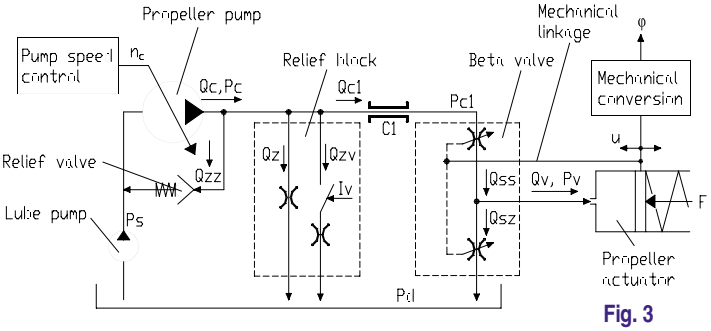

Fig. 3

Hydraulic actuator

For purpose of control loop demonstration a single acting hydraulic actuator is used. Generally, a piston of an actuator is loaded from one side by sum of spring, aerodynamic, centrifugal and counterweight forces, the opposite side of piston is loaded by pressurized oil. Position of the piston (u) is calculated from oil flow (Qv) and piston area (Sp):

$$\dot{u} = \frac{Q_V}{S_P}$$

Straight-line movement of the piston is converted to rotating motion of the propeller blade in a simple goniometric conversion block for geometric scheme of a propeller.

Electrically driven gear pump

In the model, the gear pump is represented by flow characteristic [5] which is expressed by equation:

$$Qc = (K_{11}*\Delta Pc + K_{10}) * n_C - K_{01}*\Delta Pc + K_{00}$$

Where: $\Delta Pc = P_C - P_S$
P_C … outlet pressure
P_S … inlet pressure
n_C … pump speed

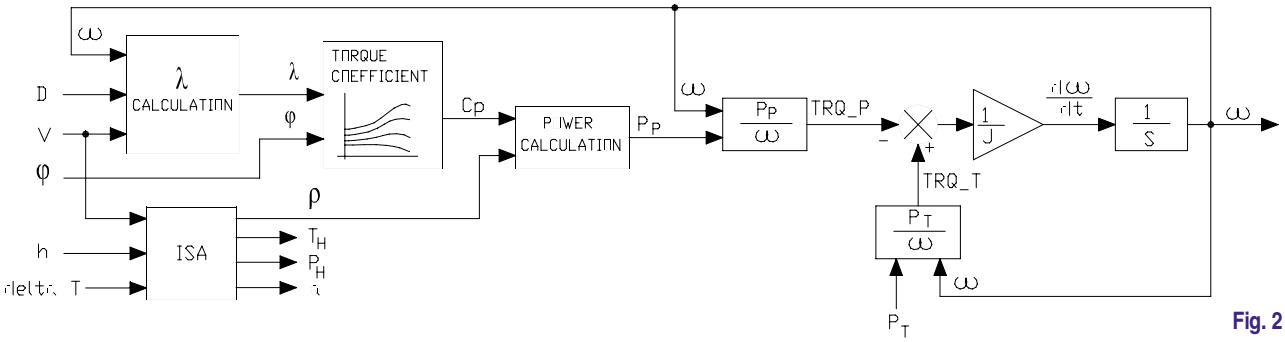

Fig. 2

The pump is driven by a brushless electric motor which is controlled by its electronic control and an excitation unit. In the model, the electric drive dynamic behavior is modeled by the second-order block with different time constants for increasing and/or decreasing motor speed.

Beta valve

The beta valve (also called a hydraulic lock) is a special valve which prevents a propeller from blades travelling to a position below the in-flight low-pitch position. Its slide is mechanically linked with the actuator piston and closes oil feeding into a hydraulic actuator and simultaneously opens drain from the actuator off in case the propeller pitch equals the in-flight low-pitch.

The model calculates oil flow to drain and the pressure drop on the restriction section by formulas:

$$Q_{SZ} = K_{SZ} * S_{SZ} * \sqrt{\frac{2}{\rho}} * \sqrt{|P_V - P_D|}$$

$$\Delta P = sign(Q_{RV}) * \left(\frac{Q}{Q_{REF}}\right)^2 * \left(\frac{S_{REF}}{S}\right)^2 * \Delta P_{REF}$$

Values of cross-section and other constants are taken from the valve manufacturer.

Relief block

The relief block comprises relief orifice with fixed cross-section and the NC solenoid valve. Both components flow oil out to the drain. The oil flow is calculated by formula

$$Q_{ZV} = Q_Z = K_{ZV} * S_{ZV} * \sqrt{\frac{2}{\rho}} * \sqrt{\Delta P}$$

$$\Delta P = Pc - Pd$$

Speed controller

The speed controller closes the constant speed control loop and in the model it is considered as the P algorithm with variable gain. The part of the controller is a logical block which switches the relief solenoid valve when the controlled variable deviation exceeds the treshold value.

Transient performance analysis

The critical point of the proposed control scheme from the point of dynamic behavior view is the oil pump electric drive and especially its dynamic behavior. Therefore the transient performance analysis was aimed to finding of acceptable time constant of this electric drive.

In the simulation investigation, the following three time constant combinations were considered for acceleration and only one for deceleration:

Acceleration: a) $T_2 = 0$ s, $T_1 = 0$ s
b) $T_2 = 0{,}02$ s, $T_1 = 0{,}2$ s
c) $T_2 = 0{,}05$ s, $T_1 = 0{,}5$ s
Deceleration: $T_2 = 0{,}001$ s, $T_1 = 0{,}1$ s

In the analysis, it was evaluated response of propeller speed to following both power and demanded propeller speed changes at sea level standard atmospheric condition:

a) Power increasing from 20 to 400 kW at propeller speed 2150 RPM and air velocity $v = 0$ km/hr. Rate of power change is
$$\frac{dPt}{dt} = +150\,kW/s$$
b) Power decreasing from 400 kW to 150 kW at propeller speed 2150 RPM and air velocity $v = 0$ km/hr. Rate of power change is
$$\frac{dPt}{dt} = -250\ kW/s$$
c) Step change from 1950 RPM to 2150 RPM of demanded propeller speed at power 400 kW and air velocity $v = 150$ km/hr;
d) Step change from 2150 RPM to 1950 RPM of demanded propeller speed at power 400 kW and air velocity v = 150 km/hr;

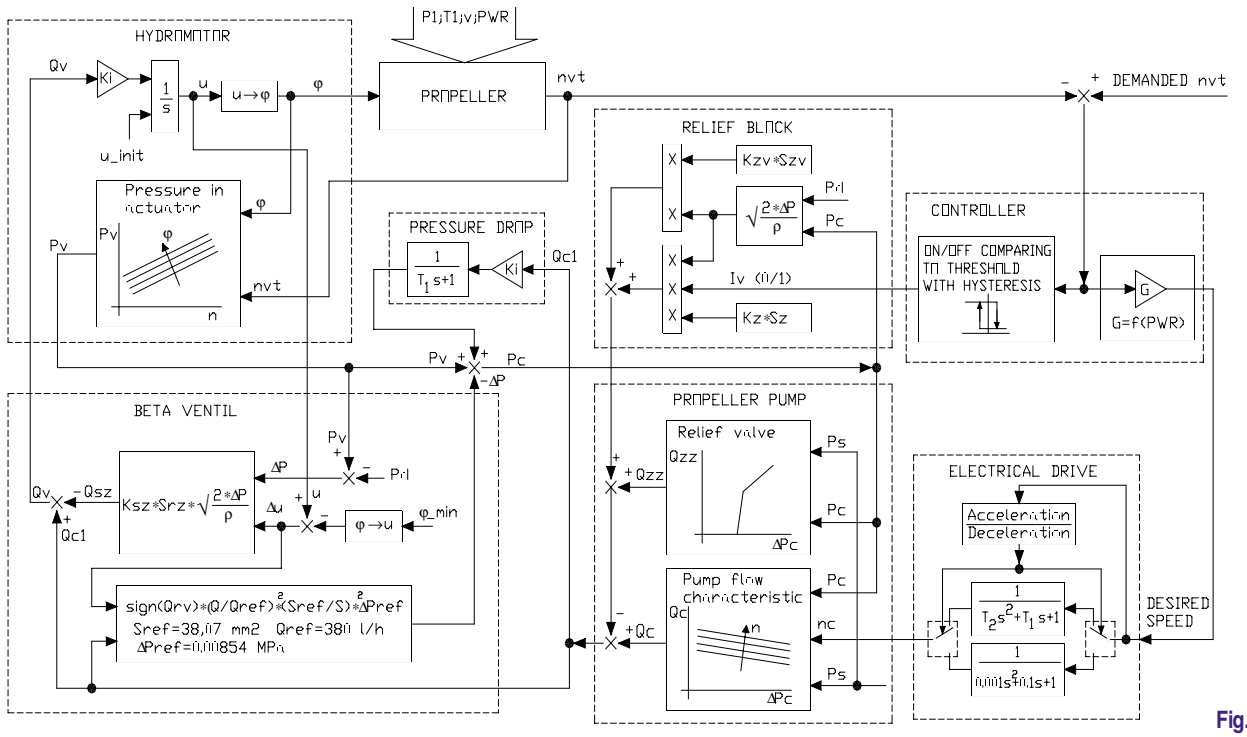

Fig. 4

Results and discussion

Transient results of simulation are shown in Figures 5 a), b), c) and d).

In cases a) and d), changes of power or demanded speed causes requirement on propeller pitch rise. It is performed by oil flow out via the relief block and at the same time oil pump speed decreasing. Oil pump dynamic is not important in case a) and the control loop is stable but in case d) the loop has got tendency to oscillation according to growing oil pump drive time constants.

In cases b) and c), changes of power or demanded speed causes requirement on propeller pitch decrease. It ensures oil flow increasing by oil pump speed increasing. In those cases an impact of oil pump drive time constant is important and time constants increasing evoke instability of the control loop. It can partially solve PD - control algorithm applying with lower gain.

Conclusion

The analysis presented shows that the concept based on oil pump speed control is on principle feasible but for real use is critical its high sensitivity to dynamic features of oil pump drive. On the base of simulation it can be determined time constant $T_2 = 0{,}02$ s, $T_1 = 0{,}2$ s for pump speed acceleration as limit for stable control loop behavior. Dynamic features can be improved by using PD — control algorithm but with reduced gain. Requirement for electric motor acceleration is hard and it can be met at the big current and electric power peak expense, which can be unacceptable for power supply main. Hydraulic parameters degradation with operation time must be taken into account. From the point of view of this argument it is hard to provide such a robust controller which ensures stability of propeller control loop for all operational life.

References

[1] Noskievič, P.: *Hydrostatické pohony a jejich řízení*; Automa, 2002, č. 1

[2] Braťka, J.: *Simulační model regulační smyčky vrtule*; Zpráva VZLÚ R-3936, 2006

[3] Braťka, J.: *Návrh systému řízení vrtule motoru TP100*; Zpráva VZLÚ R-4011, 2006

[4] Braťka, J.: *Studie řízení vrtule otáčkově řízeným čerpadlem*; Zpráva VZLÚ R-4037, 2006

[5] Oháňka, Z.: *Podklady pro matematický model regulátoru vrtule varianty C1 dle nových koncepcí řízení vrtule malého turbovrtulového motoru*; Zpráva JSV Z-SATE-752/06, 2006

[6] Kerlin, T., Bratka, J.: *CP-CS Modelling and Simulation Results Report*; CESAR Deliverable Document CE-UNIS-T3.2-D3.2.1-4 Rev. 0; 2008

[7] Yaguo Lu, Zhenxia Liu, Shengqin Huang and Tao Xu: *Numerical Simulation of Aero-engine Lubrication System*; Journal of Engineering for Gas Turbines and Power; 2009, Vol. 131/034503-1

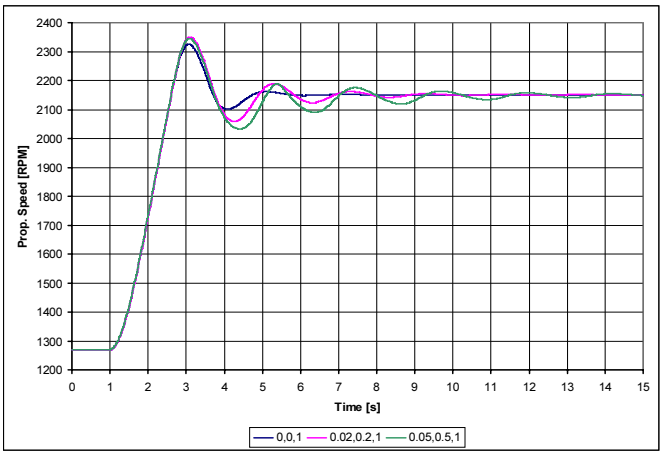

Fig. 5a) — Power increasing

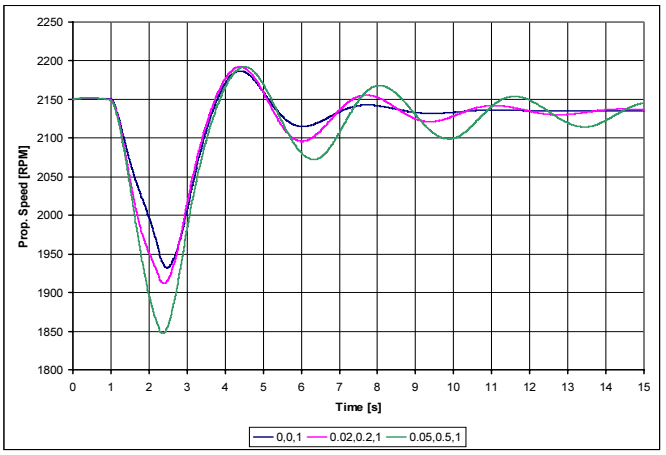

Fig. 5b) — Power decreasing

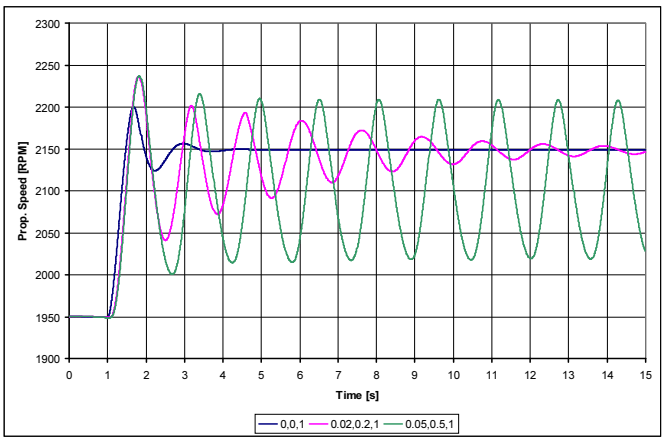

Fig. 5c) — Propeller speed increasing

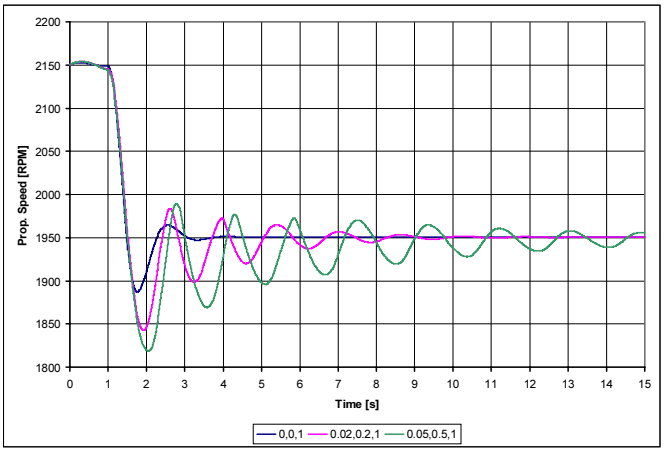

Fig. 5d) — Propeller speed decreasing

Unmanned Aircraft Structural Model and its FEM Analysis for Strength Evaluation

Strukturální model bezpilotního letounu a jeho MKP pevnostní analýza

Aleksander Olejnik, Stanisław Kachel, Robert Rogólski, Piotr Leszczyński / Military University of Technology, Faculty of Mechanics, Warsaw, Poland

In the paper, the generating process of airframe structure model was presented for the usage in numerical FEM analysis. The work was carried out by providing as an airframe example a UAV prototype structure of the PW-141 SAMONIT. The numerical thin-walled FEM model of the small UAV was worked on the base of surface geometry model imported from the CAD system. The set of virtual materials was prepared which was used to simulate the properties of applied multi-ply composite materials. The flight loads analysis was performed - the flight envelope was formulated on the basis of the geometric and mass data or aerodynamic data received from the CFD analysis for the VLM model in the stable flow. For the extreme external load cases of the envelope the load distribution was determined and the series of numerical strength calculations were performed using MD Nastran software. The results were presented in form of the stress and displacement distribution areas. By comparing the results the aircraft construction safety was preliminary evaluated in the context of the structure strength effort.

Keywords: strength analysis, UAV system.

1 Introduction

In the framework of the research project on the *"Design and technology for the PW-141 SAMONIT light surveillance"*, a numerical model for the needs of static FEM analysis was worked out. A discrete model of the structure was implemented for the strength analysis, which was done for evaluation of deflection and stress areas in the typical flight load cases. Lift force external load was taken using the UAV flight load envelope, whereas the force distributions taken to simulation were based on the load distribution, which came form the Vorlax programme. The MSC Patran/Nastran package was used for the final modelling process and strength analysis as well.

2 Aircraft geometry model for the elaboration of calculating mesh needs

Model of geometry of the PW-141 UAV generated in the 3D CAD environment was adapted to mesh structure generator, in which the final discrete model for the FEM analyses was worked out. For the needs of the Patran pre-processor, the 3D model structure description was simplified to 1 and 2D geometric models. Due to shell-tiny character of the aviation structure, a surface model was required, which was a convenient base for generation of shell elements. The set of the bi-parametric surfaces modelling the bulkheads and aircraft skin is the final form of the model adapted to the discretisation (Fig. 1).

3 Discrete model of the lifting surfaces

Elaboration of the discrete model of the structure for strength analysis was connected with consecutive intermediate task, which can be set in the following order:

- preparation of the base geometry,
- discretisation of the strength structure (mesh generation),
- structure materials selections,
- identification of the material properties,
- boundary condition determinations,
- external load simulation,
- setting of the calculation case for the selected solver.

Main 2D elements: rectangle (CQUAD4) and triangle (CTRIA3) with shell properties, completed by a single-dimensional element rods (CROD) or beams (CBAR) were used. Geometric form of the elements and available node degrees of freedom are presented in Fig. 2.

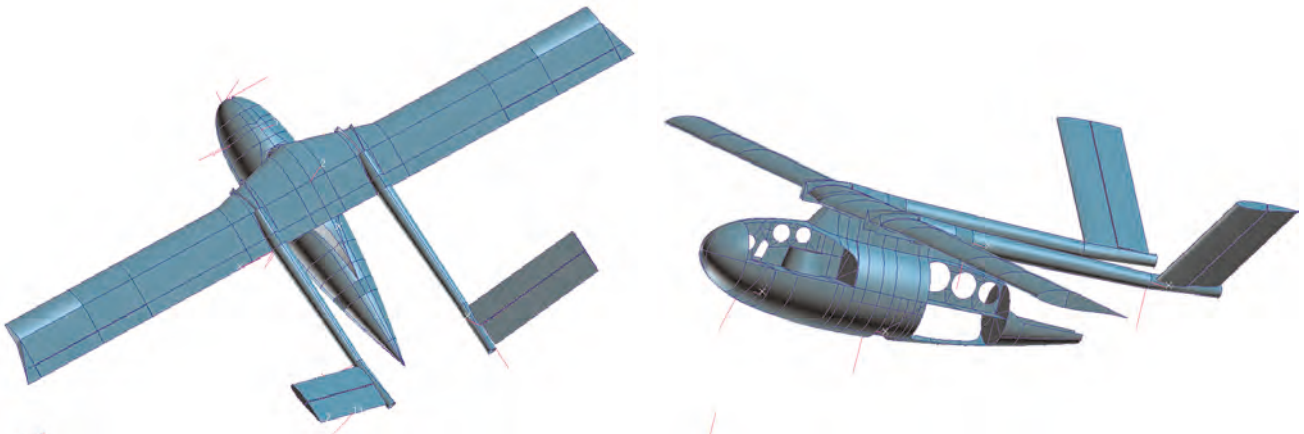

Fig. 1 — Geometry of load structure for the PW-141 UAV, modelled by surfaces; upper view and inner strength structure view — longitudinal wall geometry includes access panels

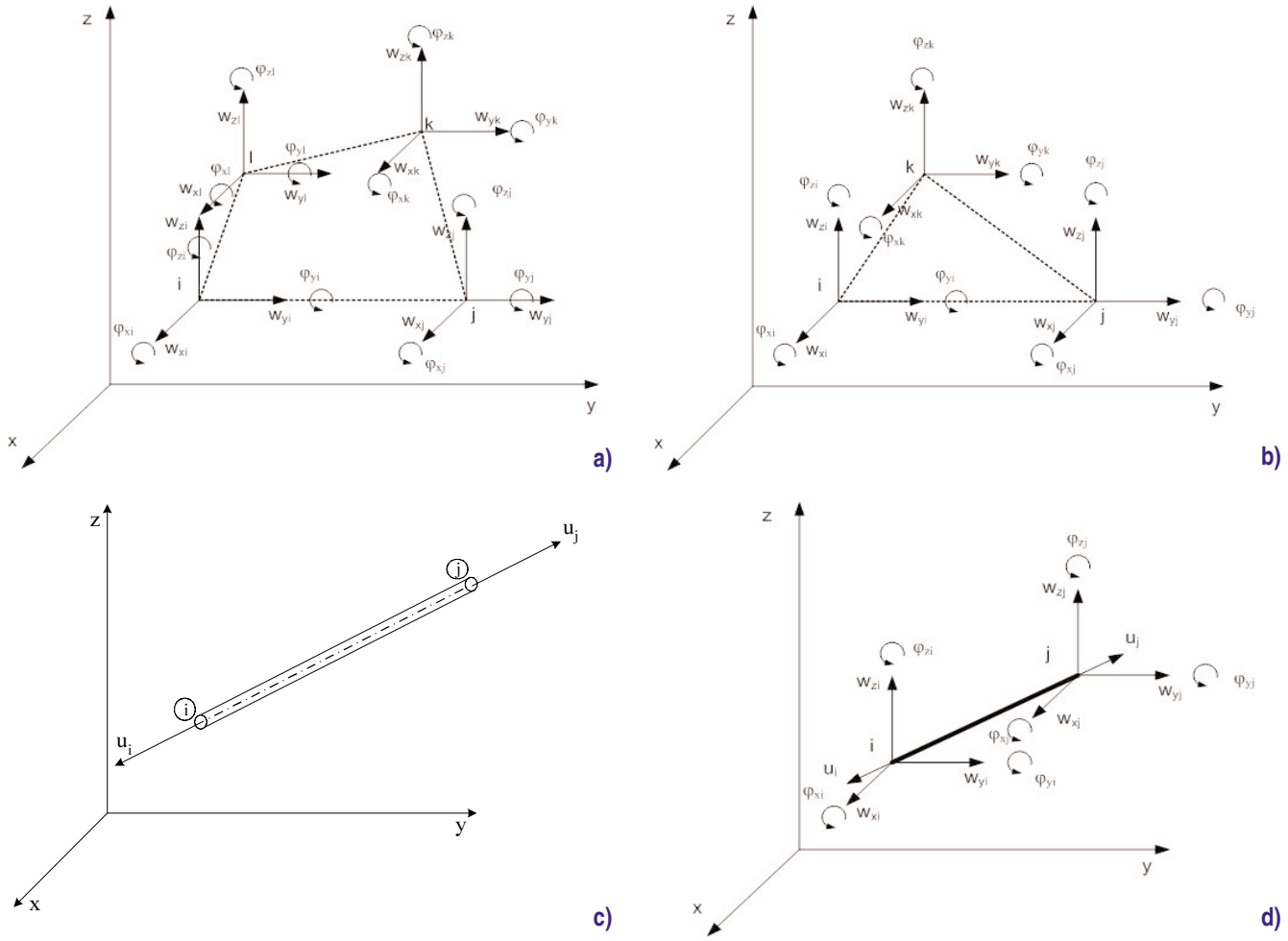

Fig. 2 — The finite elements used in strength model of the PW-141 structure: a) a rectangle element CQUAD4; b) a triangle element CTRIA3; c) a rod element CROD; d) a beam element CBAR

Using Patran's mesh generator, a geometric area was divided into elements, by the recommended topology of the four-node flat element (CQUAD4). After setting the defining division for the edge curves of the model surface and selection type of the mesh (Mesher — Iso Mesh) 11070 elements were set, which based on 9440 nodes. The main division of the base geometry for fuselage sponson and wing was presented in Figs. 2 and 3, whereas the complete model of the airframe structure is presented in Fig. 4.

A lifting structure is made almost completely from a carbon composite material, with a small amount of the aluminium alloy and steel. Inner structure elements and skin are carbon-epoxy laminate. A number of the textile or rowing layers are from 2 to 8 and depends from aircraft structure. For the investigating model it was taken, that a material is composed of a few orthotropic layers working in the flat stress and deflection state, whereas space deflections of the laminate are resulted from the differences of the flat states along it thickness. The concept of the laminate modelling by the assistance of the MSC Patran package bases on a declaration of the assigned layers of the isotopic or orthotropic materials and their thinness and angle of orientations (Fig. 6).

The constitutive equation for a single orthotropic layer in an axial load configuration and deflected in the layer surface has a following form:

$$\begin{bmatrix} \varepsilon_1 \\ \varepsilon_2 \\ \gamma_{12} \end{bmatrix} = \begin{bmatrix} S_{11} & S_{12} & 0 \\ S_{21} & S_{22} & 0 \\ 0 & 0 & S_{66} \end{bmatrix} \begin{bmatrix} \sigma_1 \\ \sigma_2 \\ \tau_{12} \end{bmatrix} \quad (1)$$

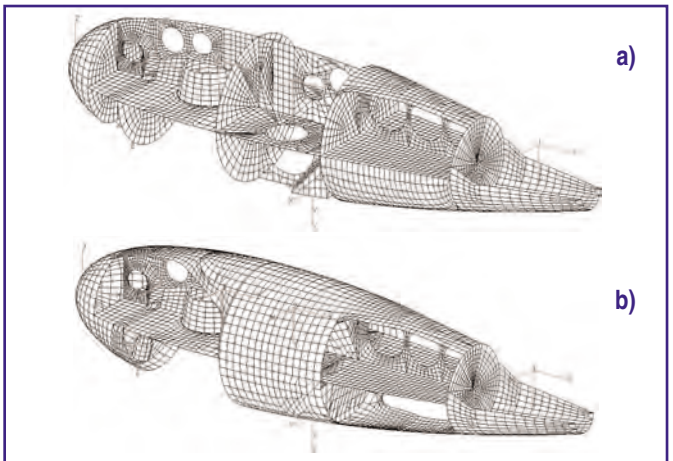

Fig. 3 — Surface mesh modelling of the fuselage sponson; a) internal structure, b) structure with skin without the access panels

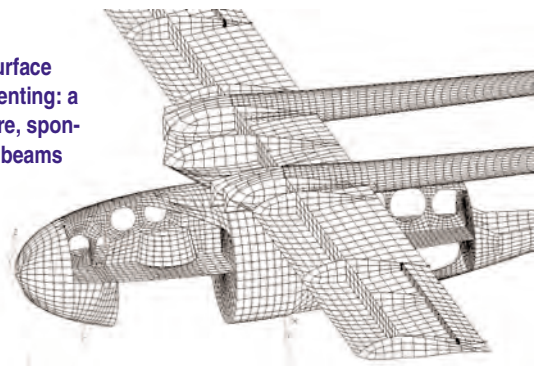

Fig. 4 — A surface mesh representing: a wing structure, sponson, and tail beams

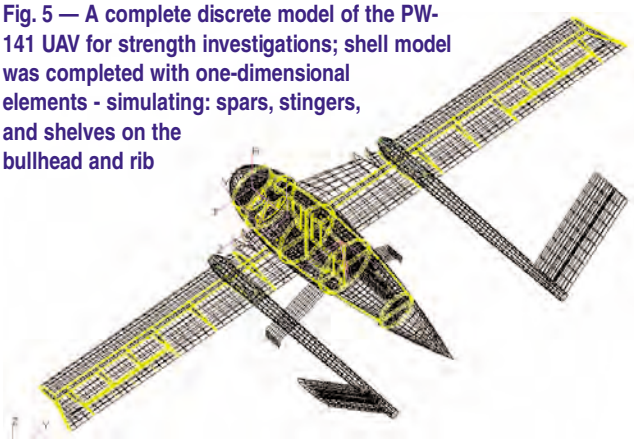

Fig. 5 — A complete discrete model of the PW-141 UAV for strength investigations; shell model was completed with one-dimensional elements - simulating: spars, stingers, and shelves on the bullhead and rib

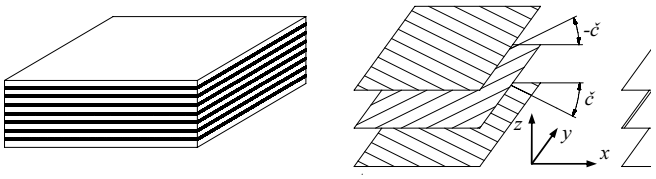

Fig. 6 — A model of the reinforced multi-ply laminate

Above presented matrix expression presents relation between deformation and stress, indexes are connected with reinforcement direction and perpendicular direction (Fig. 7). In turns matrix [*S*] it is a matrix material flexibility, which elements there are: E_{11}, E_{22}, G_{12}, ν_{12}, ν_{21} (module: Young, Kirchhoff, Poisson number). In non-axial configuration connected with the lamination θ layer, [S] matrix of modification is a matrix of transformation *T*, depending from specific trigonometry functions of the angle θ:

$$[S'] = [T]^{T} [S][T] \qquad (2)$$

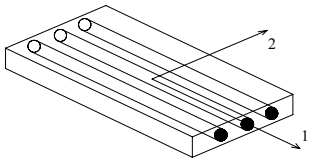

Fig. 7 — Configuration of the orthotropic axial layer reinforced one-directionally

Defining composite material for the needs of a discrete model based on declaration of the consecutive glued layer materials of the pile (there are parameters: *E*, *G*, ρ, ν), layer thickness and orientation in reference direction (Fig. 8). Parameters: E_{11}, E_{22}, G_{12}, ν_{12}, ν_{21} of layer composite for the S_{ij} stiffness matrix components are elaborated in compliance with the mixtures rule or reverse mixture rule on the base of estimated capacity volume participation of the specific components. For numerical calculations component materials with well know properties were applied: KDL 8003 fabric, KDU 1007 carbon roving tape, epoxy resin EP 53Z — material constants shown in the Table 1.

KDL 8003		KDU 1007		epoxy EP53Z	
E_{11} [GPa]	74	E_{11} [GPa]	181		
E_{22} [GPa]	74	E_{22} [GPa]	10,3	E [GPa]	4
ρ [kg/m^3]	1800	ρ [kg/m^3]	1800	ρ [kg/m^3]	1200
ν_{12}	0.05	ν_{12}	0.28	ν	0.35
G_{12} [GPa]	4,55	G_{12} [GPa]	7,17		

Tab. 1 — Material constants of the carbon-epoxy composite components accepted for the FEM model

Properties of the laminate with variable layers are assigned to the elements in the specific structure areas, in accordance to

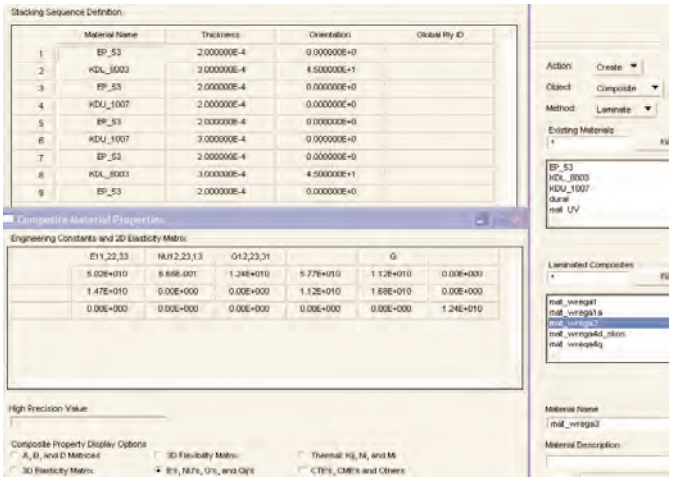

Fig. 8 — An example of creation of a carbon composite structure — Four layers of carbon fabric KDL 8003 of 0,3 mm thickness, glued with EP53Z epoxy; additionally material parameters E_{11}, E_{11}, ν_{12}, G_{12} and stiffness matrix *Q* which is a reverse of the flexibility matrix *S*

lamination plans. In this way a virtual structure with variable stiffness properties due to thickness and sort of the apply layers. Variability of the structure zones due to used laminated materials is presented in Fig. 9.

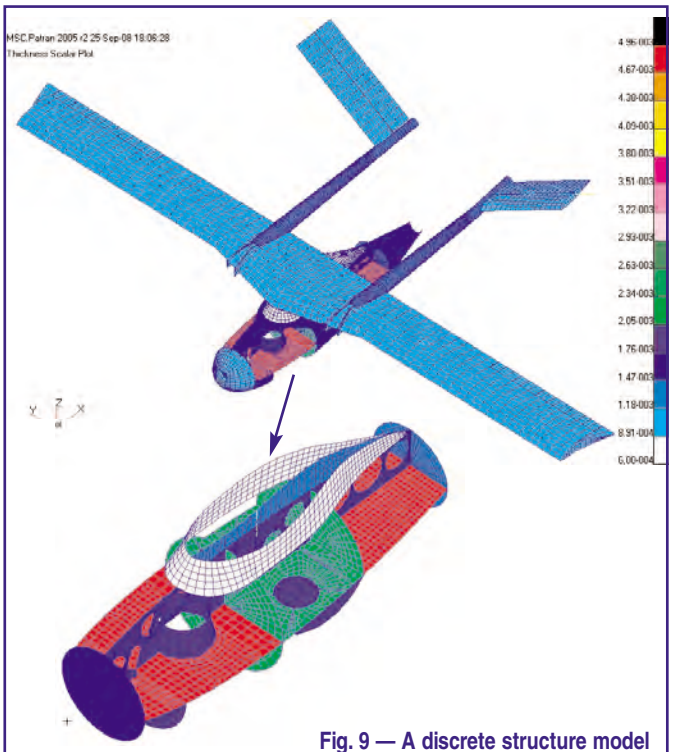

Fig. 9 — A discrete structure model with visualisation of the laminates variability used in airframe construction; sponson structure is well detailed in the lower picture, the colour scale specificates the element thickness: from 0.6 mm on the pylon skin to maximum value 4,96 mm of horizontal wall of the sponson

4 External load

Safety issue and structure resistance from flight aerodynamic load are appeared in the case of the UAV as well as manned aircraft. Nowadays, the joint regulations for UAV's are not exist so far. In the case for the military application outside the restricted area, civil air traffic regulations must be satisfied and for the PW-141 UAV the European CS-VLA regulation were taken as applicable.

The PW-141 UAV is equipped with a V-type tail unit, trapezoidal inner part of the wing (between beams) and rectangular one — outer part of the wing with the Workman FX66-17AII-182 profile. For the flight external load envelope some aerodynamic data were required: slope of the $C_Z(\alpha)$ characteristic and extreme value of the lift coefficient: C_{Zmax} and C_{Zmax}. In the first estimation, set of aerodynamic characteristics of the isolated wing, by two methods: the vortex lifts line (Multhopp's method) and net vortex method of the VORLAX programme was found out. The comparison of final results is presented in Fig. 10.

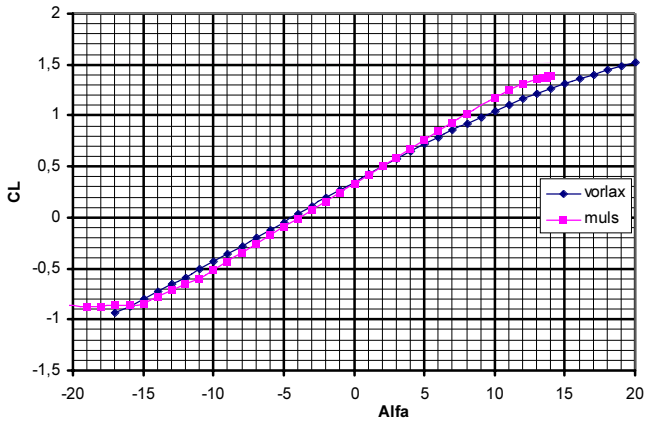

Fig. 10 — C_Z - lift force coefficient of the wing in function of α - the angle of attack

For an isolated wing during the flight envelope calculations, it can be taken a slope of the $C_Z(\alpha)$ in conservative way from above presented diagram: $a = dC_Z/d\alpha = 4.895$. For the explicit elaboration of the C_{Zmax} and C_{Zmax} coefficients of the whole aircraft, calculations for the flow of the whole aircraft body were undertaken. Due to fact that the V-type tail is an extraordinary unit, conventional approach with partition of the tail unit into horizontal and vertical one is not acceptable. In this case, an aerodynamic model for the net vortex method was used. The final volume of the C_Z are: $C_{Zmax} = 1.31$, $C_{Zmin} = -0.8$.

For the elaboration of the particular points of the flight envelope the following data were taken:

Maximum aircraft computational weight	W_{max}=69 kG
Minimum a/c take-off weight	W_{min}=36 kG
Wing surface load for W_{max}	$(W/S)_{max}$=35.94 kG/m^2
Total wing area	S=1.92 m^2
Wing span	b=4.6 m
Mean geometric chord	$\bar{c}$ =0.422 m
Wing aspect ratio	Λ=11.02
Max. lift coefficient	C_{Nmax}=1.31
Min. lift coefficient	C_{Nmin}=-0.8
Slope of the lift coefficient characteristic	$a=\left(\frac{dC_z}{d\alpha}\right)_{skrz}$ =4.895
Horizontal velocity at the permanent maximal power	V_H=185 km/h

In compliance with the CS-VLA regulations, required parameters for the flight envelope were found (Fig. 11)

- Manoeuvre load coefficients [CS-VLA.333, VLA.337]: $n_A=n_C=n_D=6$, $n_G=n_F=n_E=3$;
- Calculating velocity EAS [CS-VLA.335]: cruise speed V_C= 190 km/h, diving speed V_D= 250 km/h, manoeuvre speed V_A= 185 km/h, manoeuvre speed of reverse flight V_G= 167.2 km/h;
- Load coefficients including gust [CS-VLA.341; VLA.333]; extreme value of the coefficient with altitude limitation to 6096 m for the minimum and maximum a/c weight: Q_{max}= 69 kG: n= +6.324, n= -3.872; Qmin= 36 kG, n= +10.699, n= -7.428;

Calculation of wing aerodynamic loads was done for stable flight state in the points: C, D, E, F and G of the flight envelope. To get the equivalent load in the form of replacing lumped forces set in the nodes of the mesh of the discrete model of the wing, a numerical integration of the pressure distribution along the longitudinal directions to the flow was done. The focused mass load was included, which was estimated on the base of area participation of the specific strap section of the wing area. A scheme of the wing division on the integration areas (strap) are presented in the Fig. 11.

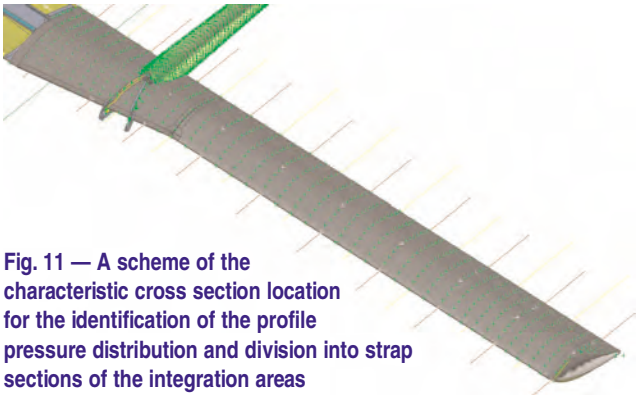

Fig. 11 — A scheme of the characteristic cross section location for the identification of the profile pressure distribution and division into strap sections of the integration areas

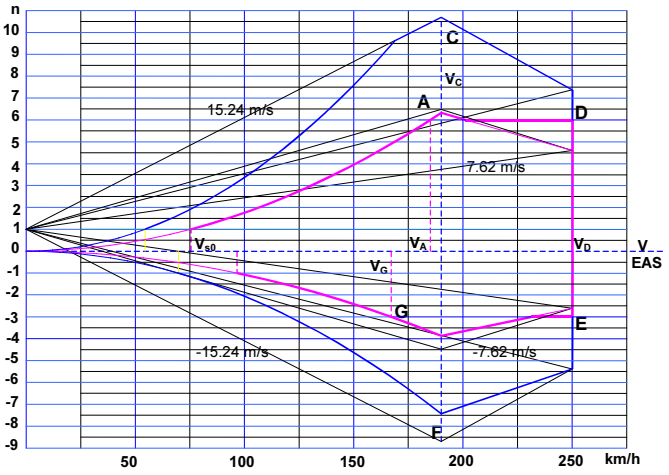

Fig. 12 — Flight envelope for the PW-141.II - aircraft masses: M_{max}= 69 kg; M_{min}= 36 kg; Load coefficients: manoeuvre: n_{max}= 6, n_{min}= -3, from gusts n_{max}= +6.324 (+10.699), n_{min}= -3.872 (-7.428); design speeds [EAS]: V_{S1}= 75.42 km/h, V'_{S1od}= 96.52 km/h, V_A= 185km/h, V_C= 190 km/h, V_D= 250 km/h, V_G= 167.2 km/h

A discretisation of the aerodynamic load for the tail unit was done in the same manner.

5 Numerical analysis of the strength structure

Strength analysis of the lifting surface was done by the MD NASTRAN system, basing on the on the earlier prepared discrete model. Support of the model was done by attaching (in fiction way) the centre of aircraft mass node. Focused forces set in the model nodes, simulated aerodynamic and mass load extreme distributions for the cruise speed VC and diving speed VD as well. The calculation results were given by elaboration of the node displacement from the static equation.

$$\{q\}=[K]^{-1}\{F\} \quad (3)$$

In turns, for the every j-element a tensor of stress was elaborated from the formula

$$\{\sigma_j\} = [Q_j]\{\varepsilon_j\} = [Q_j][B_j]\{q_j\} \quad (4)$$

where $\{q\}$ — vector of the node displacements, $[K]^{-1}$ — global mass of the flexibility (a reverse matrix to the global matrix of the stiffness), $\{F\}$ — vector of the external loads, $[Q_j]$ — matrix of the element stiffness, $\{\varepsilon_j\}$ — deflection tensor, $[B_j]$ — matrix of the element derivatives of the shape function. Visualisation of the results was presented in the form of displacement and stress distributions generated by the Patran post-processor.

6 Conclusion

The strength analysis for the PW-141.II UAV structure being under extreme load for velocity: V_D and V_C pointed out, that the structure is loaded in proper way and is safe. Current strength R_m for a specific composite used in the UAV design is in the range from 1300MPa to 3000MPa, which does quarantee a structural safety. Elaborated stresses, due to deliberately decreased values, recommend usage of the lighter composites with smaller number of the layers, however the final decision should be made after the static ground tests.

References

[1] *European Aviation Safety Agency Certification Specifications for Very Light Aeroplanes CS-VLA*

[2] German J.: *Podstawy mechaniki kompozytów włóknistych*; Politechnika Krakowska, Kraków 1996

[3] Miranda L. R., Elliott R. D., Baker W. M.: *A Generalized Vortex Lattice Method for Subsonic and Supersonic Flow Applications*; NASA Contractor Report 286

[4] Ochelski S.: *Metody doświadczalne mechaniki kompozytów konstrukcyjnych*; WNT, Warszawa 2004

[5] Rakowski G., Kacprzyk Z.: *Metoda elementów skończonych w mechanice konstrukcji*; Oficyna Wydawnicza Politechniki Warszawskiej, Warszawa 1993

[6] Reymond M., Miller M.: *MSC/NASTRAN Quick Reference Guide version 68*; The MacNeal-Schwendler Corporation, Los Angeles, CA 1994

[7] *MSC Documentation Library - MSC Nastran, MSC Patran*; Combined documentation 2005

Editorial Note: The formerly mentioned pictures (Figs. 13 and 14) are printed on the inner back page of this issue in colour for better clarity.

Simulation of Rigid Projectile Impact on the Real Aircraft Structure

Simulace nárazu tuhého projektilu na reálnou leteckou konstrukci

Ing. Radek Doubrava, Ph.D. / VZLÚ, Plc., Prague

This article discusses prediction of the impact behaviour of a rigid projectile immediately after the impact on an aluminium plate. The result was verified on the real aircraft structure damage. 3D digitizing system was used for comparison between FE calculation and real structure damage.

V článku je diskutovaná predikce vlivu tuhého projektilu po dopadu na plech z hliníkové slitiny. Výsledky byly ověřeny na poškození reálné konstrukce. Pro porovnání výsledků simulace a reálně poškozené konstrukce byl použit 3D digitalizační systém.

Keywords: rigid projectile impact, aircraft structure, FE calculation, 3D digitizing.

Introduction

The model that will work best for a given real world problem depends on a number of factors, including structural loading, impact velocity and boundary conditions. In the service of an aircraft there exists a risk of emergency cases from the point of view of unforeseeable circumstances (e.g. bird strike, sucked impurities to the engine etc.), or owing to human factor (e.g. projectile, missiles etc). In these cases it is necessary to ensure or minimize damage from the point of view health. An impact simulation is an important tool for all industries as development cycles decrease.

Problem description

The projectile in this simulation is standard military geometry of caliber 23mm. Figure 2 shows typical geometry of projectile and geometry model from CAD.

The projectile and the skin for simulation are meshed by means of shell elements in the FEAMP pre-processor and transformed into the ABAQUS/CAE.

Fig. 1 — Damage of aircraft structure after impact of a military projectile

Material model for structure simulation

The 2024-T3 aluminium Johnson-Cook failure strain model has been used for structure simulation [4]. The Johnson-Cook

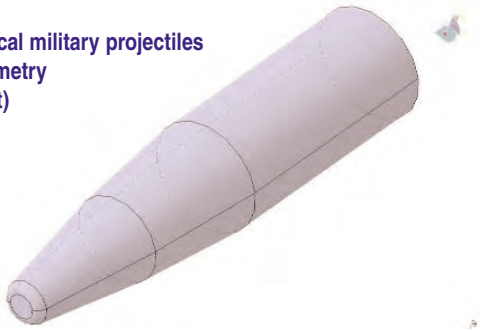

Fig. 2 — The typical military projectiles (above) and geometry model CAD (right)

flow surface is defined:

$$\sigma_y(\varepsilon_p, \dot{\varepsilon}_p, T) = [A + B(\varepsilon_p)^n][1 + C\ \ln(\dot{\varepsilon}_p^*)][1 - (T^*)^m] \quad (1)$$

where A, B, C, n and m are constants.

Failure accumulation in the Johnson-Cook model does not directly degrade the yield surface. The model, more fully described in reference [4], defines the strain at fracture where the ratio of the pressure to the effective stress is:

$$\varepsilon^f = (D_1 + D_2 \exp(D_3\eta))(1 + D_4 ln\dot{\varepsilon}^*)(1 + D_5 T^*) \quad (2)$$

Fracture occurs in the Johnson-Cook model when the damage parameter D exceeds 1.0. The evolution of D is given by the accumulated incremental effective plastic strains divided by the current strain at fracture

$$D = \sum \frac{\Delta\bar{\varepsilon}^p}{\varepsilon^f} \quad (3)$$

The values for Johnson-Cook material model of 2024-T3 alloy are in Table 1.

material:	2024-T3		
Elastic	E=	74000	MPa
	ν=	0,33	
	ρ=	2,77E-09	t/mm^3
Johnson-Cook constants	A=	368,9	MPa
	B=	683,9	MPa
	C=	0,0083	
	m=	1,7	
	n=	0,73	
Johnson-Cook failure	D_1=	0,112	
	D_2=	0,123	
	D_3=	1,5	
	D_4=	0,007	
	D_5=	0	

Tab. 1 — The constant for 2024-T3 aluminium Johnson-Cook material model [4]

A general contact algorithm was used for the definition of contact interactions. The simulations were performed using VUMAT subroutine [2].

Ballistic limit verification

Figure 3 shows FE model of projectile with an initial velocity specified in the direction normal to the plane of the plate elements.

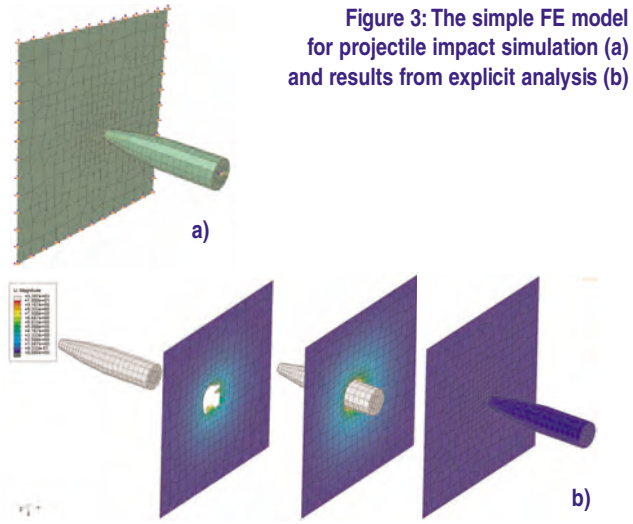

Figure 3: The simple FE model for projectile impact simulation (a) and results from explicit analysis (b)

Figure 4 shows comparison between experimental ballistic limit [1] and FE simulation of 2mm skin thickness projectile impact.

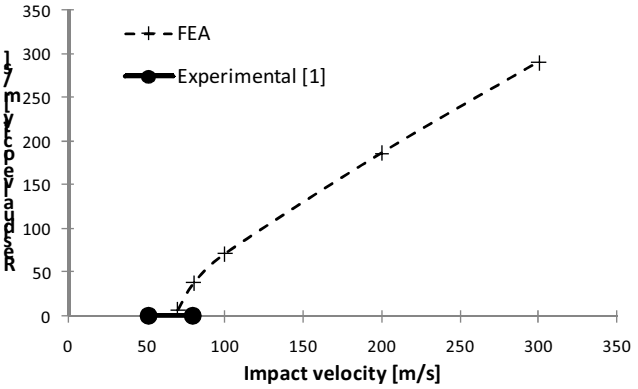

Fig. 4 — Comparison between experimental ballistic limit [1] and FE simulation of real projectile

Application to the real aircraft structure

The experience obtained from simple model, such as damping coefficient, friction value, strain rate etc., was used for simulation of real aircraft structure. The real damage of the horizontal tail plane was measured by photogrammetric technique (see Figure 5).

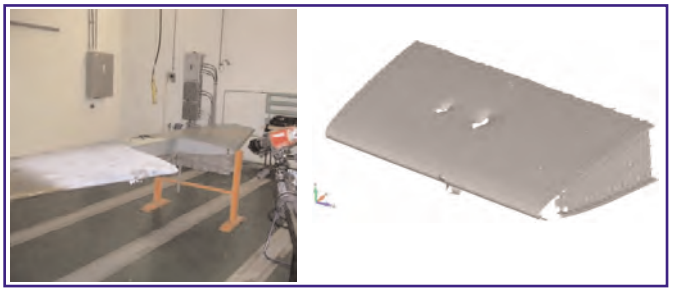

Fig. 5 — Measurement of real aircraft structure after damage

Figure 6 shows general FE model of aircraft and refine mesh for impact simulation. The numerical model consisted of 10472 elements (9295 nodes). The model including real

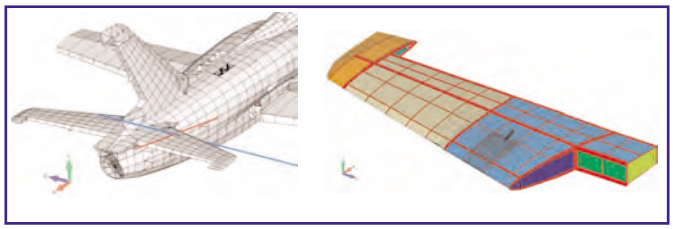

Fig. 6 — The general FE model of aircraft and refine mesh for impact simulation

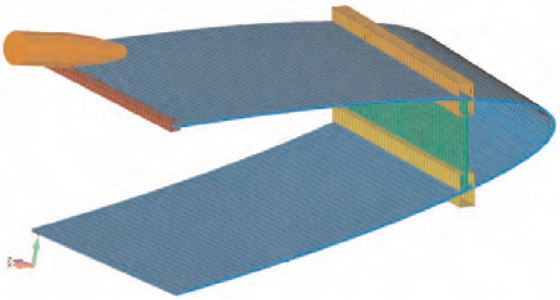

Fig. 7 — Detail of FE model for impact simulation on the real aircraft structure with property visualization

inner structure parts such as webs, ribs, and stringers.

The velocity of projectile was defined on the bases of military standard MIL-STD-662F [3]. Table 2 shows projectile velocity on the base of target distance. For simulation was used 547.1m/s initial velocity accordant with 1000m target distance. Figure 8 shows the influence of projectile impact on the real aircraft structure and especially on the inner parts of structure.

Figure 9 shows comparison between measured damage surfaces of aircraft structure and FE analysis.

Target distance [m]	Remaining velocity 23mm API-T BZT SOVIET	
	feet/s	m/s
0		
100	3110	947,9
200	2990	911,4
300	2790	850,4
400	2640	804,7
500	2490	759,0
600	2350	716,3
700	2205	672,1
800	2065	629,4
900	1925	586,7
1000	1795	547,1

Tab. 2 — Velocity of projectile [3]

Figure 10 shows change of projectile velocity during impact on the parts of aircraft structure.

Conclusion

This paper describes a technique of modelling of projectile impact using FE model for real structures damage evaluation. The result shows good agreement between outer surface measurement and FE calculation. Although this work is only a first approximation, and implemented in relatively simplified terms, this method of finding damage propagation is applicable for:

- diagnostics of airframe damage — scanning of aircraft surface, photogrammetric system application etc.,
- structure repair evaluation — damage of inner structure, composite path application etc.,
- service operations — visual inspection.

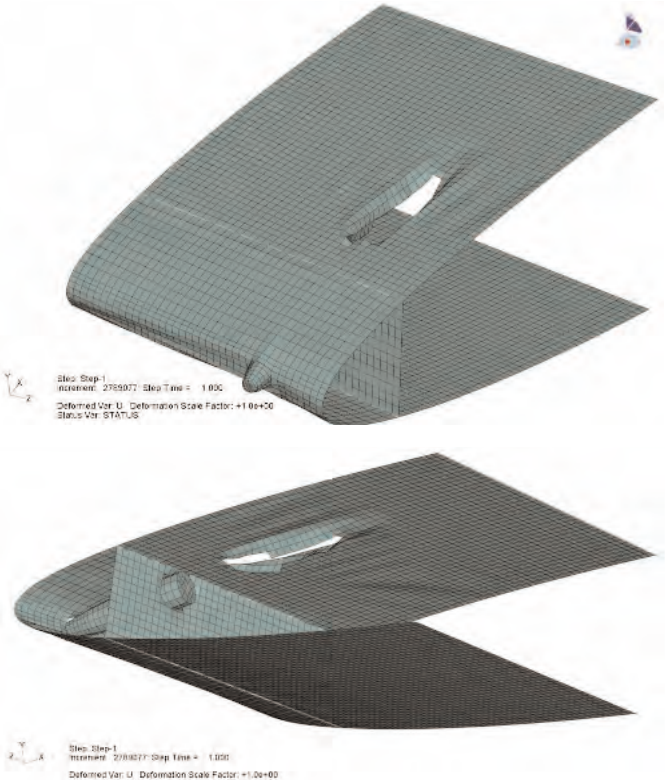

Fig. 8 — Detail of damage outer and inner parts of structure during projectile impact simulation

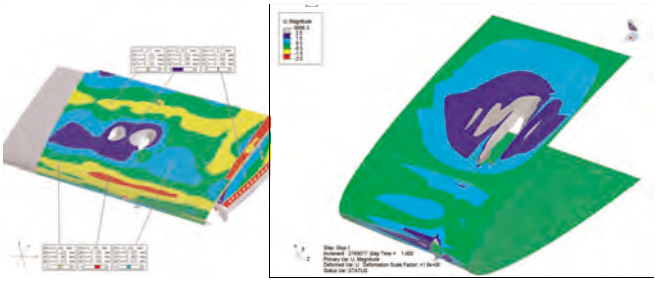

Fig. 9 — Comparison displacement contour map between measurement (left) and FE simulation (right)

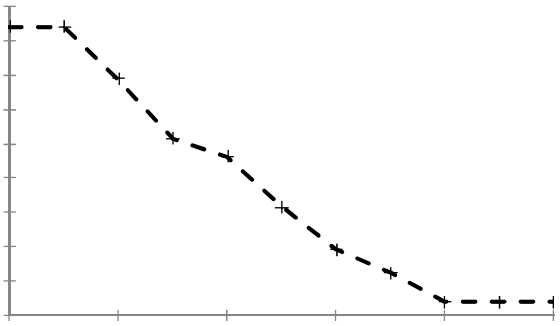

Fig. 10 — The change of projectile velocity after impact on the parts of aircraft structure

References

[1] Khan, W U, Ansari, R.: *Oblique Impact of Projectile on Thin Aluminium Plates*; Defence Science Journal, Vol. 53, No. 2, pp. 139-146, 2003

[2] ABAQUS v.6.7.5 Manuals, Dassault Systems 2008-10-14

[3] MIL-STD-662F: *V50 Ballistic Test for Armor*

[4] DOT/FAA/AR-03/57: *Failure Modelling of Titanium 6Al-4V and Aluminium 2024-T3 with the Johnson-Cook Material Model*

Wind Tunnel Research of Wingtip Devices

Výzkum konců křídla v aerodynamickém tunelu

Jan Červinka, Zdeněk Pátek / VZLÚ, Plc., Prague

Experimental model of straight higher-aspect ratio wing with eight different wingtips was studied at low-speed wind tunnel. Systematic study of wingtip influence provided fundamental experimental data concerning the possibilities to influence aerodynamic characteristics of wing by its wingtip devices, especially the characteristics difficult to compute. The data serve also for validation and setting of the calculation methods.

V nízkorychlostním aerodynamickém tunelu byl zkoušen experimentální model přímého křídla větší štíhlosti s osmi různými variantami řešení jeho konce. Systematické studium vlivu konce křídla na aerodynamické charakteristiky posloužilo k získání základních experimentálních dat o možnosti ovlivnění aerodynamických charakteristik křídla různým řešením jeho konce, zejména těch charakteristik, které se obtížně výpočetně předpovídají. Data poslouží rovněž pro nastavení a validaci výpočetních metod.

Keywords: wingtip, wingtip device, wing, aerodynamics of wing.

Nomenclature

c_C	crosswind force coefficient (aerodynamic axis system)
c_D	drag coefficient (aerodynamic axis system)
c_L	lift coefficient (aerodynamic axis system)
c_l	rolling moment coefficient (body axis system
c_m	pitching moment coefficient (body axis system)
S	wing area, m^2
α	angle of attack, deg
β	sideslip angle, deg

1 Introduction

Possibility to influence the aerodynamic performance of a wing by using shaped wingtips has been known for decades [1] [2] [3], for example F. Lanchester patented the endplate even in 1897. A new impulse was given by Whitcomb work [4] and since then increasing attention is continuously paid to this specific area of the wing design. But there is lack of published validated best-practice approaches for their design, rare exception is presented by ESDU [5], that is focused mainly on large transport aircraft.

In general, the different wingtip devices are concisely attributed with increase of the efficient wing aspect ratio, which manifests primordially by the reduction of the induced drag and by the increase of the maximum lift. This supposition is generally correct but the resulting global aerodynamic performance of a wing with different wingtip devices is not so evident because the criteria could be various. It is necessary to include the total drag, but for example also the lateral characteristics, etc. Sometimes also the literary sources give different results even for very similar cases. In addition, also other than aerodynamic considerations (strength, flutter, ...) shall be taken into account in a comprehensive winglet assessment.

The aim of the presented testing was basic comparison of the influence of several wingtips on global aerodynamic performance. The wingtip devices were intentionally chosen as distinctively different, from simple extension of span to specifically designed dedicated winglet. The studied straight wing corresponds to low-speed commuter or general aviation aircraft.

2 Wing model and testing

2.1 Basic wing

A model of a turbulent wing of a generic aircraft of general aviation category was used. The supposed aircraft is twin turboprop of business category with cruise speed of approx. 400 kph (210 kts).

Basic geometric characteristics of the wing are given in Tab. 1 below:

Span	2.0125 m
Area	0.3937 m^2
Mean geometric chord	0.1997 m
Aspect ratio	10.29
Taper ratio	0.60
Geometric twist angle	-3.4°
Dihedral	1.5°
Airfoil section - root	max. thick. 17 %
airfoil section - tip	max. thick. 13 %

Tab. 1

2.1 Wingtip devices

Eight wingtip devices including basic conventional wingtip were tested. The general description is given in the following section, their principal geometric characteristics are presented in Tab. 2. The views of wingtips are presented in Fig. 1 to Fig. 8.

Wingtip 1

Basic conventional wingtip, it was used as a reference configuration.

Wingtip 2

Extended span, its planform shape smoothly continues the planform shape of basic wing.

Wingtip 3

Extended span, the shape of the extension is in the form of the simple winglets 4, 5 and 6, i.e. swept tapered surface with the root chord equal to the tip chord of the basic wing. The tip airfoil section is of the same family as the root airfoil section.

Wingtip 4

Simple winglet, cant angle 43.5 deg upwards (i.e. approx. 45 deg to the horizontal level). In principle, the wingtip 3 with nonzero cant angle.

Fig. 1

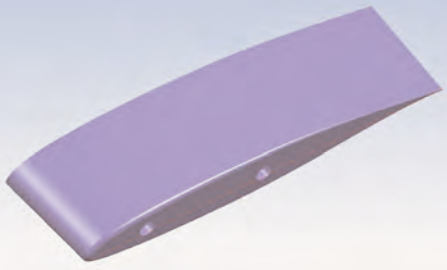

Fig. 2

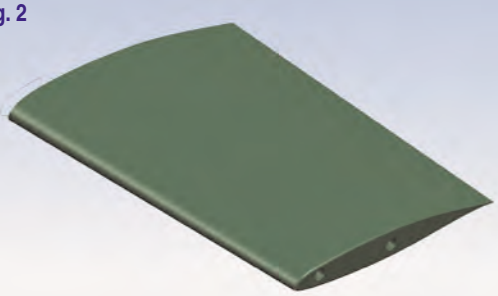

Fig. 3

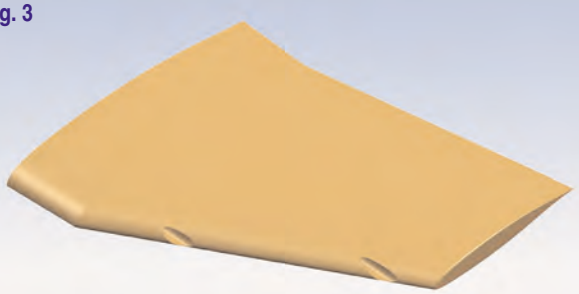

Fig. 4

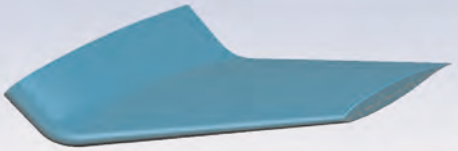

Fig. 5

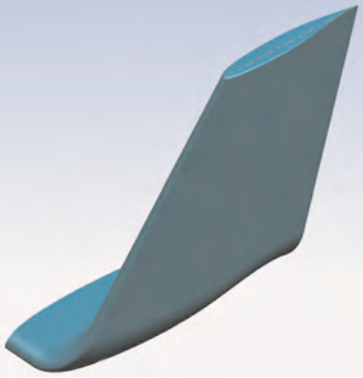

Fig. 6

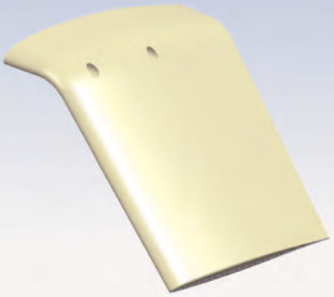

Fig. 7

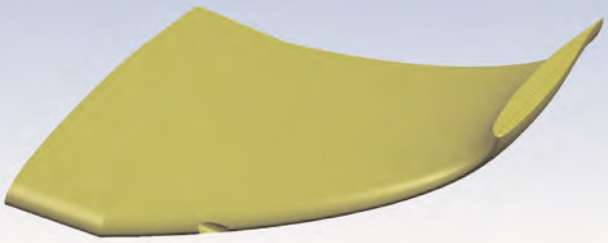

Fig. 8

Wingtip 5

Simple winglet, cant angle 85 deg upwards (i.e. approx. 90 deg to the horizontal level). In principle, the wingtip 3 with nonzero cant angle.

Wingtip 6

Simple winglet, cant angle 47 deg downwards (i.e. approx. 45 deg to the horizontal level). In principle, the wingtip 3 with nonzero cant angle.

Wingtip 7

Winglet of elliptical front projection, the cant angle of the tip edge 85 degrees. The tip airfoil section is the same as the root airfoil section. This winglet represents blended winglets.

Wingtip 8

Dedicated winglet, designed particularly to enhance the basic wing. Specific airfoil sections are used along the winglet length (span).

Wingtip	1	2	3	4	5	6	7	8
Relative wingspan	1.00	0.146	0.146	0.109	0.017	0.105	0.132	0.039
Relative wing area	1.00	0.104	0.087	0.065	0.002	0.063	0.079	0.013
Relative winglet length	0.00	0.146	0.146	0.151	0.151	0.151	0.169	0.139
Relative winglet area	0.00	0.104	0.087	0.090	0.090	0.090	0.101	0.047
Relative chord - root	-	1	1	1	1	1	1	0.55
Relative chord -tip	1	0.90	0.61	0.61	0.61	0.61	0.61	0.36
Sweep at LE	3.32	3.32	30	30	30	30	33	30
Cant of wingtip	0	0	0	43.5	85	-47	85	75
Toe of wingtip	0	0	0	0	0	0	0	0
Twist of wingtip	-0.14	-0.64	-0.64	-2	-2	-2	-2	-2

Table 2 Nomenclature

Relative wingspan	wingspan to basic wingspan ratio
Relative wing area	wing area to basic-wing area ratio
Relative winglet length	winglet length to basic wingspan ratio
Relative winglet area	winglet area to basic-wing area ratio
Relative root / tip chord	root / tip winglet chord to basic-wingtip chord
Cant	angle between basic plane of wing and the basic plane of wingtip
Twist	negative twist means lower angle of attack of the tip than of the root

2.2 Test setup

Wind tunnel

The testing was performed in the 3mLSWT low-speed wind tunnel of VZLÚ Aeronautical Research and Test Institute. The test section is of 3 m diameter.

The model of a wing was hinged on a sting manipulator that allowed change of angle of attack and of sideslip angle as well in desired ranges.

The forces acting on the model were measured by an internal six-component strain-gauge balance.

Testing

The tests were performed as sweep at continuously changed angle of attack and constant sideslip angle.

Reynolds number of the tests was $0.7 \cdot 10^6$ (related to the mean aerodynamic chord), Mach number was 0.16

The usual low-speed wind tunnel corrections were applied on the measured data.

3 Results

To ease correct comparability of the results of the different wingtips, all results are presented in the form of aerodynamic coefficients related to joint reference quantities. The values of the span, area and mean aerodynamic chord of the basic wing were used as reference quantities for all coefficients of all evaluated wing configurations.

3.1 Extended span vs. simple winglet

Comparison of the basic wing (wingtip 1), two wings with extended span (wingtips 2 and 3) and a wing with simple vertical winglet (wingtip 5) is presented in Fig. 9.

Purely from aerodynamic point of view, smooth extension of span (wingtip 2) is the most efficient solution. It reaches higher maximum lift coefficient and better value of c_L/c_D for most c_L.

The extension of span (wingtip 3) in the same geometric shape as the simple winglet is more advantageous than the nearly vertical winglet (wingtip 5) in terms of lift and drag. The exemption is visible between c_L of about 0 to -0.3 where the simple winglet is featured by slightly lower c_D, in the order of 0.001, but this c_L range is of very low practical importance.

The change in the position of the wing aerodynamic focus was observed, the span extension induces moderate forward shift of the aerodynamic focus.

The installation of the winglet is accompanied by the evident change of lateral aerodynamic characteristics, the absolute values of the derivatives of c_C, c_l, by β are much higher.

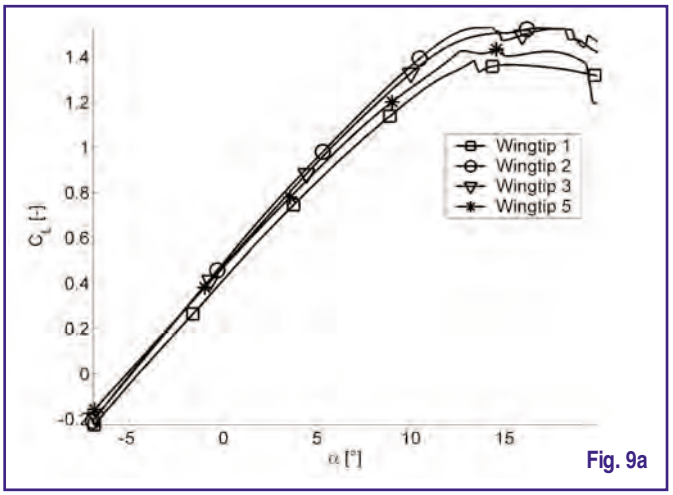

Fig. 9a

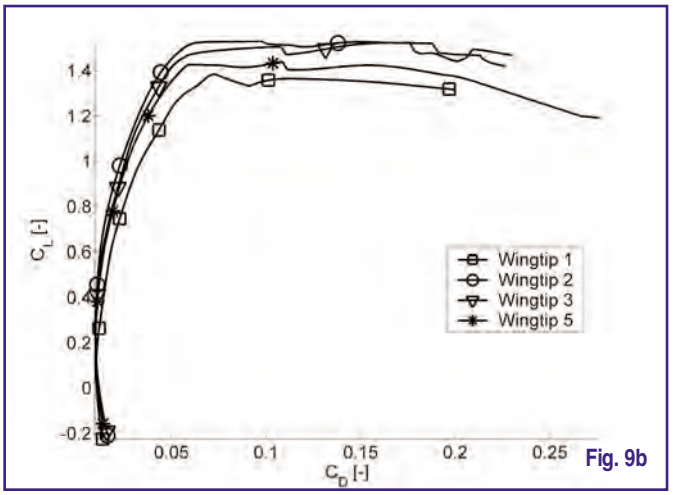

Fig. 9b

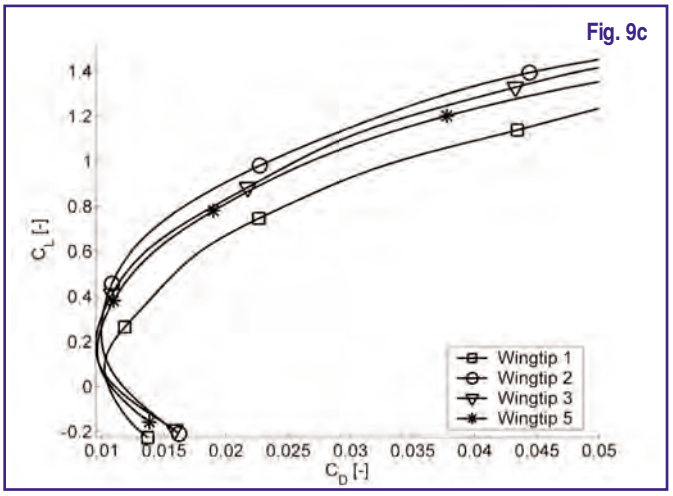

Fig. 9c

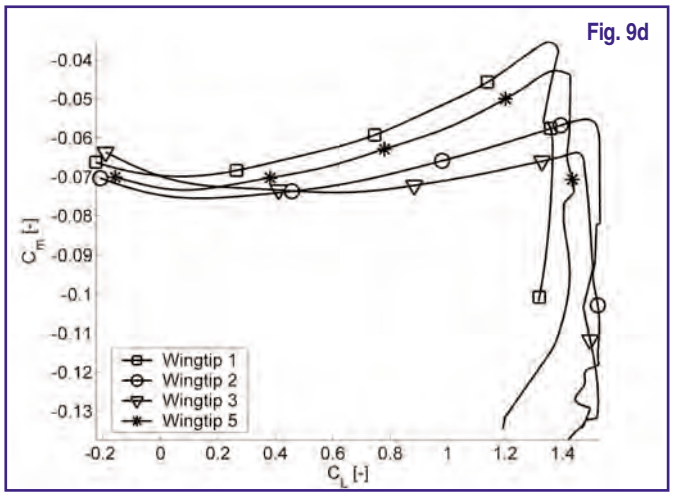

Fig. 9d

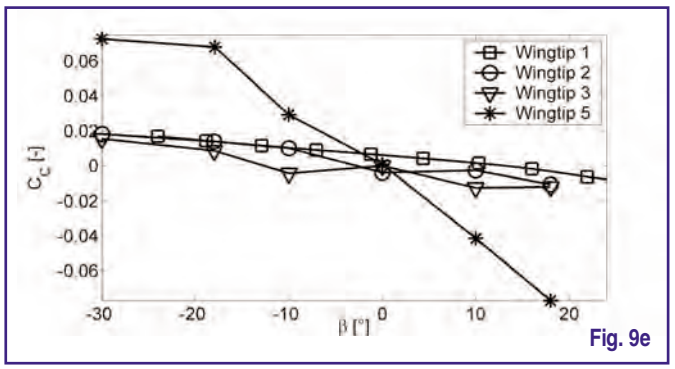

Fig. 9e

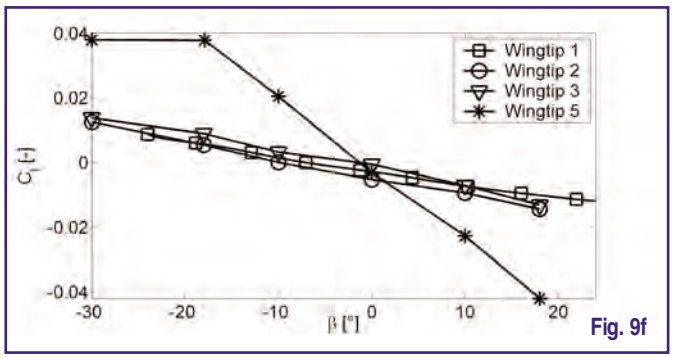

Fig. 9f

3.2 Extended span vs. dedicated winglet

The extended spans (wingtips 2 and 3) are compared with the dedicated winglet (wingtip 8) in Fig. 10.

The dedicated winglet provides lower maximum attainable c_L than any of the studied extended spans, its c_D is generally higher than with wingtip 2 and comparable with wingtip 3. It is possible to design dedicated winglet to obtain very low c_D for certain given low c_L, even lower c_D than with wingtip 3. The wingtip 2 is penalized at low c_L by high friction drag of largest wetted area.

The influence on lateral characteristics is smaller for the dedicated winglet than for the simple winglet, it is done by smaller lateral projection of the dedicated winglet area.

3.3 Influence of cant angle

Simple winglets of the identical trapezoidal form but different cant angle were investigated (wingtips 3, 4 and 5), Fig. 11.

The identical tendency as mentioned in 3.2 is observed. Regarding the efficiency, the extension of span (cant angle close to zero) is the best solution, mainly as far as maximum lift coefficient concerns. But winglet 45 deg up is very close and maybe with slightly better c_D in certain areas of c_L.

The span extension practically does not influence the lateral characteristics compared to the basic wing. The presence of winglets, with relatively large lateral projection of their area, is obviously pronounced much more.

3.4 Simple winglet up vs. simple winglet down

The basic wing (wingtip 1), a simple winglet 43.5 deg up (wingtip 4) and a simple winglet 47 deg down (wingtip 6) are compared in Fig. 12.

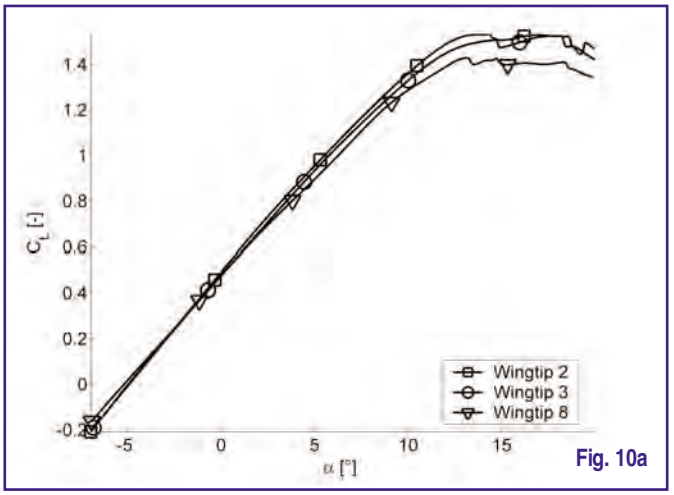

Fig. 10a

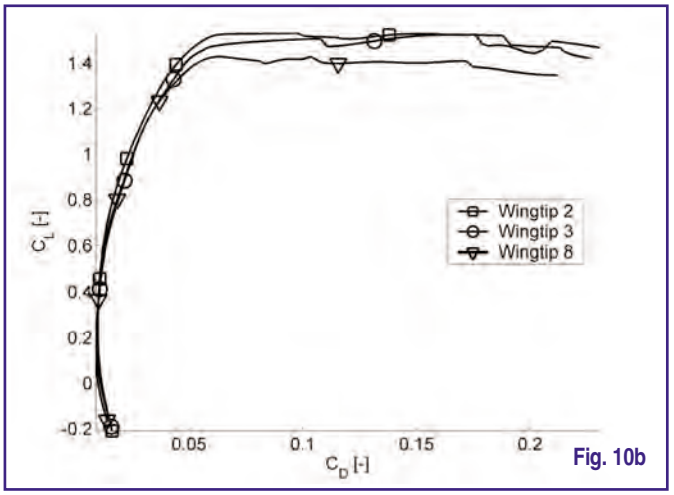

Fig. 10b

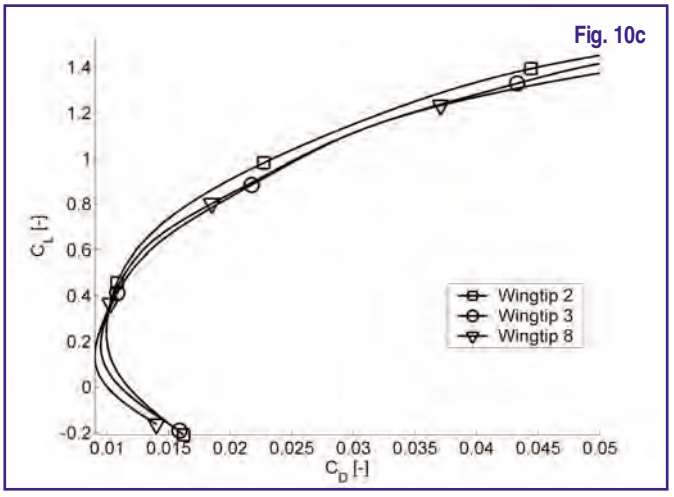

Fig. 10c

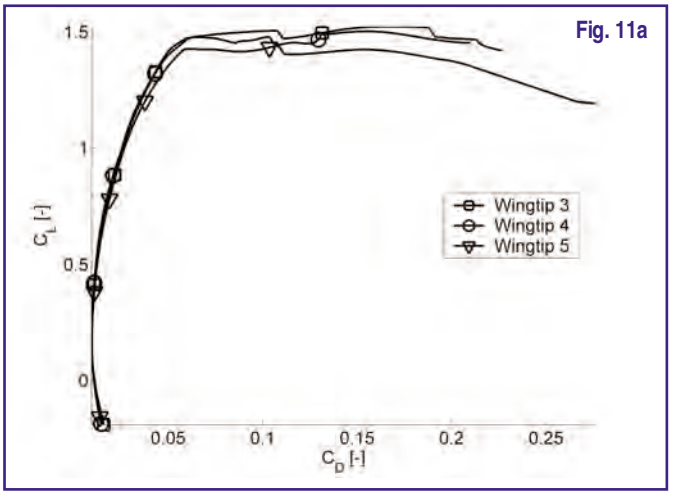

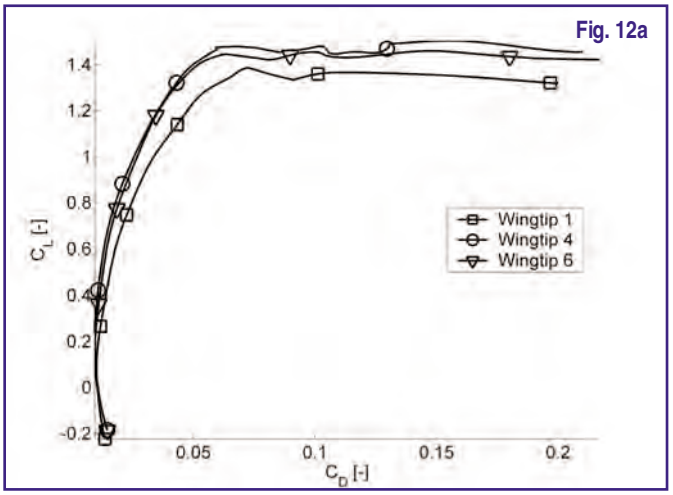

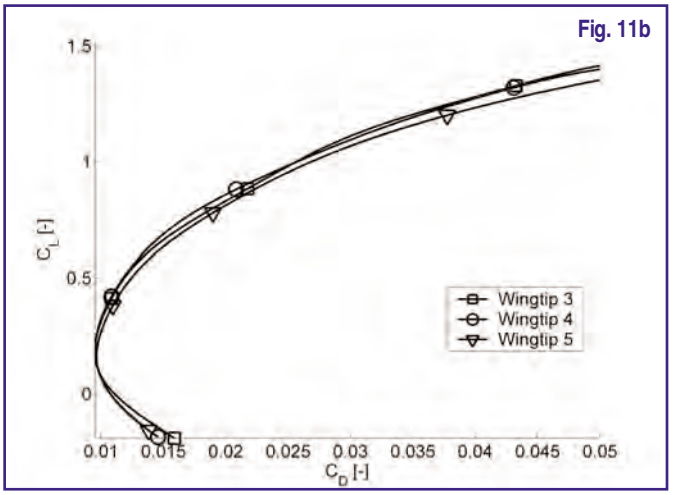

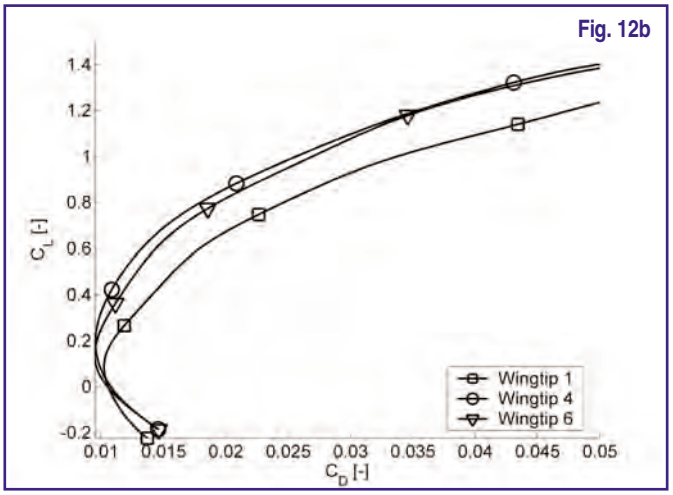

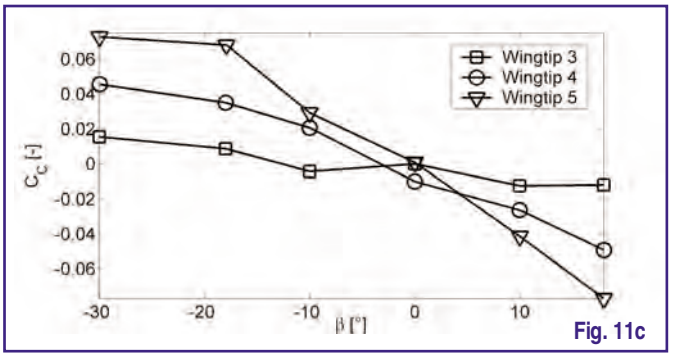

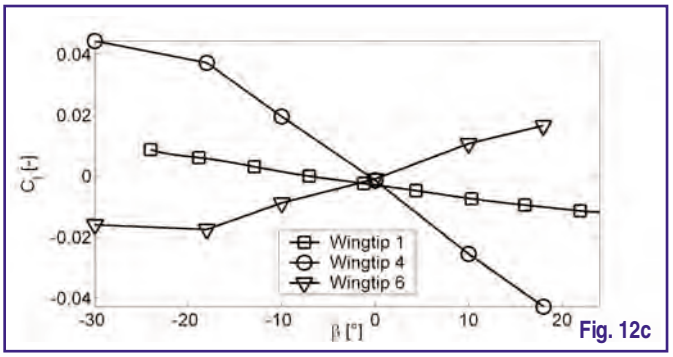

The main difference consists in drag, the wing with winglets up features systematically lower c_D for c_L higher than 0.17, the difference is in the order of 0.001.

As far as lateral characteristics concerns, the winglet down, opposite to the winglet up, weakens the lateral stability regarding the bank angle. It is illustrated by the fact that the c_l vs. β curve has inverse slope.

3.5 Elliptically blended winglet

Three winglets with identical length but different shapes in front projection were evaluated (Fig. 13) — simple nearly vertical winglet (wingtip 5), blended winglet with elliptical front view elevation (wingtip 7) and the dedicated winglet (wingtip 8).

Elliptically blended winglet proves to be aerodynamically most advantageous, from the point of view of maximum lift and the drag as well. In addition to it, the lateral aerodynamic consequences of its installation are very moderate.

The reason is that this winglet is aerodynamically close to the implementation of simple span extension, the relative wingspan is nearly identical with extended span (wingtips 2 and 3).

The Fig. 14 compares the elliptically blended winglet (wingtip 7) with the extended span (wingtip 3) and the simple winglet 43.5 deg up (wingtip 4). It is remarkable that the aerodynamic characteristics of wingtips 3, 4 and 7 are very close in general. But the blended winglet shows lower drag at least at low positive lift. The penalty is much complex shaping together with the wingspan very close to the simply extended span, on the other side the blended winglet provides certain influence on lateral characteristics that could be purposely managed.

Comparison of the elliptically blended winglet (wingtip 7) with the dedicated winglet (wingtip 8) is given in Fig. 13. The blended winglet features higher maximum lift. From point of

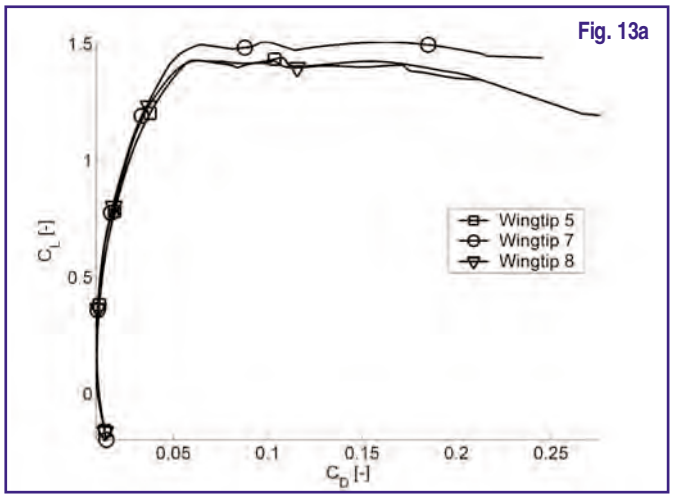

Fig. 13a

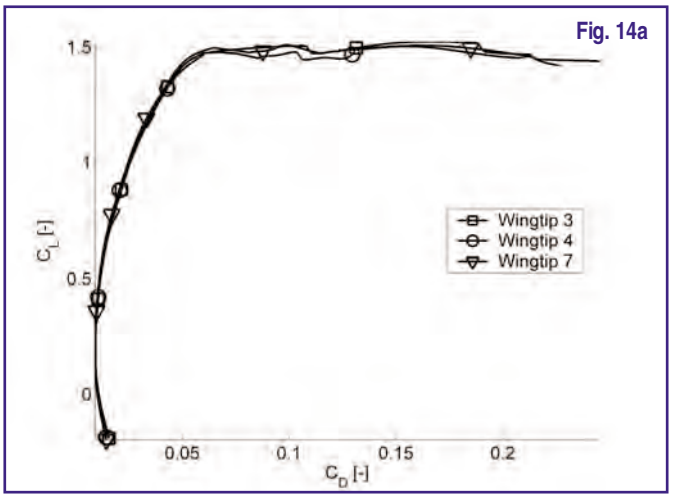

Fig. 14a

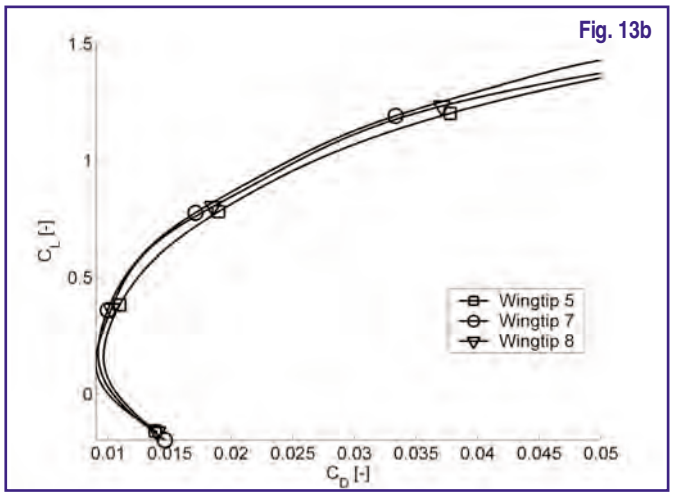

Fig. 13b

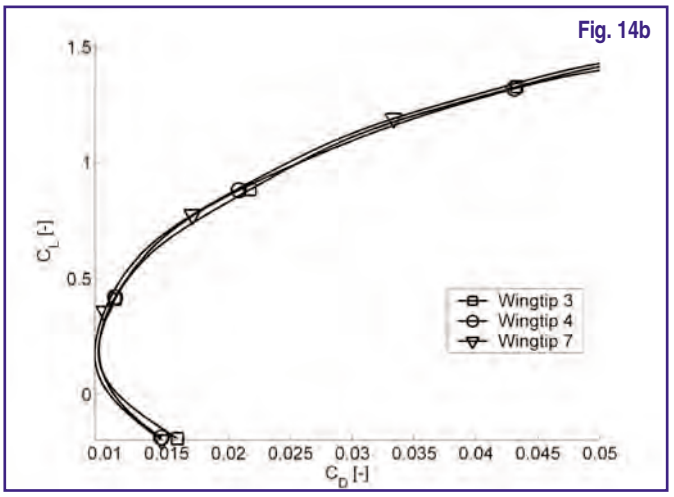

Fig. 14b

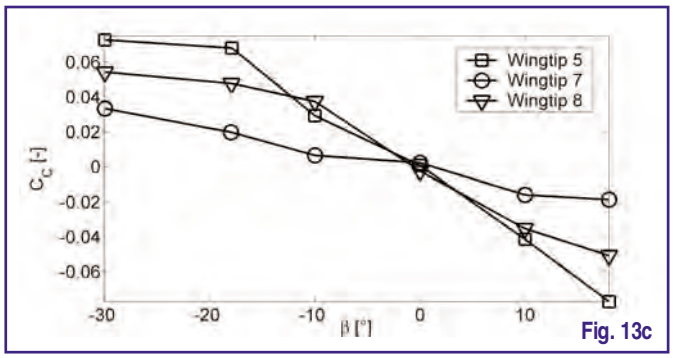

Fig. 13c

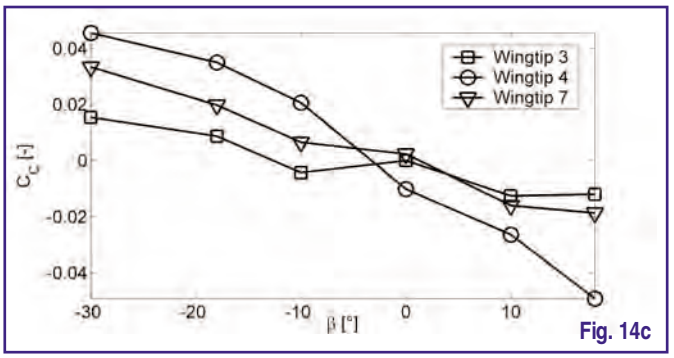

Fig. 14c

view of drag, the results are similar in the both cases, it is possible to design the both devices to very low drag at certain narrow area of lift. The dedicated winglet pronounces more influences on the lateral aerodynamic characteristics. It has the advantage of distinctly shorter total wingspan that could be the decisive criterion.

4 Conclusions

Experimental research of systematically developed series of wingtip devices shows several fundamental facts ((and partly also confirms known issues):

Extension of span is usually the most efficient solution from the point of view of global aerodynamic characteristics. In relation with this fact, the wingtip device with low cant angle is more efficient than with high cant angle.

The wingtip inclined up (with positive cant angle) is aerodynamically more advantageous than the wingtip inclined down.

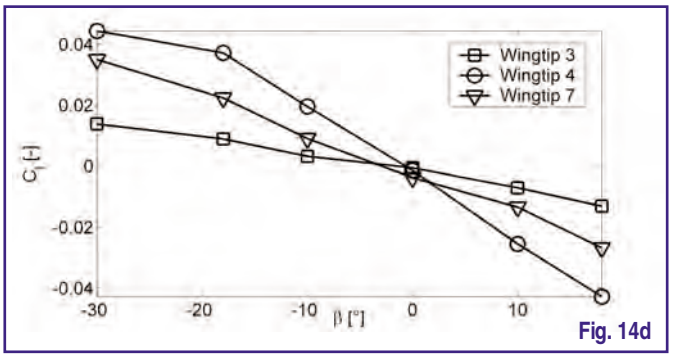

Fig. 14d

Elliptically blended winglet is an efficient tool that can be suitable for very low drag at selected narrow area of lift.

Complex dedicated winglet features similar possibilities as blended winglet, but at shorter wingspan. Its influence on the lateral characteristics of the wing is more pronounced.

Acknowledgments

The research was supported by the MSM0001066901 *Applied external aerodynamics development* (*Rozvoj aplikované vnější aerodynamiky*) project supported by the Ministry of Education, Youth and Sports of the Czech Republic.

References

[1] Rebuffet, P.: *Aérodynamique expérimentale*; Librairie polytechnique Ch. Béranger, Paris et Liege, 1945
[2] Schlichting, H., Truckenbrodt, E. A.: *Aerodynamik des Flugzeuges*; Springer Verlag, Berlin, 1960
[3] Hoerner, S.: *Fluid Dynamic Drag*; Hoerner Fluid Dynamics, Bakerfield, 1965
[4] Whitcomb, R.: *A Design Approach and Selected Wind-Tunnel Results at High Subsonic Speeds for Wing-Tip Mounted Winglets*; NASA TN D-8260, 1976
[5] -, *Aerodynamic Principles of Winglets*, ESDU 9813, Engineering Sciences Data Unit, 1998

Cooling of Electronics Installed in Passenger Seats of Civil Aeroplanes and its Testing

Chlazení elektroniky instalované v sedadlech cestujících v dopravních letounech

Jiří Myslivec / VZLÚ, Plc., Prague

Airlines offer ever more and wider range of electronic services installed on passenger seats. Every electronic appliance works with loss of power changed into heat. This heat has to be dissipated. In European project COSEE the cooling of seat electronics was solved by help of Loop Heat Pipes that conduct the heat into the seat construction. A VZLU test laboratory participated in solution to the problem by testing prototypes installed in seats.

Letečtí dopravci nabízí cestujícím stále širší rozsah elektronických služeb na sedadlech cestujících. Každá elektronika pracuje se ztrátovým výkonem, který je nutno odvádět. V evropském projektu COSEE bylo řešeno chlazení elektroniky tím způsobem, že tepelné trubice odvádí teplo do konstrukce sedačky cestujících. Zkušební laboratoř VZLU se na řešení úkolu podílela v etapě vývoje metodik zkoušek a vývojových zkoušek prototypů instalovaných na sedadlech.

Keywords: SEB (Seat Electronic Box), LHP (Loop Heat Pipe), construction conductivity.

1 Introduction

Aircraft of new generation are equipped by new state-of-the-art devices for *in-flight entertainment* (IFE) of passengers. Dynamic growth of these devices is due to competitive pressures by airlines and producers of aircraft, by higher requirements of travellers on utilizing long time flights for entertainment, information or fulfilling of working tasks, and further it is the result of general technical progress in electronics.

IFE equipment of new generation: in seat interactive audio/video on demand, broadband internet, games, mobile phones, onboard shopping, 3D graphics (interactive moving map), E-commerce and so on. Control of these equipments is concentrated in *Seat Electronic Box* (SEB) placed on seats of passengers.

Due to physical laws every electronic equipment works with limited efficiency and these losses caused heating of SEB. Cooling of SEB was the objective of European project COSEE (*Cooling of Seats Electronic Boxes and Cabin Electronics*).

The following laboratories took part in the COSEE project: France — Thales and INSA, Germany — USTUTT and Recaro, Belgium — EHP, Russia — ITP, Italy — Avio Interiors, Czech Republic — VZLU.

2 Methods of SEB cooling

Cooling of the other electronic boxes on the aircraft (radio and navigation equipment etc.) is made by forced convention provided by the aircraft, which is possible because these devices are not placed in passenger cabins.

Total average heat losses dissipated by SEB boxes in an aircraft for 300 passengers will be approximately 5 kW, maximum up to 10 kW.

Possible ways of SEB cooling:

a) Forced convention is not available for SEB
b) Natural convention has limited power dissipation
c) Integrated fans cause extra cost, noise and flow of air when multiplied by the SEB number, lower reliability and higher maintenance
d) Heat pipes and phase change systems adequately integrated into the seat structure would provide a reliable and efficient alternative to fan cooling

3 LHP technology, components and operation

Loop Heat Pipe (LHP) principle: working fluid comes into evaporator in liquid phase, there absorbs the heat and changes in vapour phase and goes into condenser, working fluid cools and changes in water phase. Cooling process in this loop works without supply of energy and is very reliable. *Heat Pipe* (HP) principle is similar but only inside of one pipe, on one end of HP is evaporator and on the opposite end is condenser.

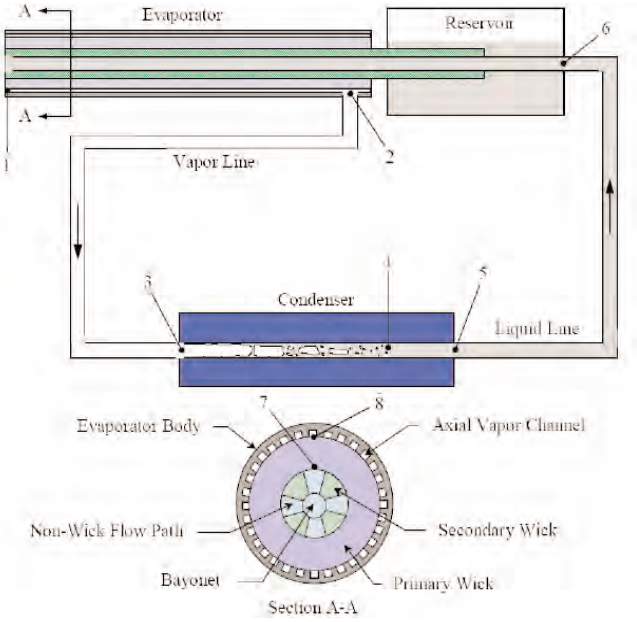

Fig. 1 — Loop heat pipe

The objective of COSEE project was to develop and integrate an advanced cooling technique based on heat pipes located between the seat structure and SEB through:

+ Evaluation and thermal simulation of the heat dissipation capability of the different cooling options.
+ Design and development of a specific and reliable heat pipe adopted to aerospace conditions.
+ Adaptation of the equipment and seat structure to optimize use of the new cooling technique.
+ Performance evaluation on mock-up according to aeronautical specifications.

Performance	Proposition of requirement for COSEE LHP
Operating T° range	-15°C to 55°C
Heat sink operating T° range	-15°C to 55°C
Non operating T° range	-55°C to 85°C
Maximal heat load	100 W
Minimal start-up heat load	20W
Heat flux density at evaporator	4 W/cm² (TBC)
Altitude Pressure	15,000 feet
Fluid leak rate	< $3*10^{-7}$ cc/sec at +20°C for each connection
Life time	25 years
Mass	Shall be minimized
Evaporator and condenser saddles flatness	0.2 mm (TBC)
Evaporator and condenser saddle roughness	1.6 µm
Length between evaporator and condenser	max 700 mm
Vertical distance between evaporator and condenser	500 mm
Installation requirements	The liquid and vapor tube shall be flexible to follow enough the seat structure (minimal bending radius of 10 mm)

LHP specifications

4 Performance evaluations

Performance evaluation was carried out at normal conditions, higher temperatures, linear acceleration and vibrations. Cooling of SEB is made in two steps. First step is from heating components (connected with HP evaporator) inside of SEB on the surface (connected with HP condenser) of SEB by HP (see Figure 3) and the second step is from this point on surface (connected with LHP evaporator) of SEB to construction of seat (connected with LHP condenser) by LHP (see Figure 2). Temperature of components in SEB is sensed on Printed Card Board (PCB). Temperature of seat construction is sensed on beam of seat and on LHP condenser. Measured values were sensed by thermocouples Type J.

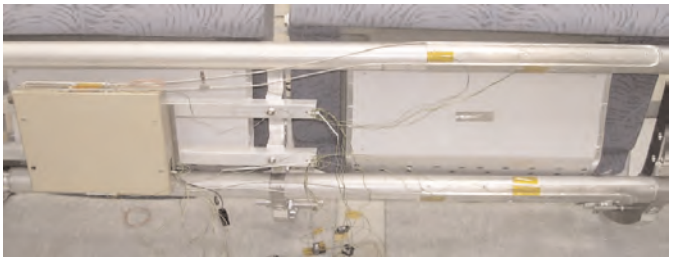

Fig. 2 — Installation of cooling system on AVIO seat

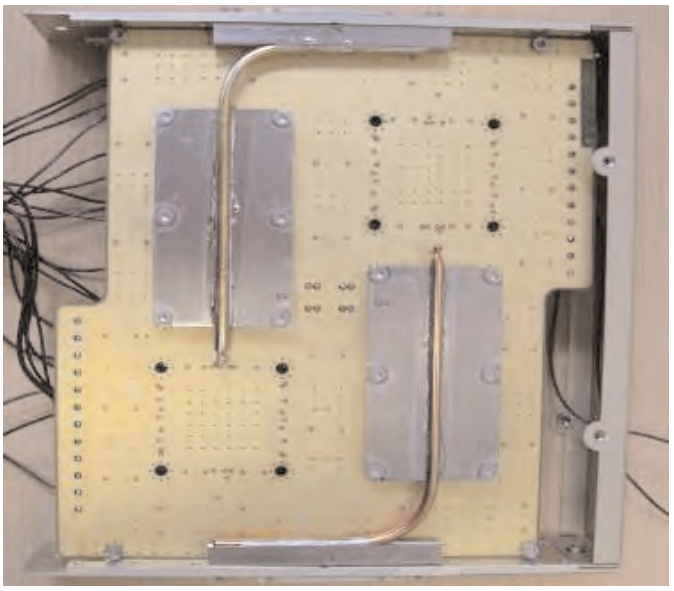

Fig. 3 — Installation of cooling system in SEB

4.1 Static ambient performance

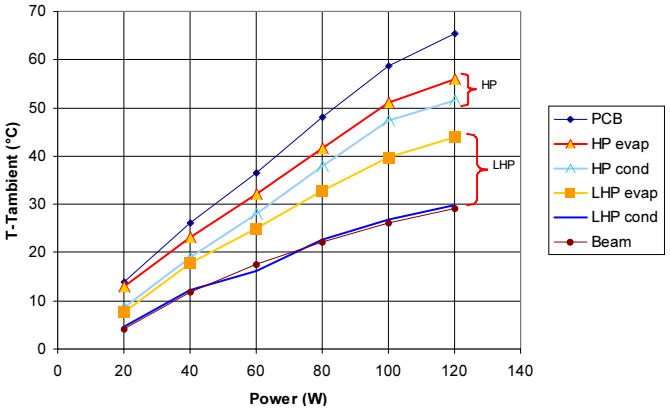

Fig. 4 — Avio seat with ITP Loop Heat Pipe

Temperature difference in the seat metal structure is about 30° C with 120W on the SEB and 17,5° C with 60W.
HP thermal gradient: 3° C, LHP thermal gradient: 14° C.

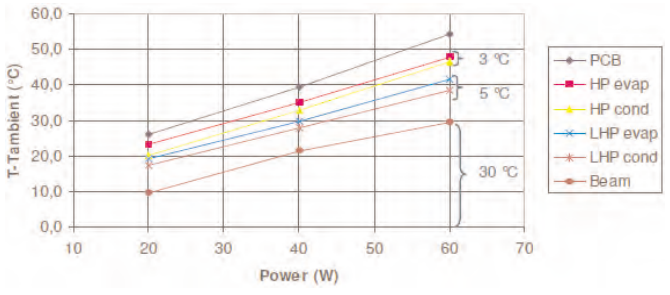

Fig. 5 — Recaro seat with EHP Loop Heat Pipe

Bad heat dissipation in the seat structure λxy = 50W/mK and λz = 1W/mK in carbon beam.

Strong gradient in the beam near the LHP condenser.

LHP efficiency is good: HP thermal gradient: 3° C, LHP thermal gradient 5° C with a tilt between evaporator and condensor of 500mm.

4.2 Variation of Ambient Temperatures 35° C, 45° C, 55° C

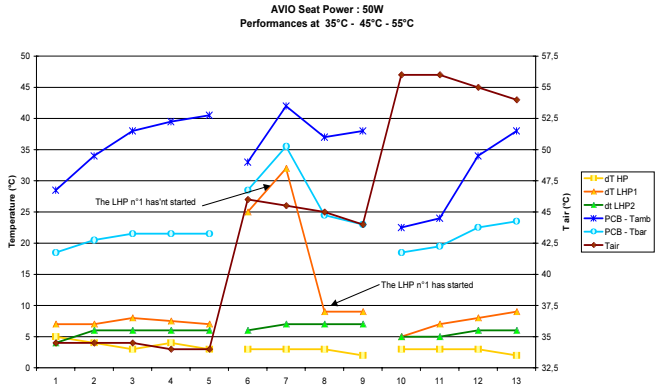

Fig. 6 — Avio with ITP Loop Heat Pipe performances

ΔT PCB stays at the same level under the different ambient temperatures.

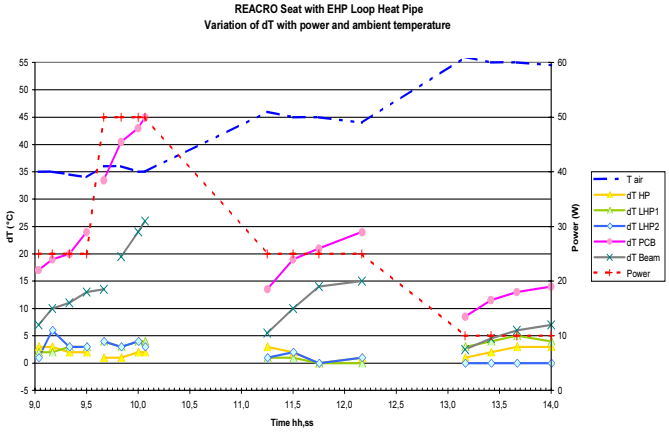

Fig. 7 — Recaro with EHP Loop Heat Pipe performances

For the same power 25W a difference of 10° C of ambient temperature do not impact the LHP.

4.3 Linear acceleration

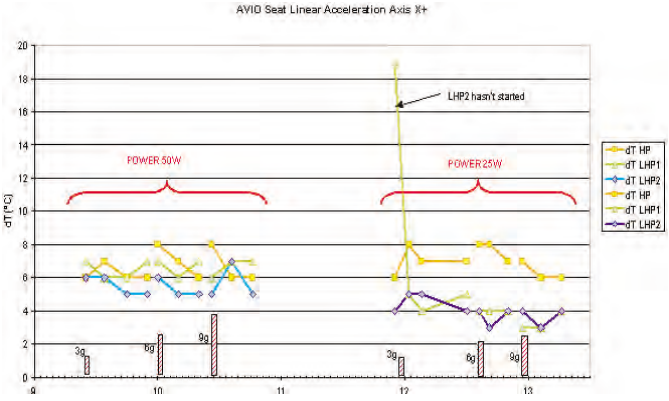

Fig. 8 — Avio Seat Linear acceleration axis X+

Except some start up behaviour at low power the loop heat pipes still correctly operate after three minutes acceleration up to 9g.

The thermal performance of HP and LHP are not affected by the acceleration in any directions.

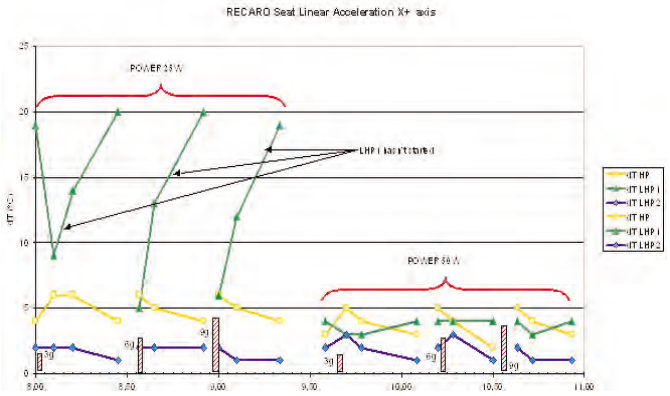

Fig. 9 — Recaro seat linear acceleration X+ axis

The acceleration does not affect the thermal behaviour of the HP and LHP systems.

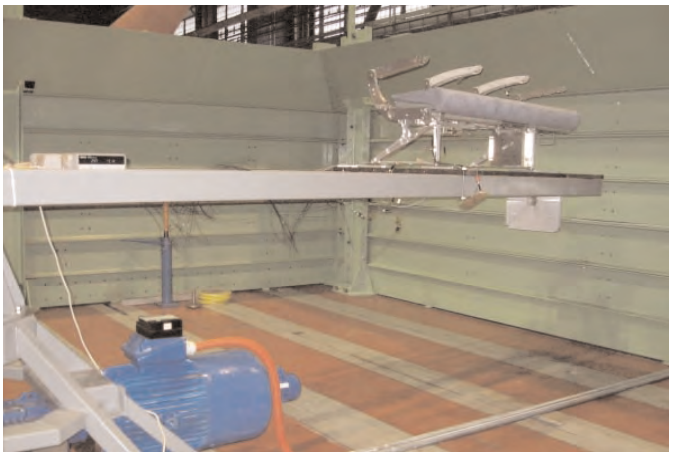

Fig. 10 — Avio Seat on centrifuge

4.4 Vibration

Measured values were similar to results in static ambient test.

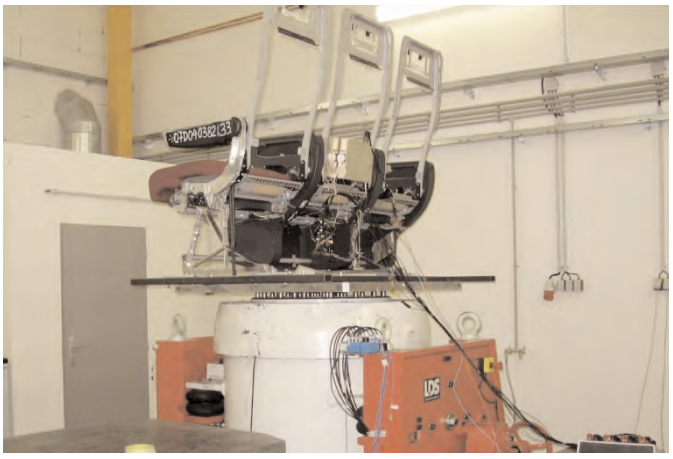

Fig. 11 — Recaro seat vibration test

5 Conclusions of the tests

The two seats have been submitted to the different aeronautic specifications without any damages or detrimental effects.

The two types of Loop Heat Pipes EHP and ITP have a good thermal behaviour.

Only start up problems under very low heat flux (the heat flux at the loop heat pipe evaporator) is not enough for the star-

ting of the system. The internal heat pipe and the loop heat pipes are not affected after three minutes acceleration up to 9g.

The Avio seat with ITP LHP gives better results than the Recaro seat equipped with EHP LHP. This results are due to the cooling capacity of the seat structure in graphite composite and not to LHP performance.

This cooling solution requires a seat with a mechanical structure having a good thermal conductivity.

References

[1] Launay S., Sartre V., Bonjour J.: *Effect of Fluid Thermophysical Properties on Loop Heat Pipe Operation*;. 14th Int. Heat Pipe Conf., Florianopolis (Brasil), April 2007

[2] Maydanik Y. F.: *Loop Heat Pipes*; Applied Thermal Engineering 25, 2005, pp. 635-657

[3] Riehl R.R., Siqueria T.: *Heat Transport Capability and Compensation Chamber Influence in Loop Heat Pipe Performance*; Applied Thermal Engineering 26, 2006, pp. 1158-1168

The Fast Transient Processes Simulation by Using IST Electro Hydraulic Test Control System

Simulace rychlých přechodových dějů elektrohydraulickým zkušebním systémem IST

Martin Oberthor, Jiří Nejedlo / VZLÚ, Plc., Prague

Impulsive loading is generally very dangerous; it can initiate sudden failure of material which would not happen during the static loading. A test facility has been built up for this reason at VZLU Strength of Structures Department. This test facility enables the fast transient process simulation. The article describes simulation of fast transient processes and construction impulsive loading by using IST Electro Hydraulic Test Control System. Success in solving this problem will improve VZLU testing potential.

Rázové působení síly je obecně velmi nebezpečné, neboť může iniciovat náhlou destrukci materiálu, ke které by při statickém zatížení nikdy nedošlo. Z tohoto důvodu bylo na divizi Pevnosti konstrukcí VZLÚ postaveno zkušební zařízení, které umožňuje simulovat rychlé přechodové děje. Tento článek se zabývá simulací rychlých přechodových dějů a impulsního zatěžování konstrukcí prostřednictvím elektrohydraulického zkušebního systému IST. Zvládnutí této problematiky umožní rozšířit zkušební potenciál VZLÚ.

Keywords: Impulsive loading, IST Electro Hydraulic Test Control System, MOOG servo valve, control loop, PID controller, transient characteristic, frequency response characteristic, crash test.

1 Introduction

Dynamic forces often occur under operation. Impulsive loading is generally very dangerous; it can initiate sudden failure of material which would not happen during the static loading. Sudden fracture caused by impulse force has minimum of deformation only (brittle failure) and there is no plastic deformation vestige. Simplified dynamic loading calculation based on the energy balance is illustrated on free fall of weight example (Fig. 1).

This simplified approach to energy balance is used for the impulse stress and deformation calculation — (affecting the modulus of elasticity E during the dynamic loading is left out, the possibility of loss of energy associated with system, etc.). The following equation is expressing energy balance between the bar store (deformation) energy and weight potential energy:

$$F_r = F_s \cdot \left(1 + \sqrt{1 + \frac{2 \cdot h}{\Delta l_s}}\right) \qquad (1)$$

Which means:

F_r - Dynamic effect of the force

F_s - Static force

h - Height of weight free fall

l_s - Rod deformation during the static loading

The bracket expresses impulse (dynamic) coefficient k_r. This coefficient defines how many times the static stress and deformation quantities are increased due to an impulsive loading.

$$k_r = 1 + \sqrt{1 + \frac{2 \cdot h}{\Delta l_s}}$$

Results from the equation: if $h = 0$ (drop from the height = 0, impulsive loading), the dynamic stress is double in comparison with the slow (static) loading. For more details see [1].

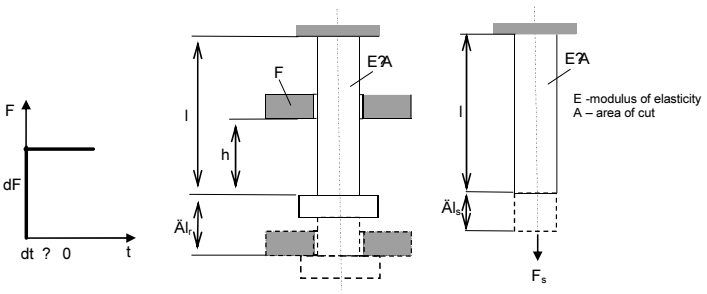

Fig. 1 — Example of weight free fall

Sudden fracture caused by the impulsive loading has only imperceptible deformation in its surroundings — it is a brittle fracture. Is it generally accepted that the deformational resistance increases with increasing of the deformational velocity. The limit of elasticity, yield strength and the material strength also increase with the speed of deformation velocity. Yield strength is close to the strength limit with increasing of the

deformational velocity. It follows that also plastic material can fail without previous plastic deformation in the case of fusion of these limits.

2 Testing equipment

Hydraulic circuit

Aim of the tests was verification of testing equipment behavior at fast transient process simulations. It was also possible to verify how the test specimen will be affected by the impulse loading.

The straight actuators are used generally for the fast transient processes simulation in the Strength of Structures Department. The actuator IST, type PG63P was found suitable for these tests. Maximum static force is 48,2 kN; maximum dynamic force 38,5 kN; maximum stroke 400 mm. The load cell SCHENCK, type PM63K, is mounted on the actuator. The actuator is equipped with LVDT (Linear Variable Differential Transformer).

The actuator is controlled by electro hydraulic converter — by *servo valve*. The different servo valves enable to achieve various characteristics of fast transient processes simulations.

The five servo valves have been tested. The actuator and whole hydraulic circuit was supplied by IST Schenck Hydraulic Power Supply, type PP165BA. Service pressure was 28 MPa, maximum supply flow rate was 160 l/min. Hydraulic Service Manifold PF 205 A2 was used for the hydraulic circuit control and protection. The following variants of servo valve connection have been tested for the fast transient characteristics evaluation:

Variant No. 1: The actuator was controlled by single MOOG servo valve with maximum flow rate 38 liters per minute (lpm).

Variant No. 2: The actuator was controlled by single MOOG servo valve with maximum flow rate 63 lpm. This servo valve is capable to increase the flow rate by 65 % comparing to Variant No. 1.

Variant No. 3: The actuator was controlled by single MOOG servo valve with maximum flow rate 93 lpm. This servo vale is capable to increase the flow rate by 144 % comparing to Variant No. 1. The highest flow rate and full opened servo valve channels can cause the supply pressure drop. For this reason one HYDAC SB330-2 accumulator was connected to the feed line and the same accumulator was also connected to return line (undesirable oscillations damping).

Variant No. 4: The actuator was controlled by two parallel servo valves with the different flow rates. These servo valves were placed on the same mounting base. The quicker servo valve with the maximum flow rate 38 lpm had opened the supply pressure to the actuator first, the slower servo valve with the maximum flow rate 63 lpm amplified the pressure supply consequently. This servo valves connection was recommended by MOOG company.

Variant No. 5: The actuator was controlled by two servo valves with the same flow rates 63 lpm. These servo valves were placed on the same mounting base again.

IST Electro Hydraulic Test Control Systems

IST (Instron Structural Testing) Labtronic 8800 Electro Hydraulic Test Control System was used for test specimen loading. The basic closed-loop with load control was used (Fig. 2). System A/D converter was 16 bit. The system sampling rate was 0,2 ms.

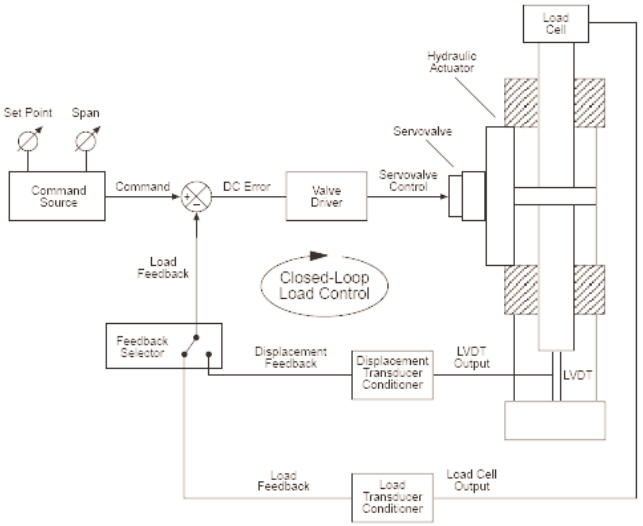

Fig. 2 — The basic IST control block diagram

The PID controller at **series connection** was used during the tests.

The equation of this controller at series connection follows (Fig. 3):

$$u = K * e + \frac{1}{T_I}\int (K * e)dt + T_D * d(K * e) + \frac{1}{T_I}\int (K * e)dt \quad (2)$$

the variables mean:

K - Proportional gain;
e - Control error;
T_D - Derivative constant;
T_I - Integration constant;
u - Actuating signal, here is a **servo valve control**.

The equation (2) after simplification:

$$u = K * (e + \frac{1}{T_I}\int edt + T_D \frac{de}{dt} + \frac{T_D}{T_I} * e) \quad (3)$$

Parameter ***K*** represents the gain of the proportional controller — ***P* gain** here. Mainly this value influences the whole control loop.

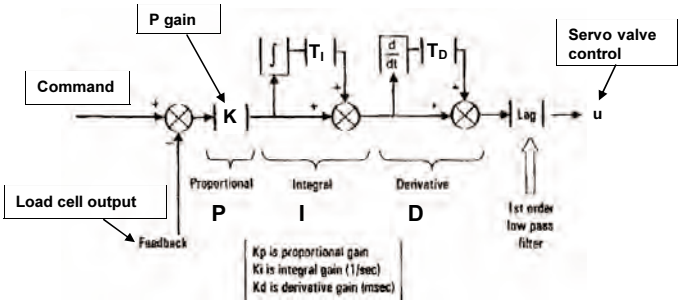

Fig. 3 — The control loop with PID controller (series connection)

Remark: This series control loop contains in addition term T_D/T_I in comparison with the standard (parallel) PID control loop.

3 Test specimen

The constructive part designed for automotive industry was used as a test specimen. This component was the cast made of the alloy AlSi9Cu3.

The test specimen was tested in two variants of its fixation to the rigid test rig:

- Assembly without original rubber silent block; the rubber

silent block was substituted by rigid dummy;
- Assembly with original rubber silent block, this variant represented the real fixation in the car.

The Fig. 4 shows one of the servo valves test arrangement mentioned above. This arrangement includes the valve variant No. 3 (servo valve 93 lpm and two accumulators HYDAC). The test specimen is fitted without original rubber silent block.

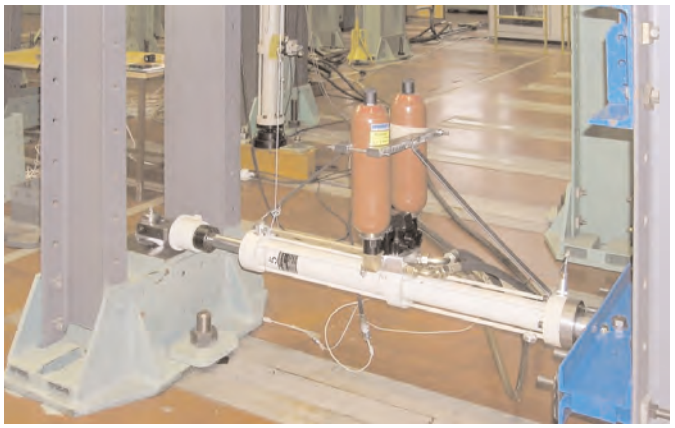

Fig. 4 — The test arrangement overview. Servo valve variant No. 3; Assembly without original rubber silent block

4 Tests

Transient characteristics

There are a lot of methods for the quality control process evaluation, but no criterion is unique. The dynamic properties of the system are analyzed most often by the system transient characteristic measuring. We can say that it was possible to find the optimal PID control setting (mainly *P* gain) for the force step changes not to be accompanied by greater test specimen deformation (it means greater actuator piston displacement). The servo valve characteristics have been dominant mainly in the case of piston displacement step changes (displacement control, crash tests etc., see below). The transient load characteristic examples are presented for the chosen servo valve variants here. The courses of transient characteristic as a response to command step change 2 kN - 5 kN for servo valve variant No. 3 (for various proportional gains of *P* gain) are shown in the Fig. 5. The test specimen was fitted on the test rig without original rubber silent block.

Some control characteristics were also monitored during the system transient characteristic tests. The following variables were measured: Command, Load (feedback) and Servovalve control (controller output). The curves of variables measured

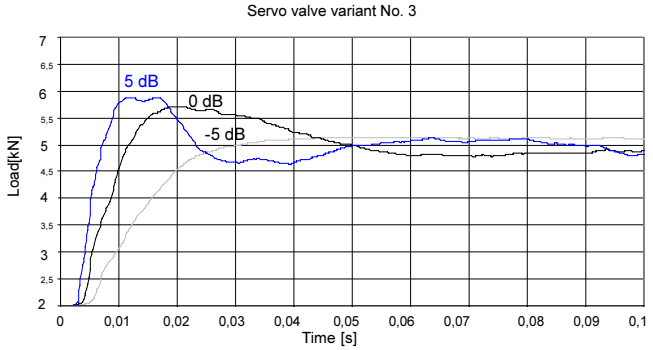

Fig. 5 — The curves of transient characteristic for various proportional gains; response to command step change 2 kN - 5 kN; assembly without original rubber silent block

during the tests (from the moment of the test trigger) are shown in Figs. 6 and 7. These curves cannot be shown in more detail because of sampling rate capabilities.

The servovalve control signal was appreciably affected by controller derivative unit at the beginning of the test (Fig. 6). When the command was going to be constant, the derivate unit decreased its influence on control loop. Anyway this servovalve control peak could by no means affect the feedback because of the entire control system time constant.

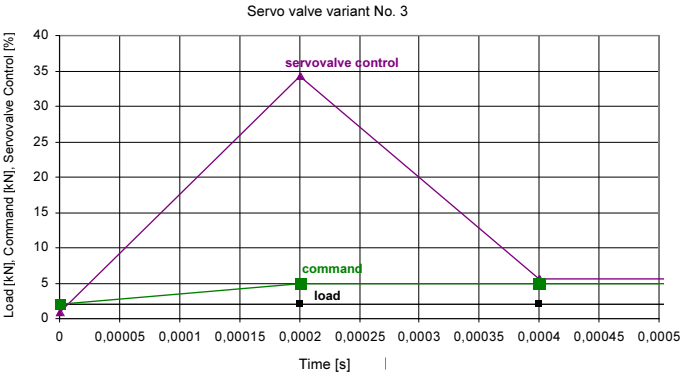

Fig. 6 — The transient characteristic measurement - the curves of control variables (moment of the test trigger), *P* gain = 0 dB

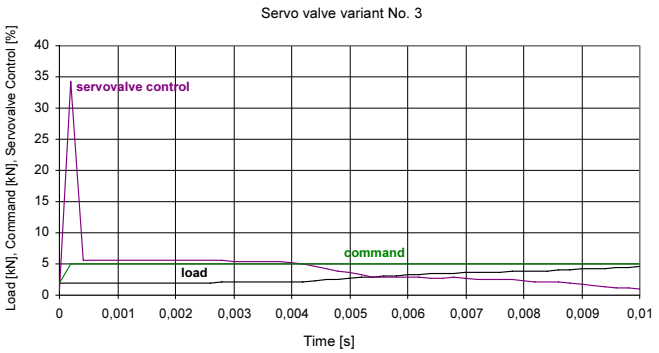

Fig. 7 — The transient characteristic measurement - the curves of control variables (longer time period), *P* gain = 0 dB

Magnitude of the servovalve control peak depended on the *P* gain setting (Fig. 8).

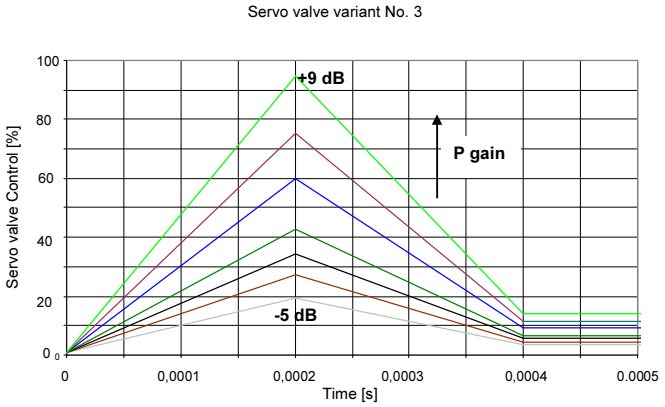

Fig. 8 — The transient characteristic measurement - the curves of servovalve control depending on the proportional gain setting

The curves of transient characteristic as a response to command step change 2 kN - 5 kN for servo valve variant No. 3 (for various proportional gains of PID controller) are shown in the Fig. 9. The test specimen was fitted on the test rig with original rubber silent block.

The curves of variables measured during the tests are shown in the Fig. 10. The servovalve control signal is again signifi-

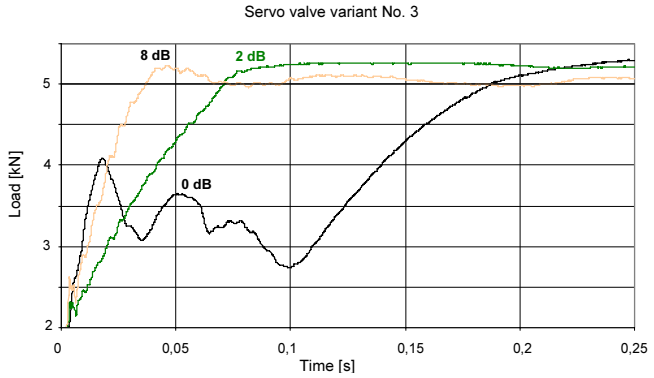

Fig. 9 — The curves of transient characteristic for various proportional gains; response to command step change 2 kN - 5 kN; assembly with original rubber silent block

cantly affected by controller derivative unit at the beginning of the test. When the command was steady, the controller (mainly derivate unit again) reacted to a feedback small change (influence of the silent block rigidity).

As was said before, the flow rating for each servo valve variant has a significant influence on displacement step changes. The servo valve variant comparison is shown in the Fig. 11.

The fastest response had a servo valve variant No.3. The additional accumulator HYDAC SB330-2 connected to the feed line was able to prevent loss of hydraulic pressure in the hydraulic circuit.

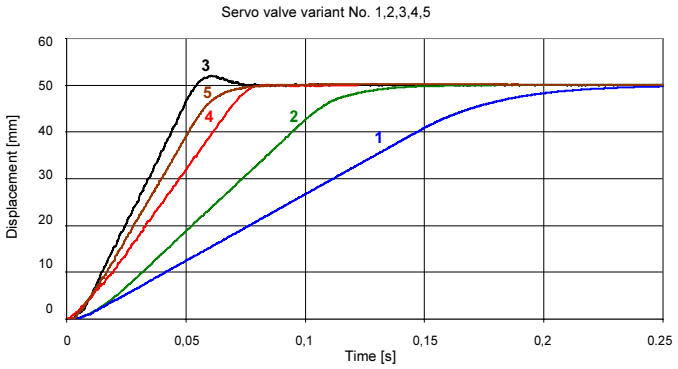

Fig. 11 — The transient characteristic measurement for all servo valve variants; response to command step change 0 mm - 50 mm

Frequency response characteristic

The frequency response characteristics are used for the more detailed system analysis (e.g. signal attenuation, stability, self-oscillations etc.). This method is less sensitive to disturbances by comparison with measurement of transient characteristics.

Frequency response characteristics were carried out (up to frequency $f = 50$ Hz) for all servo valve variants. When the *P*-gain setting was too high (different for each servo valve variant), the control overshoot (proportionate amplitude >1) happened for assembly without rubber silent block very often (Fig. 12).

The example of frequency response characteristic is shown in Fig. 13. The test was carried out for loading by harmonic curve, the loading mean value was 2 kN, the amplitude was 1 kN, P gain = 9 dB. The test specimen was fitted without rubber silent block.

The frequency response characteristic for test specimen fitted with original rubber silent block is shown in Fig. 14. The test was carried out for loading by harmonic curve, the loading mean value was 2 kN, the amplitude was 1 kN, *P* gain = 8 dB. The test specimen was fitted with rubber silent block.

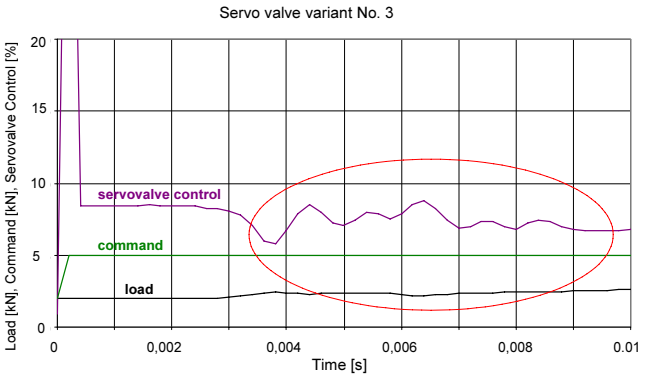

Fig. 10 — The transient characteristic measurement - the curves of control variables; assembly with original rubber silent block

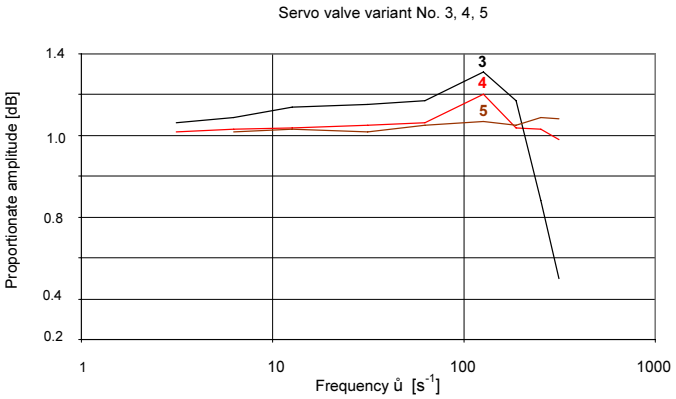

Fig. 12 — The amplitude responses for loading by harmonic curve; mean value 2 kN, amplitude 1kN, *P* gain = 2 dB; test specimen was fitted without rubber silent block

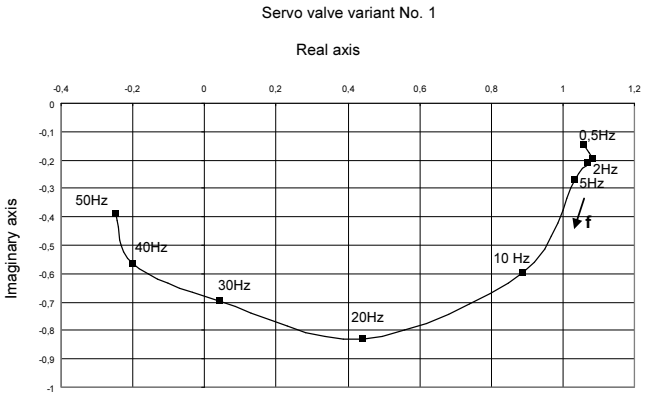

Fig. 13 — The frequency response characteristic for loading by harmonic curve; mean value 2 kN, amplitude 1 kN, *P* gain = 9 dB; test specimen was fitted without rubber silent block

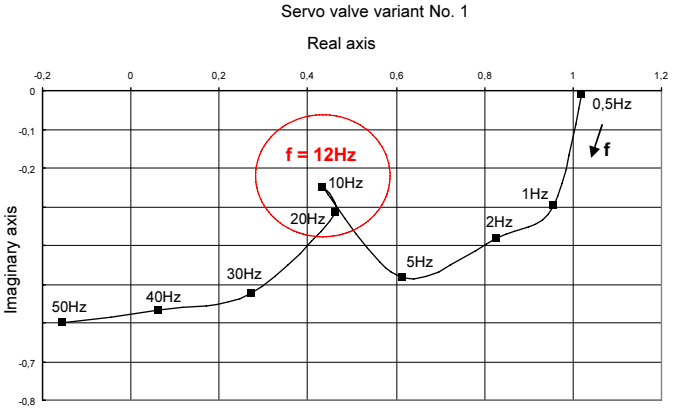

Fig. 14 — The frequency response characteristic for loading by harmonic curve; mean value 2 kN, amplitude 1kN, *P* gain = 8 dB; test specimen was fitted with rubber silent block

Apparent attenuation at frequency approximately 12 Hz can be seen in the following figure. It was found, that this frequency corresponds to rubber silent block (including of test preparation) natural frequency, see frequency spectrum response in Fig. 15.

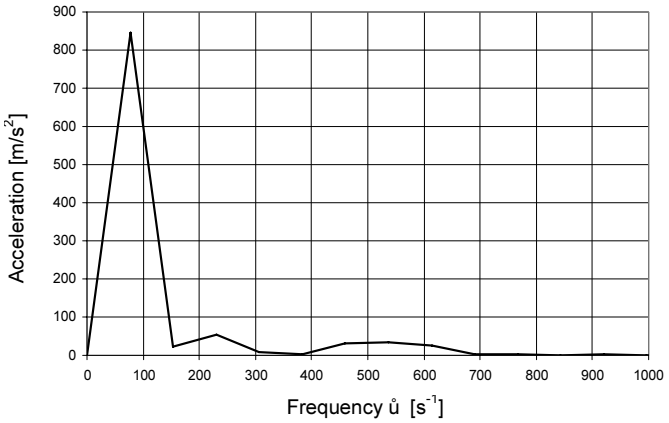

Fig. 15 — The frequency spectrum response of the original rubber silent block including of test preparation

Crash tests

Practical verification of impulsive loading was carried out by so-called crash tests. The aims of such a test generally are:

- ❑ evaluation of the crash behavior of the component with a given geometry,
- ❑ validation of the crash behavior of the component with a given geometry,
- ❑ test/simulation correlation

Loading conditions were:

- Preload the tested object on the level of 500 N.
- The force has to reach dynamic load level of 30 kN in the course of 10 ms.
- The tested object must be loaded until the rupture.

The flow rating of each servo valve variant affected the results because of significance piston displacements at crash tests (as well as the piston displacement step changes, see above). The crash test curves for each servo valve variant are shown in the following figures.

In the Fig. 16, time = 0 sec defines the moment changes in the command signal. The knowledge of this course is important when we need to verify the whole control loop response on command signal. Dead time T_d = 0,002 sec is evident here. T_d is nearly the same for all servo valve variants. The load rice time up to the moment of specimen failure is the most important for chosen the right servo valve variant. The fastest variants were variants No. 3 and No. 5 (Fig. 17).

Remark: There is no possibility to accurately determine the impulsive energy, because of the absorption immeasurable part of energy by the stand, fixture etc. The energy was determined by means of load force and piston distance measuring.

The curves of variables measured during the crash tests (Fig. 16) are shown in the Fig. 18. The servo valve was fully opened until the test specimen rupture. The position of piston rod stopped subsequently the test.

Following figure shows the crash test curves for each servo valve variant. The test specimen was fitted with rubber silent block.

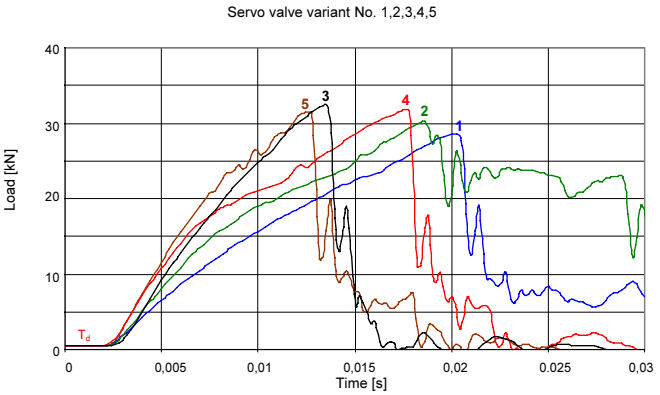

Fig. 16 — The crash tests for all servo valve variants; time = 0 s defines changes in the command signals; assembly without original rubber silent block

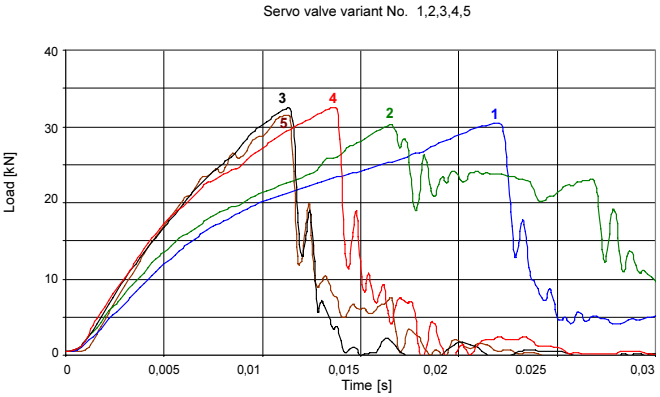

Fig. 17 — The crash tests for all servo valve variants; time = 0 s defines the moment changes in the load cell outputs; assembly without original rubber silent block

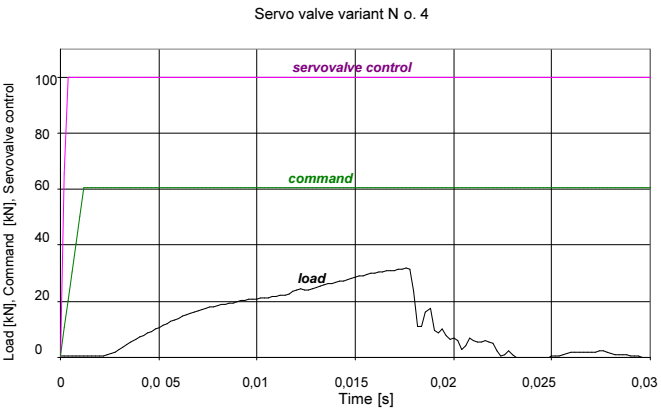

Fig. 18 — The crash test measurement - the curves of control variables; assembly without original rubber silent block

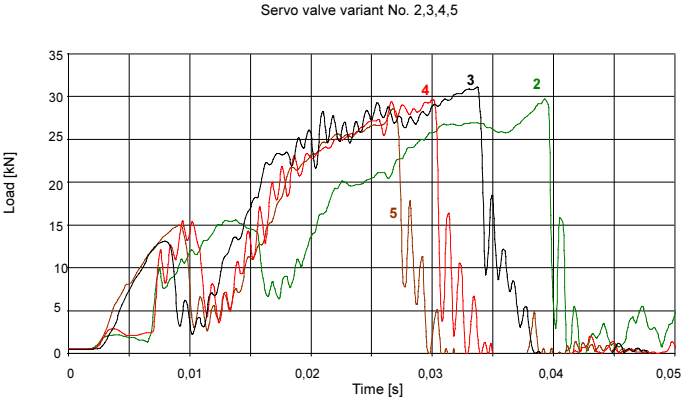

Fig. 19 — The crash tests for all servo valve variants; time = 0 s defines the command signal change; assembly with original rubber silent block

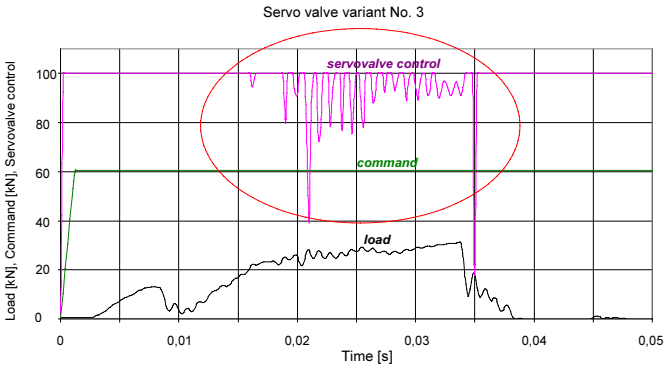

Fig. 20 — The crash test measurement - the curves of control variables; assembly with original rubber silent block

The curves of variables measured during the crash tests (Fig. 19), are shown in the Fig. 20. The servo valve was fully opened first. The signal from load cell was vibrating during some period of the silent block deformation (for the reason of rubber silent block rigidity). This caused, that derivate unit started to vibrate too and affected the servovalve control. After the rupture the piston position stopped the test subsequently.

Static test

The static tests of the test specimen till the rupture were carried out to assess of the dynamic force effect. The tests were performed for servovalve variant No. 3, *P* gain = 9 dB and for three load speeds: 1 kN/s; 0,5 kN/s; 0,1 kN/s.

The rupture happened practically on the same load level, within the range: 28,5 kN - 29 kN (Fig. 21).

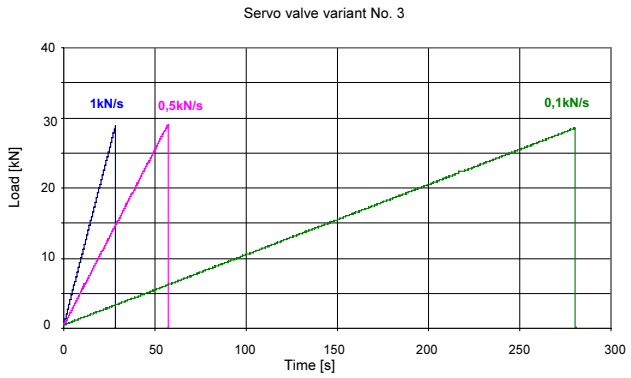

Fig. 21 — The static tests for three load speeds; assembly without original rubber silent block

The increase in test specimen strength is approximately **10%** to **15%** in comparison with the crash tests (for assembly without original rubber silent block). The fracture surfaces from the static tests are almost identical with the test specimens of the crash tests.

Reviewing the results following should be kept in mind:

- The specimen is alloy casting AlSi9Cu3;
- Fast process we used (approximately 10 ms to fracture) doesn't have to fulfill the conditions of equation (1) $dt \rightarrow 0$ s mentioned in introduction

Conclusion

Impulsive loading is generally very dangerous; it can initiate sudden failure of material which would not happen during the static loading.

The test facility has been built up for this reason at the VZLU Strength of Structures Department. This test facility enables the fast transient process simulation. The actuator IST type PG 63 was chosen as a suitable option for these tests. The five variants of MOOG servo valve connection have been verified here in connection with this actuator, including the additional accumulators HYDAC.

Aim of the tests was verification of testing equipment behavior at fast transient process simulations. It was also possible to verify how the test specimen will be affected by the impulse loading. The tests were carried out on real cast of constructive part and were fitted with the original rubber silent block as well as with the rigid dummy.

The article contains examples of transient characteristics, frequency response characteristics, crash tests and the comparison with the static tests.

Acknowledgements

This research was supported by the grant MSM0001066903 of the MŠMT (Ministry of Education, Youth and Sport of the Czech Republic).

Reference:

[1] Textbook of Czech Technical University of Prague, Faculty of Mechanical Engineering: *Strength and Elasticity I*, Prague 1997

Intentionally left void.

Influence of Silumine Castings Microstructure on Component Failure Resistance

Vliv mikrostruktury odlitků vyrobených ze siluminu na odolnost součásti proti mechanickému porušení

Miroslava Machková, Roman Růžek / VZLÚ, Plc., Prague;
Drahomíra Janová / Institute of Material Science and Engineering, Brno University of Technology, Brno

The paper is concerned with the assessment of relationship between the casting structure of AlSi9Cu3 alloy and its failure resistance. Following the impact and fatigue tests a metallographic analysis of casting microstructure was performed. The objective of this work was to define causes of reduced resistance to mechanical damage that had occurred for several types of castings. Macro- and micro-porosity, metallographic structure and presence and distribution of particular phases were investigated. Micro-analysis of phase composition was carried out. All of samples showed pores and cavities. The distribution of these flaws was so much different, even in near sections of the same casting, that no significant correlation has been found. Based on the metallographic analysis, it is possible to assume that the structure of mechanically more resistant castings is more coarsely grained with larger alpha-phase aluminum surfaces and features ferrum only in the form of tiny angulate particles always accompanied by manganese. The structure of less resistant castings contains larger stellar-shaped particles of $Al_{15}(MnFe)_3Si_2$ intermetallic phase, and more importantly, it has sharp, hard and brittle needles of Al5FeSi intermetalic phase, which dramatically deteriorate mechanical properties due to their notch effect. The creation of these particles is connected with solidification conditions.

V příspěvku je diskutována souvislost mezi strukturou odlitků ze slitiny AlSi9Cu3 a jejich odolností proti mechanickému porušení. V návaznosti na rázové a únavové zkoušky odlitků ze slitiny AlSi9Cu3 realizované v různých stádiích vývoje nové součásti, byla provedena metalografická analýza mikrostruktury vzorků těchto odlitků. Cílem analýzy bylo najít příčiny snížení odolnosti proti rázovému poškození u některých typů odlitků. Byla sledována makro i mikro pórovitost na řezech a výbrusech, metalografické struktury, přítomnost a rozložení jednotlivých fází, byla provedena mikroanalýza jejich složení. Všechny vzorky vykazovaly póry a dutiny. Rozložení těchto poruch bylo natolik rozdílné i v jednotlivých blízkých řezech a výbrusech ze stejného odlitku, že se nepodařilo najít významnou korelaci. Na základě provedené metalografické analýzy lze konstatovat, že struktura mechanicky odolnějších odlitků je hrubší s většími plochami α-fáze hliníku, dále se ve struktuře odolnějších odlitků vyskytuje železo pouze ve formě drobnějších hranatých až hvězdicovitých částic vždy společně s manganem. Ve struktuře méně odolných odlitků lze pozorovat větší hvězdicové částice intermetalické fáze $Al_{15}(MnFe)_3Si_2$, ale především se zde vyskytují ostré, tvrdé a křehké jehlice železité fáze Al_5FeSi, které svým vrubovým účinkem výrazně mechanické vlastnosti součásti zhoršují. Vznik těchto částic souvisí s podmínkami při tuhnutí taveniny, především s rychlostí ochlazování.

Keywords: silumine, casting, impacte resistance, fatigue, porosity, intermetallic phases.

1 Introduction

The impact and fatigue tests were carried out for several casting versions during the development of a highly mechanically loaded casting part. In some period of the component development, after the reinforcement of the critical areas worse mechanical properties of the structure turn up. Based on these results it was apparent that mechanical properties of the component are significantly influenced by manufacturing technology, firstly by solidification rate in the critical areas, gas trunk during cooling and pressure conditions during casting. These factors influence the macrostructure and microstructure of the material with strong impact on the mechanical and fatigue behaviour of the product. Therefore the objective of the paper is to find the relationship between the microstructure and the failure resistance of the casting.

2 Material and specimen description

Six pieces of the casting were used for the metallographic analysis. Individual specimens were marked by a number with the following meaning:

type-1 corresponds to the first version of the component,

type-2 corresponds to the version with geometry extension of critical cross sections (and at the same time with the worst failure resistance) both with original technological process of the casting,

type-3 represents the version with cross sections modification (a little bit smaller cross section compared to the second version) and with three different casting conditions (a, b, c).

type-4 represents the final version of the component with the best mechanical properties.

Castings were made from hypoeutectic unmodified silumine EN AC-46000 (EN AC-AlSi9Cu3(Fe), ČSN 42 4339), that approximately corresponds to US material AA 380.0. The chemical composition of the alloy is illustrated in **Table 1**. This material is often used mainly in the automotive industry. The mechanical and fatigue properties of products made from this material depends not only on average chemical composition but also on macro and micro structure. The relevant para-

Tab. 1. Typical chemical composition of Al Si9Cu3 alloy [wt %]

Alloy	Si	Fe	Cu	Mn	Mg	Ni	Zn	Pb	Sn	Ti	Others		Al
EN AC-46000	8.0-11.0	1.3	2.0-4.0	0.55	0.05-0.55	0.15	0.55	1.2	0.35	0.25	0.05	0.25	Remainder

meters influencing the properties of the structure are:

a) Porosity - cavities (bubbles, microshrinkage, gas pores).
b) Type, size, number and shape of intermetallic phases.
c) Structural parameters (dendrite cells size, morphology of eutectic silicon, morphology of intermetallic phases, etc.).

The needle of eutectic silicon with typical branching, particles with iron and manganese in the shape of star and "Chinese script", particles with cuprum and single sharp needles of iron occur in alloy AlSi9Cu3, as is described and studied in literature [1], [2], [3], [4], [5], and [6].

3 Experiment

The samples were cut out by IsoCut4000 saw and prepared by standard metallographic procedures (grinded, polished with diamond suspensions and some of them etched by Dix-Keller or 0.5%HF). Subsequently the microstructural details were analysed using optical microscopy (Olympus GX51, SZ40) with different magnifications up to 1000x. Also, Nomarski DIC illumination technique was used. All samples were analysed with respect to the documentation of porosity.

One sample from each of 1, 2 and 4 specimens were prepared at the Brno University of Technology.

The chemical composition of the intermetallic phases was determined by scanning electron microscopy equipped with EDAX analyser. The microanalysis of two specimens was carried out at the Brno University of Technology. Based on this analysis, the shape of different particles was identified. The content of intermetallic particles for samples of type 1 (first version), 2 (the worst mechanical behaviour) and 4 (final version with the best mechanical properties) was determined.

4 Results and discussion

4.1 Porosity

Porosity was documented on all cutting surfaces of specimens. Fig. 1 illustrates the typical macrographs corresponding to a specimen of type 1 , a specimen of type 2 (the worst mechanical behaviour) and specimen of type 4 (the best failure resistance). Fig. 2 shows the largest and typical cavities on micrographs.

The cavity and the pores were detected in all specimens. The considerable inhomogeneity distribution of bubbles, shrinkages and pores was documented in the different sections of castings. Even if several cutting surfaces were cut out from the same casting very close to each other (distance between each of them was from 4 to 8 mm), the porosity is very different. The maximum size of a cavity is about 5mm (see Fig. 1 — middle left). Such a big and deep bubble was found in one cutting surface of specimen of type 2 only. In the other cuts of this specimen the cavities were not bigger then in the other castings. The next highest sum of cavity lengths (see Fig. 2 — bottom) was found in one of metallographic samples of specimen type 4 (the best failure resistance). This cavity seems to be more like as shrinkage and it is very shallow. Combination of smaller and shallow bubbles and shrinkages or tiny pores was detected only. This is a reason why we were not successful in finding any significant relation between the biggest cavity shape and the failure resistance. We can consider the big and deep bubbles are dangerous from the point of view of failure resistance.

4.2 Material microstructure

Microstructures of the castings of types 1, 2 and 4 which were analyzed in a greater detail by optical methods were found not to be much different. The material with the best mechanical properties (specimen type 4) has a little coarser grained structure in general, with larger areas of dendrite alpha phase of aluminium. In this structure, there are no big star shaped particles but edge shaped and smaller ones only. Fig. 3 shows the microstructure comparison of castings of types 1 and 4.

4.3 Material microanalysis

Microanalysis was performed on the metallographic samples of 1- and 4- type castings. The micrographs of structure acquired by electron microscope with analyzed points marked by members are in Figs. 4 and 5.

Sample made from the specimen 1 (Fig. 4): In the big star shaped particle (spot 1), presence of iron, manganese and smaller amount of chrome was detected. It is possible to consider these particles as the brittle and hard intermetallic "sludge phases" $Al_{15}(MnFe)_3Si_2$ as can be found in the literature [6].

Iron and manganese presence was detected also in the tiny edge shaped particle spot 6 and in the particle marked 7.

The particle 3 and white margins (spot 2) around particle 1 and part of the needle 4 show high percentage of copper with Mg and Ni traces. Similar it is in spot 8.

The needle 5 contains Fe with very low percentage of Mn, which corresponds with very hard and brittle phase Al_5FeSi. Even its shape acts in a very negative way.

A very similar composition was determined in spot 9.

The tiny bright point 10 is Pb-rich particle.

The hardly detectable needle 11 is Si-rich. This is a needle of eutectic silicon.

A sample made from the specimen 4 (see Fig. 5): Microanalysis shows that angulate, approximately hexagonally shaped particles contain Al, Si, Fe, Mn and Cr.

In the needles (spot 3) and neighbouring areas (spot 2) there is a high content of Si.

4.4 Intermetallic phase analysis

Comparison of intermetallic phase occurrences was performed based on of former analyses of micrographs with 1000x magnification. Fig. 6 and Fig. 8 document the presence of single particles, which are in the microstructure. In these figures, which were acquired using different techniques for scratch pattern, we can find particles containing Fe, or Fe and Mn as plastically emerging differently from Fig. 7 where single particles are detectable, but without the 3D topography. Cu features by significant perforation, eutectic Si differs by colour only.

In the individual pictures there are marked:

Particles A - intermetallic phase $Al_{15}(MnFe)_3Si_2$.
Needles and facets B - eutectic silicon.
Particles C - Cu presence.
Needles D - Fe needle of phase Al_5FeSi.

Comparisons of presence and morphology of phases in the samples made from casting 1, 2 and 4 lead to the following conclusions:

In the more failure-resistant structures, there are only smaller edge shaped particles containing iron and manganese. No iron-rich needles of phase Al_5FeSi are present in these structures.

5 Conclusions

Microstructure of higher failure-resistant castings is a little more coarsely grained with larger areas of Al α-phase. In castings like these, iron is present in smaller particles only and always together with manganese. No sharp, hard and brittle needles of ferrous phase Al_5FeSi occur. These particles would have a negative notch effect which significantly degrades the mechanical properties of material. Occurrence of these particles is probably the main reason of decreasing the failure resistance of castings. Other cause of mechanical properties degradation can be the presence of cavities. The big deep bubbles seem to be a peril for material behaviour; shallow shrinkages have probably no influence on the failure resistance.

Acknowledgement

This research was supported by the grant MSM0001066903 of the MŠMT (Czech Ministry of Education, Youth and Sports).

References:

[1] Michna Š. a kol.: *Encyklopedie hliníku*; Adin Prešov, (2005)

[2] Panušková M., Tillová E., Činčala M.: *Vplyv rozpúšťacieho žíhania na mechanické vlastnosti zliatiny AlSi9Cu3*; ALUMINIUM 2007, Transaction of the Universities of Košice 2007, pp. 160-165

[3] Tillová E., Chalupová M.: *Štúdium morfologie eutektického kremíka, v zliatinách Al-Si*; ALUMINIUM 2007, Transaction of the Universities of Košice, 2007 , pp. 17-23

[4] Roučka J., Veverka A., Diviš V., Ňuksa P.: *Effect of Gassing and Solidification Rate on Structure, Porosity and Mechanical Properties of AlSi9Cu3 Alloy Casting*; ALUMINIUM 2007, Transaction of the Universities of Košice, 2007, pp. 90-97

[5] Tillová E., Panáčková M., Chalupová M.: *Metallographic investigation of Al-Si-Cu alloys*; METALLOGRAPHY 2007, Acta Metallurgica Slovaca, 13, 1/2007, pp. 640-643

[6] Taylor J A.,: *The Effect of Iron in Al-Si Casting Alloys*; CAST, The University of Queensland, Brisbane, Australia

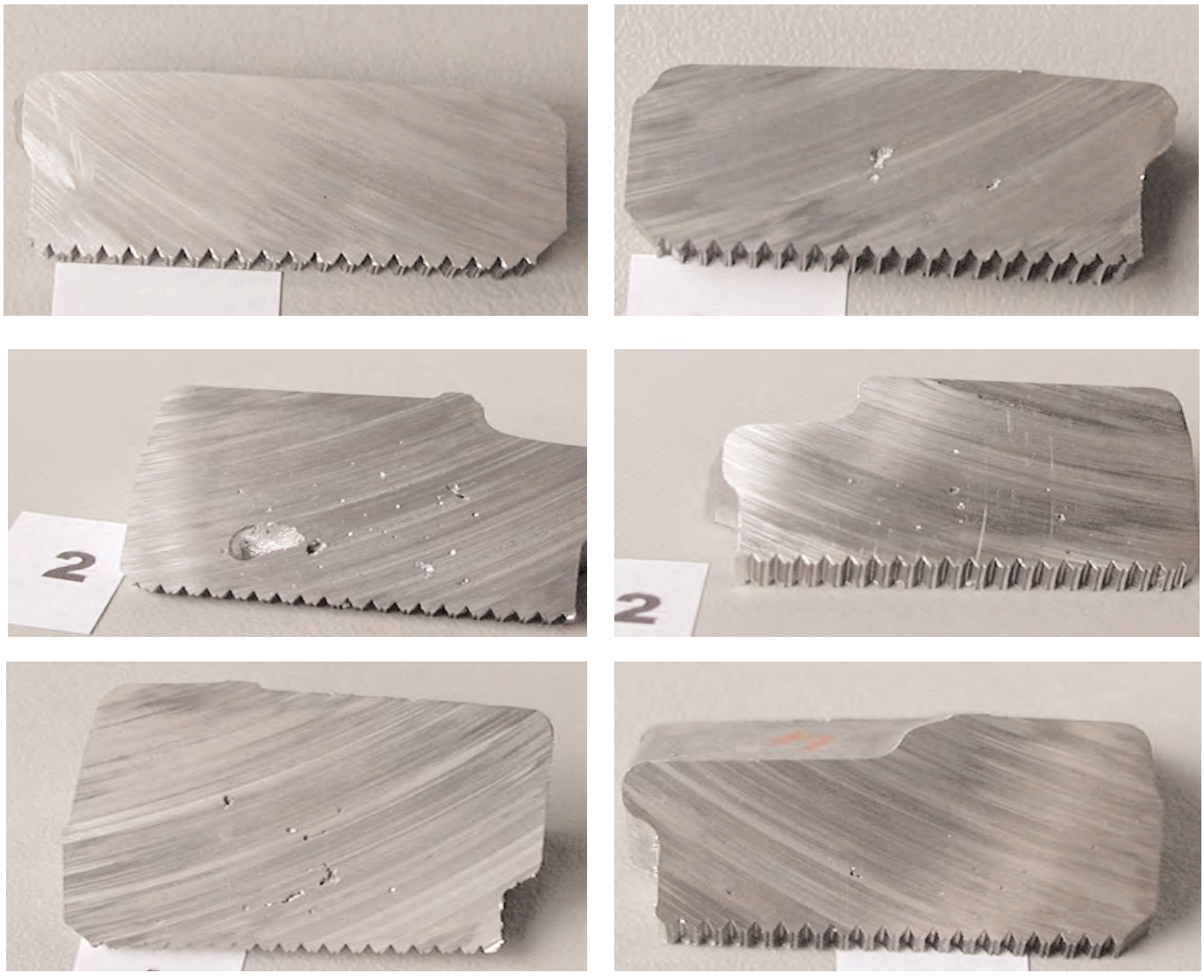

Fig. 1 — Macrographs of a specimen of type 1 (top), of type 2 (middle) with 5 mm cavity, and of a specimen of type 4 (bottom). The length of the scroll is 30mm for all specimens

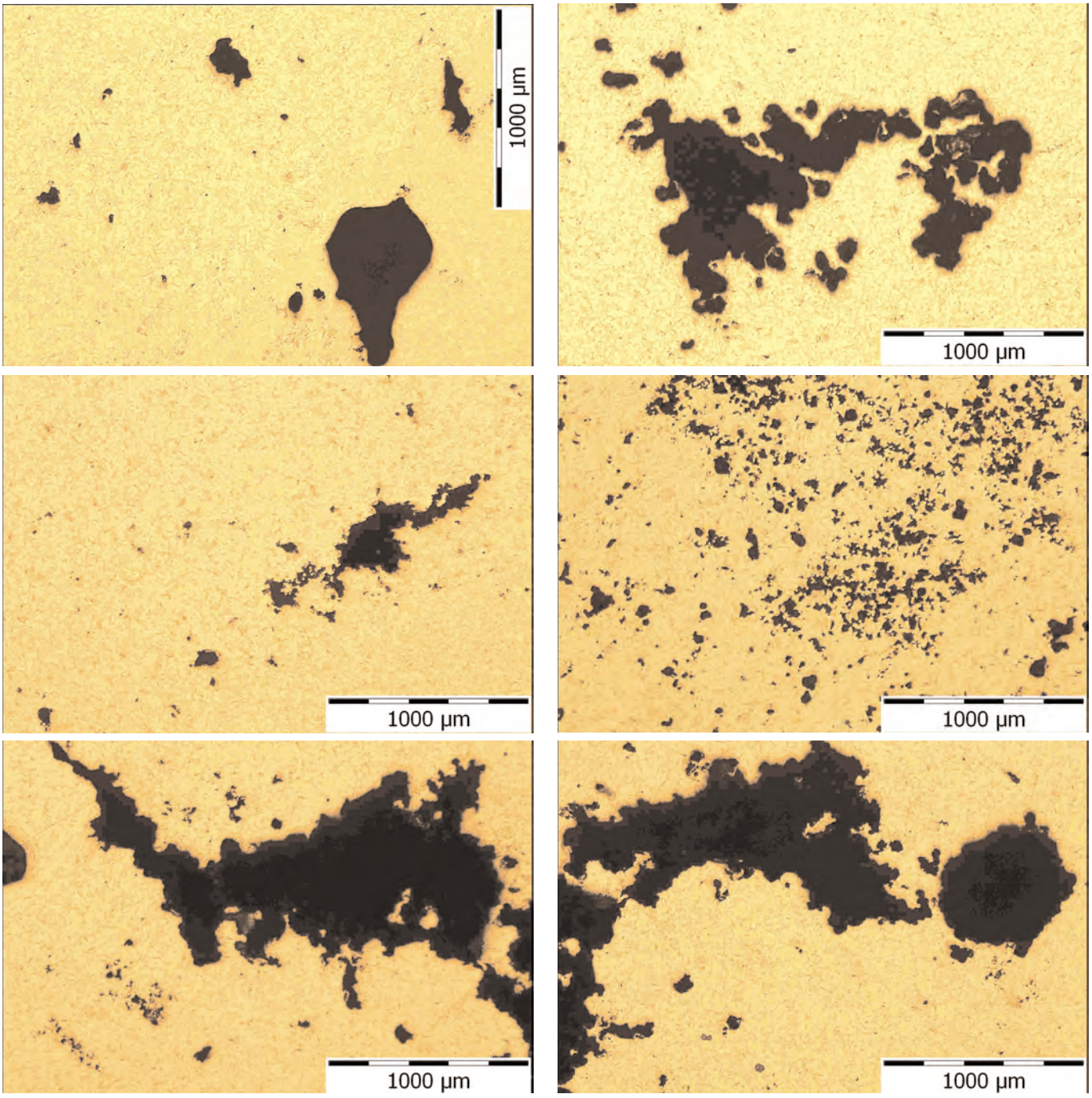

Fig. 2 — Micrographs of typical cavities corresponding to metallographic sample of specimen of type 1 and 2 (top), specimens of type 3c, 3a - small pores and cavities (middle), specimen of type 4 - with shallow cavity and its revolved part (total length of these cavities is 5 mm) (without etching)

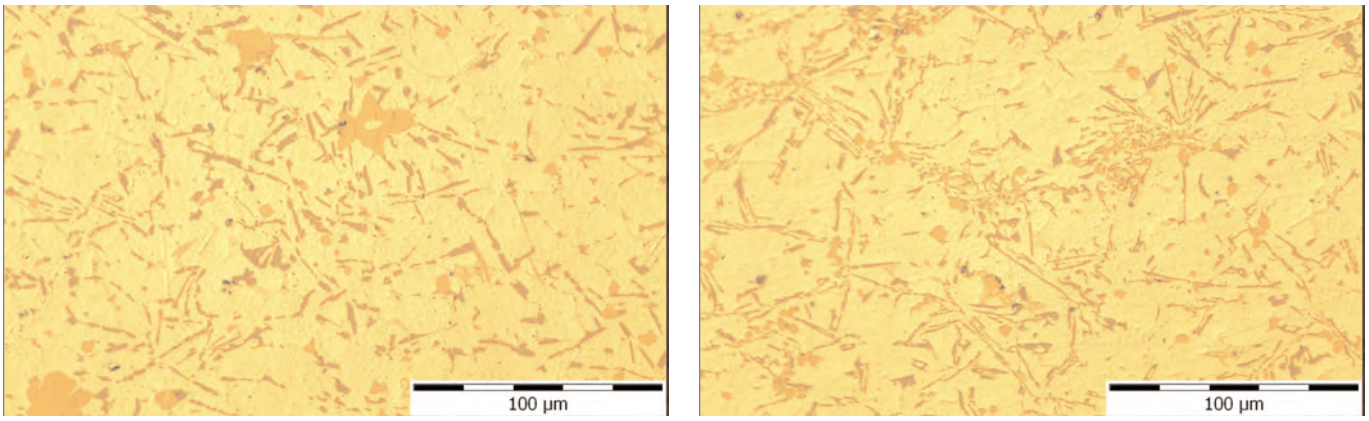

Fig. 3 — Microstructure comparison of castings of types1 and 4. Structures of casting 1 with a big star shaped particles (left), structures of casting 4 with tiny particles (right).(Nomarski DIC illumination)

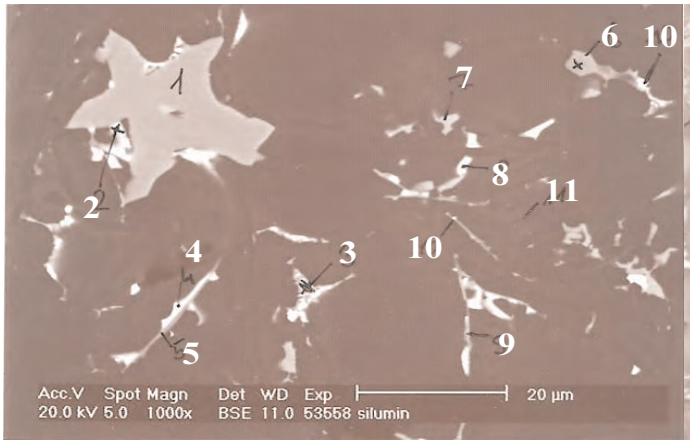

Fig. 4 — Micrograph of casting 1 structure

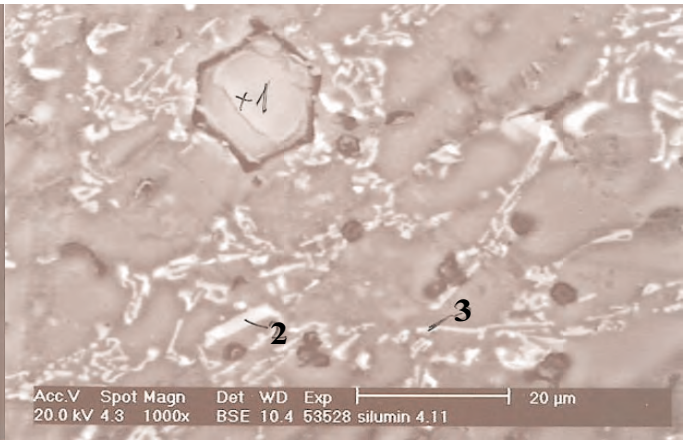

Fig. 5 — Micrograph of casting 4 structure

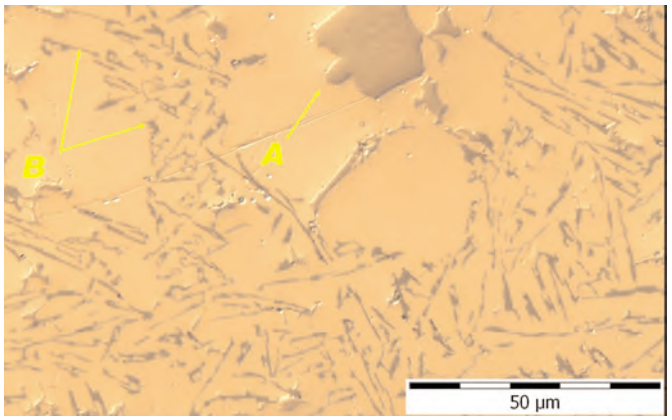

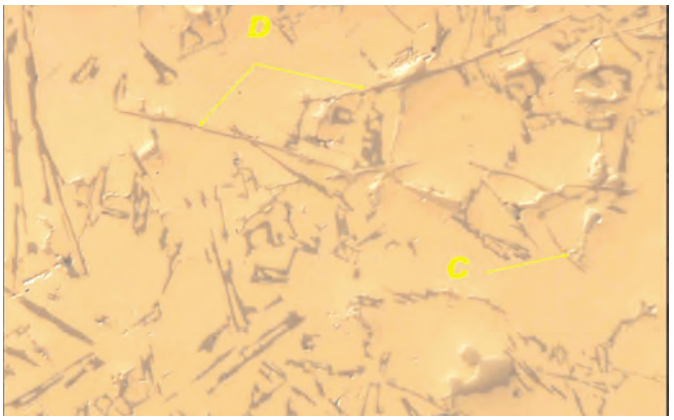

Fig. 6 — Image of phases in the metallographic sample of specimen 1
(Magnification 1000x, Nomarski DIC illumination)

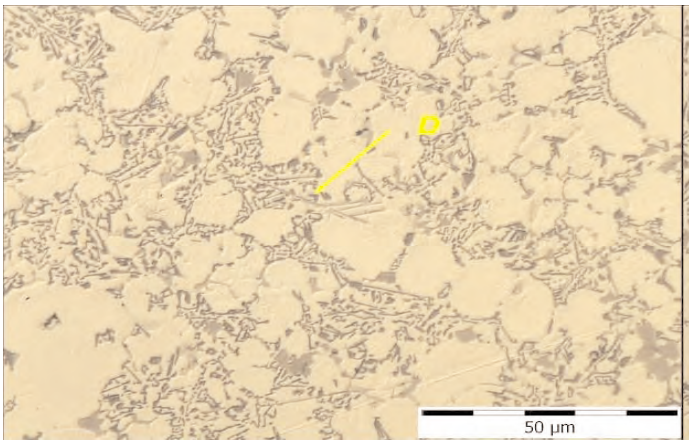

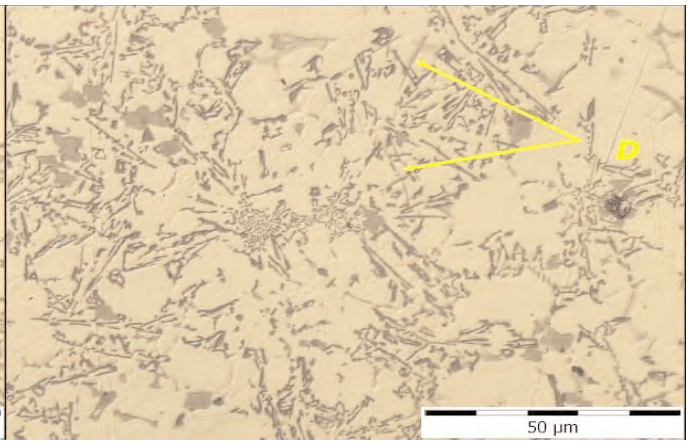

Fig. 7 — Image of phases in the metallographic sample of specimen 2
(Magnification 1000x, Nomarski DIC illumination, etching with 0,5 % HF)

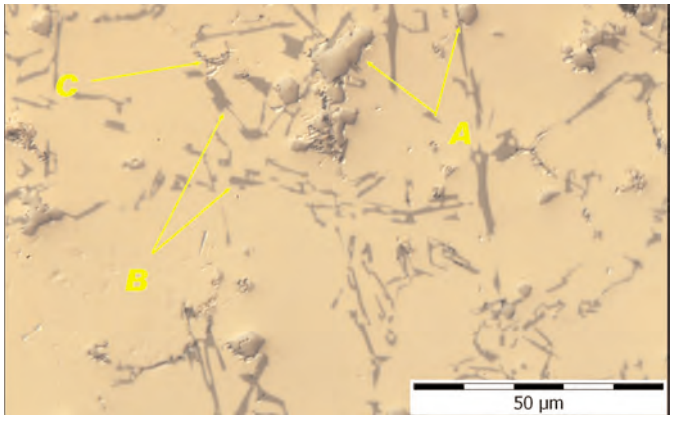

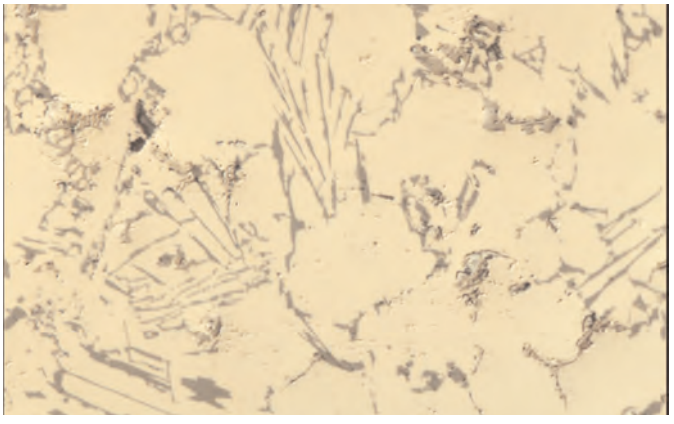

Fig. 8 — Image of phases in the metallographic sample of specimen 4
(Magnification 1000x, Nomarski DIC illumination)

Preliminary Sizing of Large Propeller Driven Aeroplanes

Předběžný výpočet rozměrů velkého vrtulového letounu

Prof. Dieter Scholz, Mihaela Niță / Hamburg University of Applied Sciences, Hamburg, Germany

Different types of aeroplanes (small / large, propeller / jet) require their own type of preliminary sizing method. One of theses methods differs only in a few but important aspects from the other. For the sake of efficient teaching of students and easy application in practice, the authors ask for the definition of a set of clearly defined step by step preliminary sizing methods. Based on the rather well known sizing method for large jet aeroplanes, the paper derives a preliminary sizing method for large propeller driven aeroplanes. In this way the paper tries to contribute to the definition of the set of methods. The sizing methods are all based on a matching chart that helps to graphically solve a two-dimensional optimization problem. The matching chart draws the optimization variable thrust-to-weight ratio (for jets) respectively power to mass ratio (propeller driven planes) versus wing loading for all basic requirements, which the aeroplane has to fulfill. The sizing method for propeller driven large aeroplanes is explained in detail and applied to a redesign study of the ATR 72. All equations are given in a form readily available for use. This requires in some cases the evaluation of proportionality factors based on aircraft statistics. Given are factors taking into account statistics for landing distance, take-off distance and maximum glide ratio for large propeller driven passenger aircraft. Furthermore, generic equations for the variation of power with altitude and speed of turboprop engines is given as well as a chart to determine the propeller efficiency.

Keywords: aircraft, design, preliminary sizing, matching chart, propeller, ATR 72, redesign.

1 Introduction

1.1 Preliminary Sizing

In literature and in practice, *aircraft development* has been repeatedly broken down into different phases. Various approaches have been followed. **Figure 1** shows one approach of dividing aircraft development into phases and shows key milestones. The development of large civil aircraft has inspired this example. Typical *aircraft design* activities take part primarily in the feasibility, concept and definition phase. *Preliminary sizing* is the first step in aircraft design and as such part of the feasibility phase, which is followed by *conceptual design* in the concept phase.

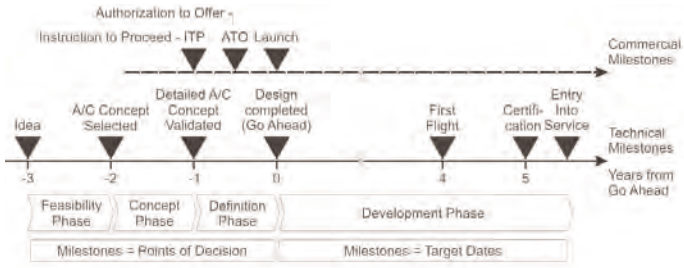

Fig. 1 — Phases of aircraft development

Preliminary sizing of an aircraft is possible without knowledge of the aircraft's geometry. In preliminary sizing the aircraft is more or less reduced to a point mass. However concrete ideas about the aircraft need to exist:

- What type of configuration will be selected?
- What aspect ratio can be expected?
- What cruise Mach number and type of propulsion system will be selected?

With these first considerations, realistic requirements can be formulated. These *requirements* (some of them depending on the certification rules — see below) will enter the preliminary sizing phase:

- Payload m_{PL} ,
- Range R,
- Mach number in cruise M_{CR} or speed V_{CR} ,
- Take-off field length s_{TOFL} ,
- Landing field length s_{LFL} , approach speed V_{APP} or stall speed V_S ,
- Climb gradient γ during second segment,
- Climb gradient γ during missed approach.

Preliminary sizing yields basic *aircraft parameters* like

- Take-off mass m_{MTO} ,
- Fuel mass m_F ,
- Operating empty mass m_{OE} ,
- Wing area S_W ,
- Take-off thrust T_{TO} or take-off power P_{TO} .

1.2 Aeroplane Categories, Propulsion System and Certification Rules

When attempting to do the preliminary sizing of a passenger aircraft, it has to be differentiated

a) the type of *propulsion system* (propeller or jet),
b) the *certification rules* for the aircraft.

The certification rules depend as much on the category and size of the aircraft as on the propulsion system. Let's differentiate these categories of aeroplanes:

1 Large jet aeroplanes are certified to CS-25 [CS-25] respectively FAR Part 25 [FAR Part 25],
2 Very light jets are certified to CS-23 [CS-23] respectively FAR Part 23 [FAR Part 23],
3 Large propeller driven aeroplanes are also certified to CS-25 respectively FAR Part 25
4 Smaller propeller driven aeroplanes (normal, utility, aerobatic and commuter aeroplanes) are certified to CS-23 respectively FAR Part 23,
5 Very light propeller driven aeroplanes (up to a maximum take-off mass of 750 kg) can be certified to CS-VLA [CS-VLA],

6 Different certification rules exist for ultra light aircraft.

1.3 Preliminary Sizing Methods

Different preliminary sizing methods are needed for the various categories of aeroplanes given in (1) through (6) above, because equally (a) and (b) have an impact on the underlying flight mechanics of the sizing problem.

Aircraft design text books or lecture notes do not always seem to present a clear step by step method for preliminary sizing. One early text book with a clear step by step method for preliminary sizing was Corning [Corning 1964]. Loftin [Loftin 1980] proposes a preliminary sizing method for large jet aeroplanes (1). Roskam [Roskam 1989], Scholz [Scholz 2008] and others base their preliminary jet sizing method on Loftin. Loftin [Loftin 1980] proposes also another method for smaller propeller driven aeroplanes (4).

What seems to be missing in the literature is a set of clearly defined step by step preliminary sizing methods for each category of aeroplane. This set of methods has to be built in such a way that the user easily understands the similarities and differences of the various methods.

Aim of this paper is to present a sizing method for large propeller driven aeroplanes (3) that follows as closely as possible the better known method for large jet aeroplanes (1) and work in this way towards the goal of a unified and complete set of sizing methods for the most important categories of civil aeroplanes.

1.4 General Approach

A *matching chart* should be at the heart of each sizing method. The matching chart helps to graphically solve a two-dimensional optimization problem. Keeping in mind that flight mechanic calculations for propellers are based on power P, whereas calculations for jets are based on thrust *T*, the two *optimization variables* as proposed here are:

a) thrust-to-weight ratio $T_{TO} / (m_{TO} \cdot g)$ respectively power to mass ratio P_{TO} / S_W

and

b) wing loading m_{MTO} / S_W .

Figure 2 shows a generic matching chart for large jet aeroplanes. From the various requirements, either the wing loading or the thrust-to-weight ratio (or a function of one versus the other) can be calculated. For all calculations it is ensured that wing loading and thrust-to-weight ratio always refer to take-off conditions, which makes it possible to compare the values of different flight phases. The results are plotted on the matching chart. The matching chart for large propeller driven airplanes only differs by putting P_{TO} / m_{TO} on the ordinate and will be explained in the main part of this paper.

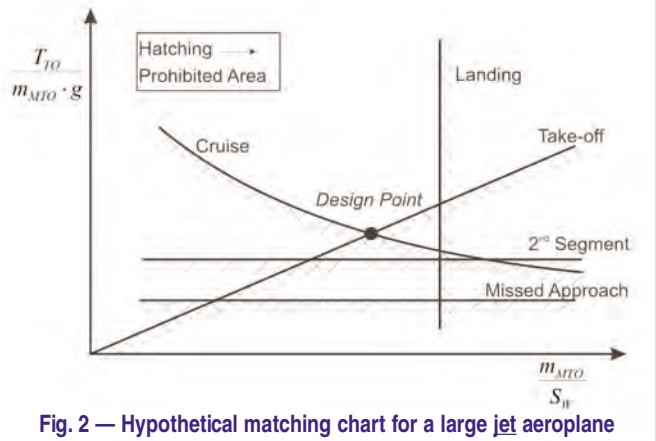

Fig. 2 — Hypothetical matching chart for a large jet aeroplane

The *aim of optimization* is to achieve the following:

- *Priority 1:*
  to achieve the smallest possible thrust-to-weight ratio (respectively power to mass ratio)
- *Priority 2:*
  to achieve the highest possible wing loading (if not other design requirements indicate to decide otherwise).

2 Overview

An overview of the proposed preliminary sizing method for large propeller driven aeroplanes is given in **Figure 3**. The blocks in the first column convert the requirements into the optimization parameters, which are power to mass ratio P_{TO} / m_{TO} and wing loading m_{TO} / S_W (shown in Figure 3 in the second column). In detail, we have:

Block 1 "LANDING FIELD LENGTH" provides a maximum value for the wing loading *m/S* (reference value: m_{TO} / S_W). The input values of the calculation are the maximum lift coefficient with flaps in the landing position $C_{L,max,L}$ as well as the landing field length S_{LFL} according to CS/FAR. The maximum lift coefficient $C_{L,max,L}$ depends on the type of high lift system and is selected from data in the literature (see textbooks and lecture notes).

Block 2 "TAKE-OFF FIELD LENGTH" provides a minimum value for the power-to-mass ratio as a function of the wing loading: $P / m = f(m / S)$ with reference value: P_{TO} / m_{MTO} . The functional connection P / m = f (m / S) is dependent on the maximum lift coefficient with flaps in the take-off position $C_{L,max,TO}$, propeller efficiency η_p and the take-off field length s_{TOFL}. The maximum lift coefficient $C_{L,max,TO}$ is selected with the aid of data in the literature. In a first attempt it is often assumed that $C_{L,max,TO}$ is 80% of $C_{L,max,L}$.

Block 3 examines the "SECOND SEGMENT CLIMB GRADIENT" and **Block 4** the "MISSED APPROACH CLIMB GRADIENT". The blocks provide minimum values for the power-to-mass ratio P / m. The input value for the calculations: the lift-to-drag ratio L / D and the propeller efficiency η_p. L / D is estimated on the basis of a simple approximation calculation.

Block 5 "CRUISE MATCHING ANALYSIS" represents the cruise analysis that provides a minimum value for the power-to-mass ratio as a function of the wing loading: $P / m = f(m / S)$. The power-to-mass ratio thus determined is sufficient to facilitate a stationary straight flight with the assumed cruise Mach number M_{CR} or cruise speed V_{CR} for the respective wing loading. The calculation is carried out for the design lift coefficient $C_{L,DESIGN}$. The cruise altitude is also obtained from the cruise analysis. Input values are the lift-to-drag ratio $E = L / D$ during cruise, the assumed cruise Mach number $M = M_{CR}$ or speed $V = V_{CR}$, engine and propeller characteristics and the characteristics of the atmosphere.

The output values of the blocks in the first column of Figure 3 provide a set of relationships between the power-to-mass ratio

and the wing loading. Taken together, these relationships give, in a "SIMULTANEOUS SOLUTION" (**Blocks 6**) a single pair of values: power-to-mass ratio and wing loading (P / m; m / S) (**Block 7**) that meets all requirements and constraints in an economical manner.

Blocks 8 and 9 stand for "WEIGHT ANALYSIS". The relative operating empty mass m_{OE} / m_{MTO} or the relative useful load u are estimated. m_{MTO} is the maximum take-off mass. The relative useful load is defined as

$$u = \frac{m_F + m_{PL}}{m_{MTO}} = 1 - \frac{m_{OE}}{m_{MTO}}$$

Various methods exist in the literature for estimating m_{OE} / m_{MTO} or u. For propeller driven aeroplanes, the power-to-mass ratio (from Block 7) could be used as an input value for a mass estimate according to statistics.

In **Block 11** "RANGE EQUATION" yields the relative fuel mass m_F / m_{MTO} (**Block 10**) which is calculated, using the "Breguet Range Equation" for propeller aircraft, based on the "RANGE REQUIREMENT" (**Block 12**). Other input values are the assumed cruise Mach number M / M_{CR} or cruise speed V / V_{CR}, the lift-to-drag ratio during cruising $E = L / D$, the specific fuel consumption $c = SFC_{CR}$ and the propeller efficiency η_p during cruise.

In **Block 14** maximum take-off mass m_{MTO} is calculated from relative useful load u, relative fuel mass m_F / m_{MTO} and the payload requirement m_{PL} (**Block 13**). With the maximum take-off mass m_{MTO} the necessary *take-off power* $P = P_{TO}$ and the *wing area* $S = S_W$ can then be calculated in **Block 15** from power-to-mass ratio P / m and wing loading m / S.

3 Optimization Parameters from Requirements

Optimization parameters are power to mass ratio P_{TO} / m_{TO} and wing loading m_{TO} / S_W. The requirements are specified for the various phases of flight.

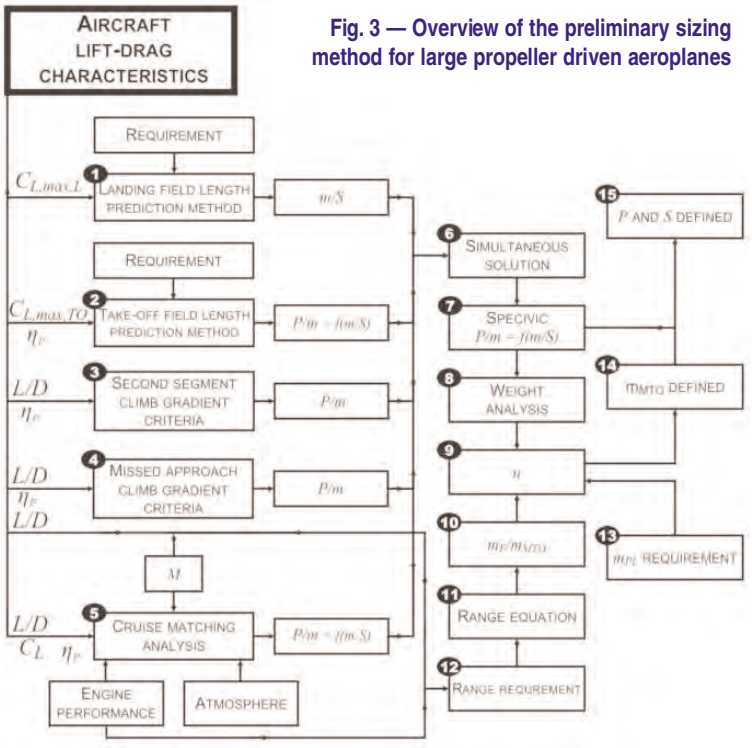

Fig. 3 — Overview of the preliminary sizing method for large propeller driven aeroplanes

3.1 Approach Speed

The landing requirements can be stated in terms of approach speed V_{APP} or landing field length s_{LFL}. Assuming similar braking characteristics of the aircraft of one category, statements of either approach speed or landing field length are equivalent ones. Based on statistics one statement can be transformed in the other:

$$s_{LFL} = \left(\frac{V_{APP}}{k_{APP}} \right)^2$$

The proportionality factor was evaluated (see **Figure 4**) from data selected for this category of large passenger turboprop aircraft:

$$k_{APP} = 1.64 \sqrt{\frac{\mathrm{m}}{\mathrm{s}^2}}$$

It also would have been possible to calculate k_{APP} from k_L (see Subsection 3.2 for k_L)

$$k_{APP} = \sqrt{\frac{2g \cdot 1.3^2}{\rho_0} k_L} = 5.20 \sqrt{k_L}$$

to yield a better value for large passenger turboprop aircraft:

$$k_{APP} = 1.93 \sqrt{\frac{\mathrm{m}}{\mathrm{s}^2}} .$$

The two approaches do not result in exactly the same value because the evaluation was based on different aircraft data. Experience shows that reported values for approach speed are often not given accurately and do not always refer to the $V_{APP} = 1.3\ V_S$ reference speed. For this reason, better results can be obtained when using landing distance data. In comparison, large passenger jets [7], [9]:

$$k_{APP} = 1.70 \sqrt{\frac{\mathrm{m}}{\mathrm{s}^2}} .$$

Based on the latter two values for k_{APP}, turboprop aircraft achieve a shorter landing field length at the same approach speed (by a factor of 1.29). This is due to the their better reverse thrust capabilities, which in turn also resulted in a lower safety factor in the determination of landing field length from landing distance for turboprop aircraft: 1/0.7 = 1.429 for turboprop aircraft versus 1/0.6 = 1.667 for jets [1]. The turboprop advantage comes out as 1.667/1.429 = 1.167 which is about the ratio that resulted from aircraft data.

3.2 Landing Field Length

Landing field length yields the optimization parameter wing loading

$$m_{MTO} / S_W \le \frac{k_L \cdot \sigma \cdot C_{L,max,L} \cdot s_{LFL}}{m_{ML} / m_{MTO}} .$$

The proportionality factor was evaluated (see **Figure 5**) from data selected for this category of large passenger turboprop aircraft:

$$k_L = 0.137 \frac{\mathrm{kg}}{\mathrm{m}^3} .$$

In comparison, large passenger jets [7], [9]:

$$k_L = 0.107 \frac{\mathrm{kg}}{\mathrm{m}^3}$$

have a lower value than the 0.137 kg/m³ from above, which means that turboprop aircraft on ave-

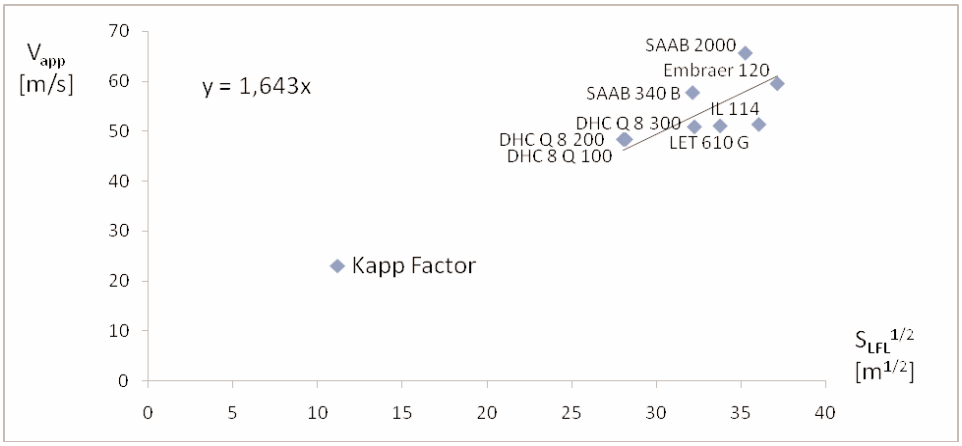

Fig. 4 — Statistical factor k_{APP} for approach speed calculation from landing field length for turboprop aircraft

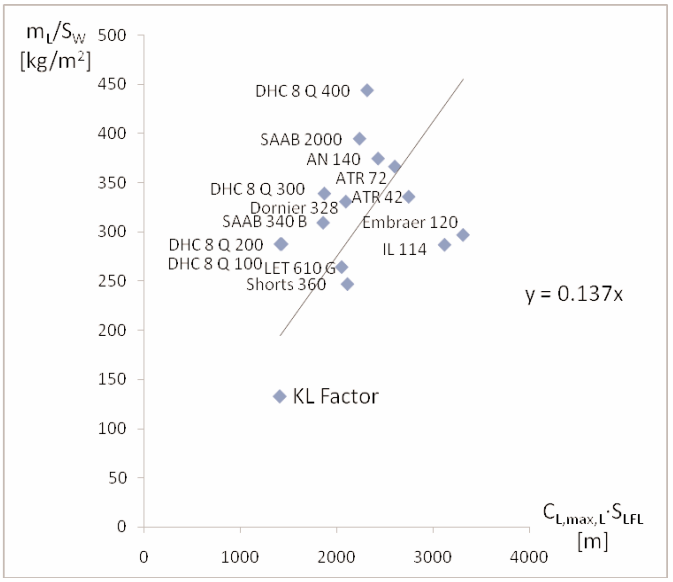

Fig. 5 — Statistical factor k_L for calculating wing loading from landing field length and maximum lift coefficient upon landing for turboprop aircraft

rage achieve a shorter landing field length with the same wing loading.

$$\sigma = \frac{\rho}{\rho_0} = \frac{288.15\,\mathrm{K}}{288.15\,\mathrm{K} + \Delta T_L}$$

is the density ratio. σ differs from unity, if landing requirements have to be met at a high (or lower) temperature than following from International Standard Atmosphere (ISA) at Mean Sea Level (MSL).

m_{ML} / m_{MTO} has to be selected. It may not be too low, otherwise fuel reserves or remaining fuel upon landing due to favorable flight conditions could result in a landing mass greater than maximum landing mass $m_L > m_{ML}$ that is clearly not permissible. Typical values for large propeller driven aeroplanes are in the range between 0.95 and 1.00. On average a value of 0.97 may be selected. These aircraft are short range aircraft. For this reason the value is always very close to 1.0.

3.3 Take-Off Field Length

Take-off field length yields a fixed ratio between the optimization parameters power to mass and wing loading. In the matching chart this forms a straight line through the origin.

$$\frac{P_{TO} / m_{MTO}}{m_{MTO} / S_W} \geq \frac{k_{TO} \cdot V \cdot g}{s_{TOFL} \cdot \sigma \cdot C_{L,max,TO} \cdot \eta_{P,TO}} .$$

The proportionality factor was evaluated (see **Figure 6**) from data selected for this category of large passenger turboprop aircraft:

$$k_{TO} = 2.25\,\frac{\mathrm{m}^3}{\mathrm{kg}}$$

In comparison, large passenger jets [7], [9]:

$$k_{TO} = 2.34\,\frac{\mathrm{m}^3}{\mathrm{kg}}$$

have practically the same value.

The speed V is the average speed during take-off. Averaging is done with respect to dynamic pressure which yields

$$V = V_2 / \sqrt{2} .$$

V_2 is the take-off safety speed that has to be reached at the end of the take-off distance. It is usually taken as

$$V_2 = 1.2\,V_{S,TO} .$$

New amendments of CS-25 [1] also indicate the possibility to set V_2 as low as

$$V_2 = 1.13\,V_{S,TO} .$$

Take-off stall speed depends on flap setting and hence selected lift coefficient. Making a connection to high lift capabilities during landing, we get

$$V_{S,TO} = V_{S,L} \sqrt{\frac{C_{L,\max}}{C_{TO,\max}}} .$$

Older aircraft were designed to

$$V_{APP} = 1.3\,V_{S,L} .$$

New amendments of CS-25 [1] also indicate the possibility to set V_{APP} as low as

$$V_{APP} = 1.23\,V_{S,L} .$$

So

$$V_{S,L} = \frac{V_{APP}}{1.3} \text{ or } V_{S,L} = \frac{V_{APP}}{1.23}$$

$$V_{APP} = k_{APP} \cdot \sqrt{S_{LFL}}$$

$$\sigma = \frac{\rho}{\rho_0} = \frac{288.15\,\mathrm{K}}{288.15\,\mathrm{K} + \Delta T_{TO}}$$

The propeller efficiency $\eta_{P,TO}$ for take-off is obtained from **Figure 7** for the average speed V (see above) and a disc loading

$$L = \frac{P_{TO}}{\sigma\, \rho_0\, S_D}$$

calculated from take-off power, density and disc area. During the first run of the sizing program the take-off power is not known. Instead a propeller efficiency is merely estimated from Figure 7. In a second iteration applying the sizing method, the take-off power from Block 15 can be used for a better estimate of the propeller efficiency with the help of Figure 7. At this point we should also be more specific about was is meant here with engine power: The power indicated is always the shaft power $P = P_S$ and $P_{TO} = P_{S,TO}$.

3.4 Climb Rate during 2nd Segment

2nd segment climb rate yields the optimization parameter power to mass

$$\frac{P_{TO}}{m_{MTO}} \geq \frac{n_E}{n_E - 1} \cdot \left(\frac{1}{E} + \sin\gamma \right) \cdot \left(\frac{V_2 \cdot g}{\eta_{P,CL}} \right) .$$

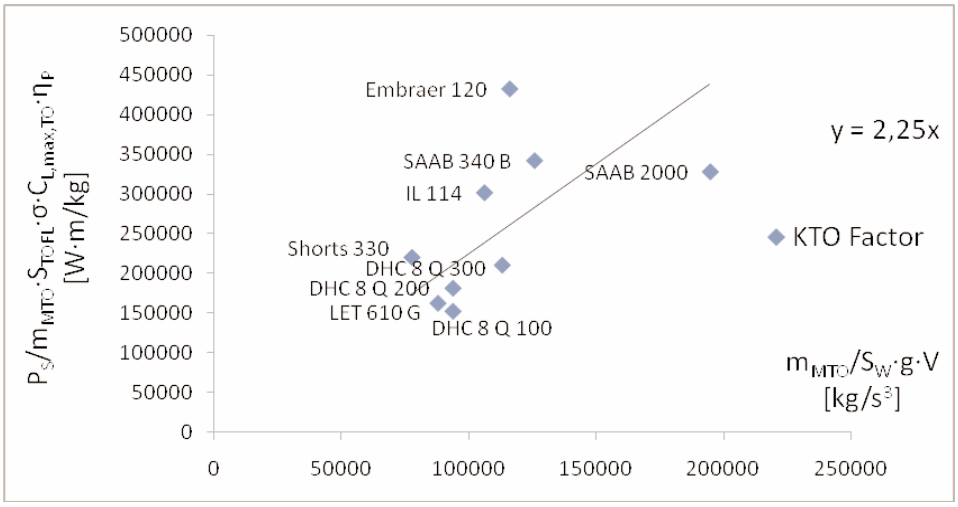

Fig. 6 — Statistical factor k_{TO} for calculating the take-off optimization parameter from take-off field length and maximum lift coefficient upon take-off for turboprop aircraft

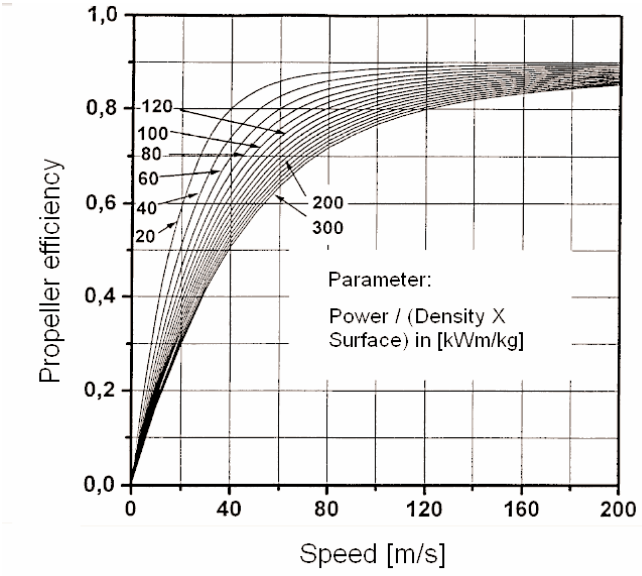

Fig. 7 — Propeller efficiency for variable pitch propellers as a function of aircraft speed and disc loading (the reference surface area is the propeller disc area). Adapted from [10]

n_E stands for the number of engines. $E = L/D$ is the glide ratio during take-off estimated from aspect ratio A, Oswald factor e:

$$E = \frac{C_L}{C_D} = \frac{C_L}{C_{D,P} + \frac{C_L^2}{\pi \cdot A \cdot e}}, \quad C_{D,P} = 0.05 C_L - 0.035 \text{ (for } C_L \geq 1.1), \quad e = 0.7, \quad C_L = \frac{C_{L,\max,TO}}{1.2^2}.$$

The climb rate (sin γ) is given in [1]: "The steady gradient of climb may not be less than 2.4% for two-engined aeroplanes, 2.7% for three-engined aeroplanes and 3.0% for four-engined aeroplanes."

V_2 and $\eta_{P,CL}$ from Section 3.3. $\eta_{P,CL}$ is calculated with a speed V_2 . Note correct propeller efficiency calculation requires iteration.

3.5 Climb Rate during Missed Approach

Missed approach climb rate puts once again a boundary condition on the optimization parameter power to mass

$$\frac{P_{TO}}{m_{MTO}} \geq \frac{n_E}{n_E - 1} \cdot \left(\frac{1}{E} + \sin\gamma \right) \cdot \left(\frac{V_{APP} \cdot g}{\eta_{P,L}} \right) \cdot \left(\frac{m_{ML}}{m_{MTO}} \right) \cdot$$

This time the estimate for $E = L/D$ is done with

$$E = \frac{C_L}{C_D} = \frac{C_L}{C_{D,P} + \frac{C_L^2}{\pi \cdot A \cdot e}},$$

$C_{D,P} = 0.05 C_L - 0.035$ (for $C_L \geq 1.1$), $e = 0.7$, $C_L = \frac{C_{L,\max,L}}{1.3^2}$

$\Delta C_{D,gear} = 0$ for [1] and

$\Delta C_{D,gear} = 0.015...0.020$ for [2].

The climb rate (sin γ) is given in [1]: "The steady gradient of climb may not be less than 2.1% for two-engined aeroplanes, 2.4% for three-engined aeroplanes and 2.7% for four-engined aeroplanes."

V_{APP} is taken from Section 3.3. m_{ML}/m_{MTO} is taken from Section 3.2. $\eta_{P,L}$ from Section 3.3, calculated with a speed V_{APP}. Note correct propeller efficiency calculation requires iteration.

3.6 Cruise

Cruise matching is based on the assumption of steady state straight flight. From the requirement of a certain cruise speed V_{CR} or cruise Mach number M_{CR}, the power to mass ratio and the wing loading are determined. In order to achieve this, two equations can be used: *Lift = Weight* and *Drag = Thrust*. Thrust will be replaced by power in the last equation. Both equations include atmospheric and/or engine parameters that are a function of cruise altitude. Since cruise altitude is not known when starting the sizing method, the power to mass ratio and the wing loading are calculated for a range of possible cruise altitudes. Data from this table is later drawn into the matching chart and stays for the cruise requirement.

3.6.1 Lift = Weight

$$\frac{m_{MTO}}{S_W} = \frac{C_L \cdot M_{CR}^2}{g} \cdot \frac{\gamma}{2} \cdot p(H)$$

or

$$\frac{m_{MTO}}{S_W} = \frac{C_L \cdot \rho_0 \cdot V_{CR}^2 \cdot \sigma(H)}{2 \cdot g}.$$

It is $C_L / C_{L,md} = 1/(V/V_{md})^2$, so the lift coefficient in cruise follows from $C_L = \frac{C_{L,md}}{(V/V_{md})^2}$,

with $C_{L,md} = \frac{\pi A e}{2E_{\max}}$.

V / V_{md} is an input parameter to the sizing method to help match the cruise performance. Maxim glide ratio E_{max} from Section 3.6.3. $\sigma(H)$ is the relative density from the ISA, $\rho_0 = 1.225$ kg/m³ is the density of the air at MSL from ISA. $\gamma = 1.4$ is the ratio of specific heats.

3.6.2 Drag = Thrust

$$\frac{P_{TO}}{m_{MTO}} = \frac{M_{CR} \cdot a(H) \cdot g}{P_{CR}/P_{TO} \cdot E \cdot \eta_{P,CR}}$$

or

$$\frac{P_{TO}}{m_{MTO}} = \frac{V_{CR} \cdot g}{P_{CR}/P_{TO} \cdot E \cdot \eta_{P,CR}}$$

$$E = \frac{2E_{\max}}{\frac{1}{\left(\frac{C_L}{C_{L,md}}\right)} + \left(\frac{C_L}{C_{L,md}}\right)}$$

with $C_L / C_{L,md} = 1/(V / V_{md})^2$.

V / V_{md} is an input parameter to the sizing method to help match the cruise performance. η_{PCR} from Section 3.3, E from Section 3.6.3, P_{CR} / P_{TO} from Section 3.6.4. $a(H)$ is the speed of sound from the ISA.

Author	Ref.Nr.	Page	Engine	A	m	n
Schaufele	[14]	187	generic	1.036	0.101	0.851
Brüning	[15]	58	T 64-GE-7	1.121	0.168	0.755
Russel	[16]	16	Rolls-Royce	1.725	0.267	0.966
Loftin	[7]	375	generic	1.089	0.091	0.924
McCormick & Barnes	[17]	351	PW 120	1.883	0.740	0.929
Average				1.371	0.273	0.885

Tab. 1: Parameters A, m and n to calculate the relative amount of engine shaft power P_{CR} / P_{TO} as a function of altitude (expressed by σ) and Mach number M

3.6.3 Maximum Glide Ratio Estimation

Maximum glide ratio $E_{max} = (L / D)_{max}$ is estimated from aspect ratio A and wetted area S_{wet}. The ratio S_{wet} / S_{wet} for large turboprop aeroplanes is between 5 and 7 with an average at about 6.2.

$$E_{max} = k_E \cdot \sqrt{\frac{A}{S_{wet} / S_W}}$$

The proportionality factor was evaluated (see **Figure 8**) based on data from [11] for this category of

large passenger turboprop aircraft: $k_E = 11.22$.

In comparison [9],

large passenger jets, long range: $k_E = 17.25$,
large passenger jets, medium range: $k_E = 16.19$,
large passenger jets, short range: $k_E = 15.15$.

It can be determined that statistically, the maximum lift coefficient (at the same aspect ratio and wetted area ratio) is smaller for aircraft with smaller range. Since the turboprop aircraft offer usually a smaller range than jets their maximum glide ratio is smaller (does not need to be that high).

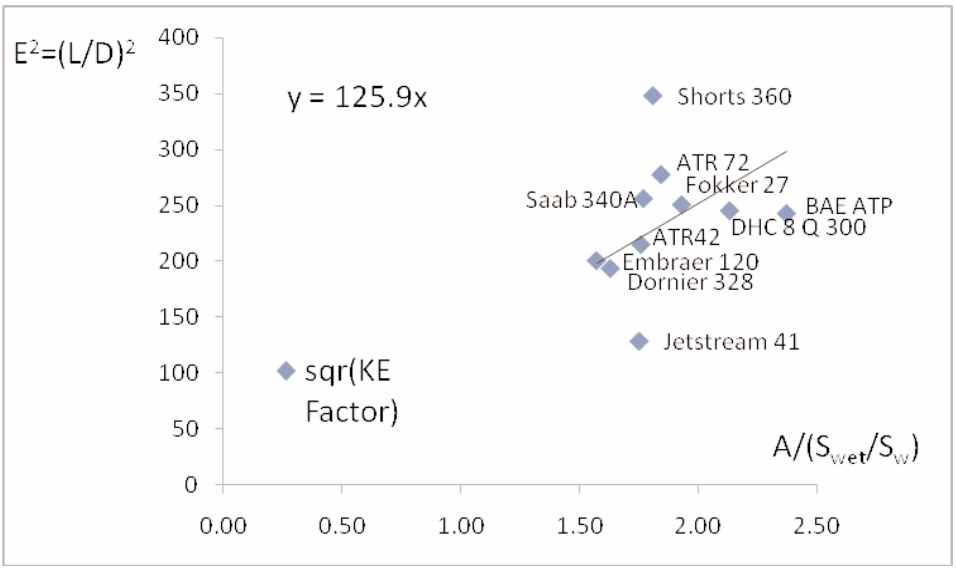

Fig. 8 — Statistical factor k_E for calculating the maximum glide ratio E_{max}, for turboprop aircraft based on data from [11]

3.6.4 Engine Power Estimation

In Section 3.6.2 the ratio P_{CR} / P_{TO} is used. This is the relative amount of engine shaft power left at altitude and at a certain aircraft speed. Since the sizing method should be a generic one, a data sheet that applies only for one specific engine may not be so helpful. For this reason, different sources with specific and generic engine performance data where studied in [13]. Furthermore, published equations to calculate P_{CR} / P_{TO} were investigated and fitted to the available data. As a result of the investigation an equation was recommended for use:

$P / P_0 = AM^m\sigma^n$ with parameters A, m and n from **Table 1**.

4 Combining Results

Values of optimization parameters are drawn in the matching chart. An example is given in Section 5. The design point is found as explained in Section 2. The rest of the sizing process is straight forward and does not differ much from that process for large jet aeroplanes (see [9]).

The required fuel mass is calculated using fuel fractions. Fuel reserves have to be included. Domestic and international flights are distinguished. For turboprop aeroplanes usually domestic reserves apply. The additional distance for the flight to an alternate, which is normally assumed to be 200 NM for larger jets, may also be selected as a shorter distance for turboprops that are not so big. Reserve loiter time is 45 minutes.

As in all other sizing processes, it is important to make a clear statement about the payload range requirements. Payload and range must from a pair of values in the payload range diagram (not any payload combined with any range). The fuel reserves and the cruise speed must be clearly stated together with the payload range requirements.

The fuel fractions for cruise flight, flight to the alternate and for loiter has in this sizing process to be based on the range equations for propeller aircraft. The Breguet factor for propeller aircraft

$$B_s = \frac{E \cdot \eta_P}{SFC \cdot g}$$

is used to calculate the segment fuel fraction for the cruise flight phase

$$\frac{m_{LOI}}{m_{CR}} = e^{-\frac{s_{CR}}{B_s}}.$$

s_{CR} is the distance flown in cruise. If the distance to the alternate and the distance covered during loiter is added, no other equation is needed. Other segment fuel fractions (e.g. for take-off and landing) may be taken from tables [8]. All segment fuel fractions combined yield relative fuel mass m_F / m_{MTO}. Maximum take-off mass is finally calculated from

$$m_{MTO} = \frac{m_{PL}}{1 - \frac{m_F}{m_{MTO}} - \frac{m_{OE}}{m_{MTO}}}.$$

5 Example Calculation: ATR 72

The sizing method was put to a test with the redesign of an ATR 72. The requirements for the sizing task were taken from the manufacturers web page.

Landing:	S_{LFL} = 1067 m
Take off:	S_{TOFL} = 1290 m
2nd Segment:	$n_E = 2$ $\gamma = 0.024$
Missed Approach:	$n_E = 2$ $\gamma = 0.021$
Cruise:	$M = 0.41$
Range:	R = 715 NM
Payload:	m_{PL} = 6460 kg

Cruise altitude, determined from the design point: H_{CR} = 3888 m.

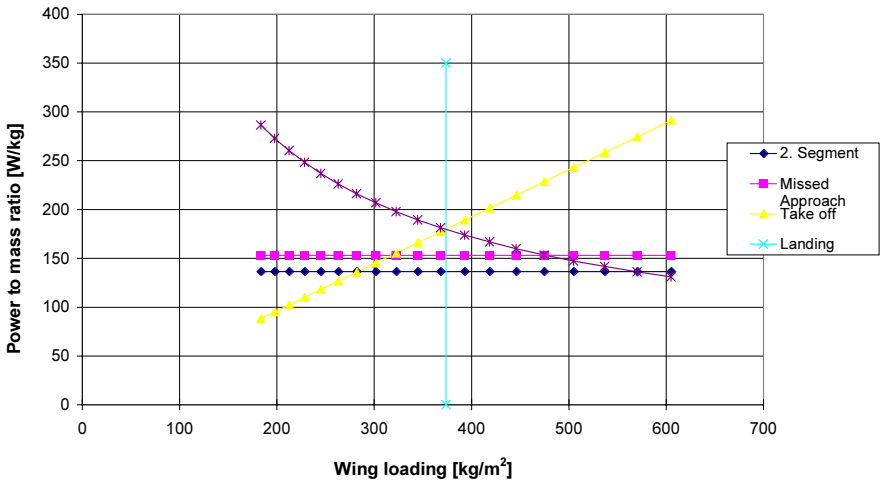

Fig, 9 — Matching chart for the sizing process of the ATR 72

6 Conclusion

A preliminary sizing method for turboprop aeroplanes was presented. The method includes — where necessary — equations based on aircraft statistics. The preliminary sizing method was tested with a redesign task of an ATR 72. The redesign with the proposed method was possible with only minor difference between the respective ATR value from the redesign case and the original ATR 72 value.

Flight Phase	$C_{L,max}$	C_L	E_{max}	E	η_P
Landing	2.5				
Take-off	2.1				0.64
2nd Segment		1.46		12.28	0.73
Missed Approach		1.48		10.79	0.73
Cruise		0.503	15.74	12.49	0.86

Tab. 2: Results from the redesign sizing process of an ATR 72 — Aerodynamic parameters and propeller efficiency

Parameter	Original ATR 72	Redesigned ATR 72	Difference
m_{MTO} [kg]	22800	22925	0.5%
m_L [kg]	22350	22466	0.5%
m_{OE} [kg]	12950	13021	0.5%
S_W [m²]	61	61.35	0.6%
b [m]	27.05	27.13	0.3%
P_{TO} (one engine) [kW]	2051	2061	0.5%
m_{MTO}/S_W [kg/m²]	373.8	373.7	0.0%
P_{TO}/m_{MTO} [W/kg]	179.9	179.8	-0.1%

Tab. 3: Results from the redesign sizing process of an ATR 72: Mass, wing area, power

References:

[1] European Aviation Safety Agency: *Certification Specifications for Large Aeroplanes*, CS25, Amendment 4, 27 December 2007, http://www.easa.eu.int

[2] U.S. Department for Transportation, Federal Aviation Administration: *Federal Aviation Regulations, Part 25, Transport Category Airplanes*, 2007, http://www.faa.gov

[3] European Aviation Safety Agency: *Certification Specifications for Normal, Utility, Aerobatic, and Commuter Category Aeroplanes*, CS23, Decision 2003/14/RM, 14 November 2003, http://www.easa.eu.int

[4] U.S. Department for Transportation, Federal Aviation Administration: *Federal Aviation Regulations, Part 23, Normal, Utility, Aerobatic and Commuter Category Airplanes*, 2007, http://www.faa.gov

[5] European Aviation Safety Agency: *Certification Specifications for Very Light Aeroplanes*, CS-VLA, Decision No. 2003/18/RM, 14 November 2003, http://www.easa.eu.int

[6] Corning, G.: *Supersonic and Subsonic Airplane Design*; Published by Corning, G., 1964

[7] Loftin, L.K.: *Subsonic Aircraft: Evolution and the Matching of Size to Performance*; NASA Reference Publication 1060, 1980

[8] Roskam, J.: *Airplane Design. Vol. 1: Preliminary Sizing of Airplanes*; Ottawa, Kansas, 1989, http://www.darcorp.com — Sale: Analysis and Research Corporation, 120 East Ninth Street, Suite 2, Lawrence, Kansas, 66044, USA.

[9] Scholz, D.: *Short Course, Aircraft Design*; Hamburg University of Applied Sciences, May 2008, http://www.flugzeugentwurf.de

Room for Your Notes

Unmanned Aircraft Structural Model and its FEM Analysis for Strength Evaluation

Colour illustrations to the article published on pages 14 to 18.

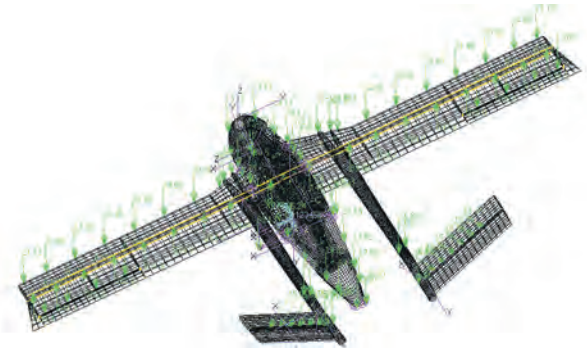

Fig. 13a — A scheme of the model equivalent load in the form of the focused forces in the D-reference point of the flight envelope

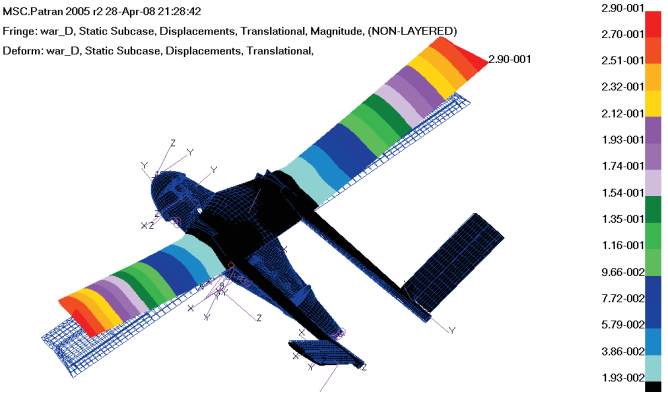

Fig. 13b — Distribution of the node displacements after static analysis for the D-case: maximum displacement u_{max}= 290 mm

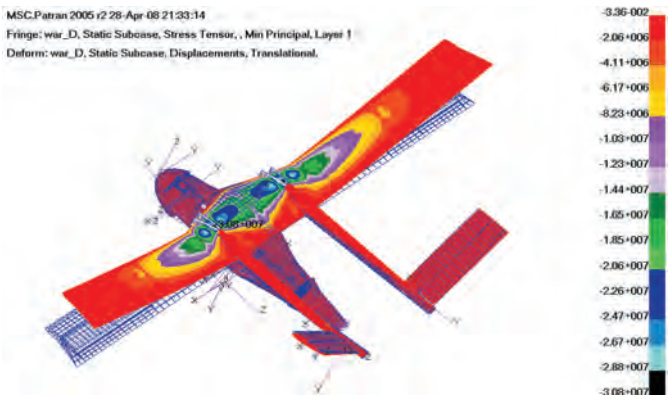

Fig. 13c — A distribution of the main stress after static analysis for the D-case: extreme stress σ_{min}= -30.8 MPa

Fig. 13d — Distribution of the primary stresses after static analysis for the D-case: extreme stress σ_{max}= 36.6 MPa

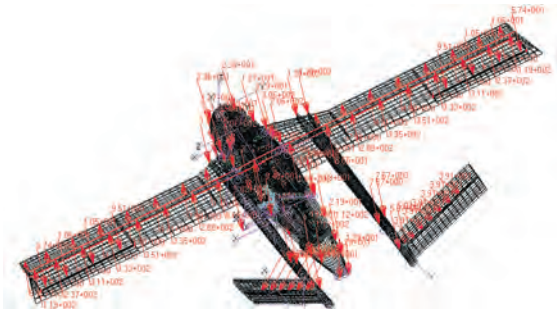

Fig. 14a — Unmaned Aircraft Structural Model and its FEM Analysis for Strength Evaluation

Fig. 14b — Distribution of the node displacements after static analysis for the C-case: u_{max}= 362 mm

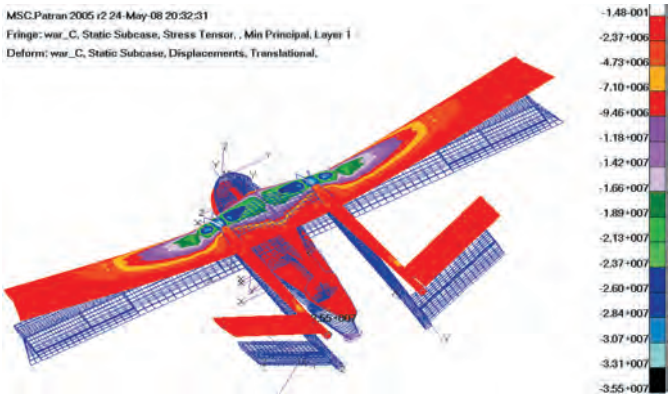

Fig. 14c — A distribution of the main stress after static analysis for the C-case: extreme stress σ_{min}= -35.5 MPa

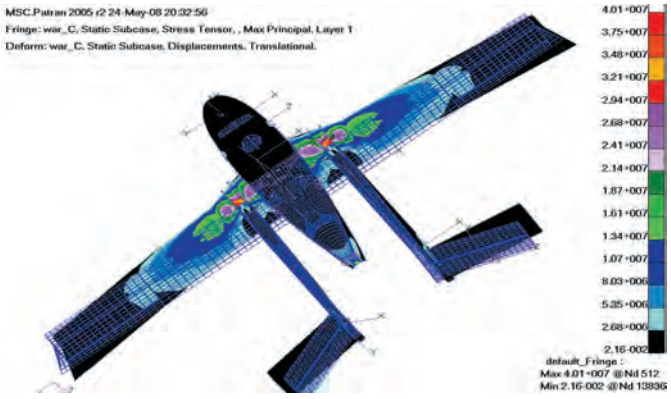

Fig. 14d — Distribution of the primary stresses after static analysis for the C-case: extreme stress σ_{max}= 40.1 MPa

Calculation of Temperature Fields of Vibrating Composite Parts

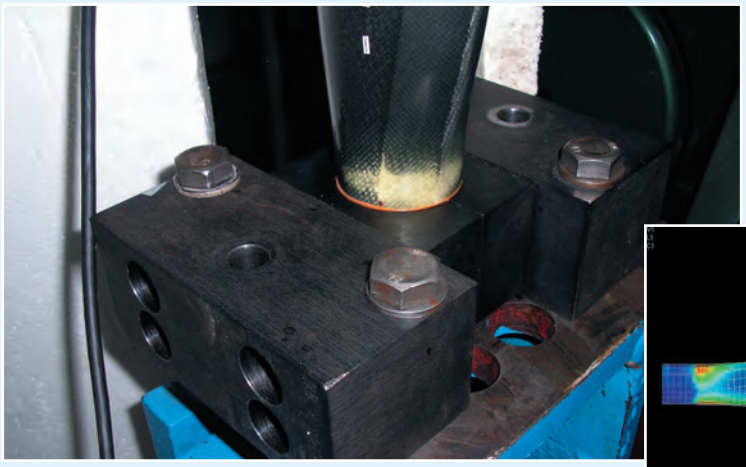

(Left) Damage of composite blade caused by intensive vibrations and consequently by overheating

(Below) FEM analysis predicts the same failure caused by overheating

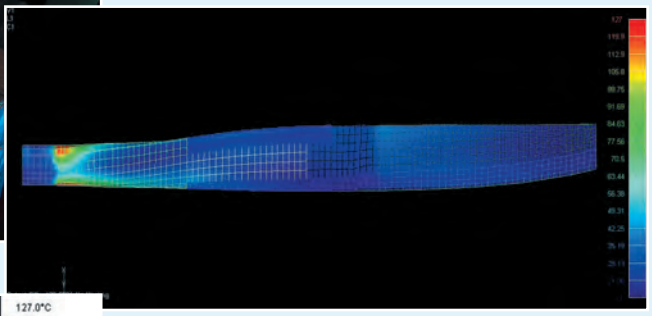

(Left) Infrared image of overheating of composite blade caused by intensive vibrations

(Below) The location of overheating corresponds to the location of matrix failure

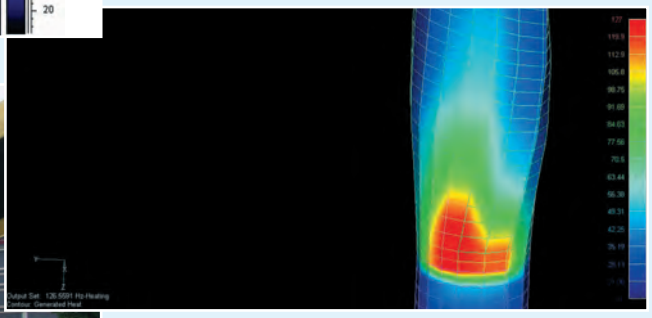

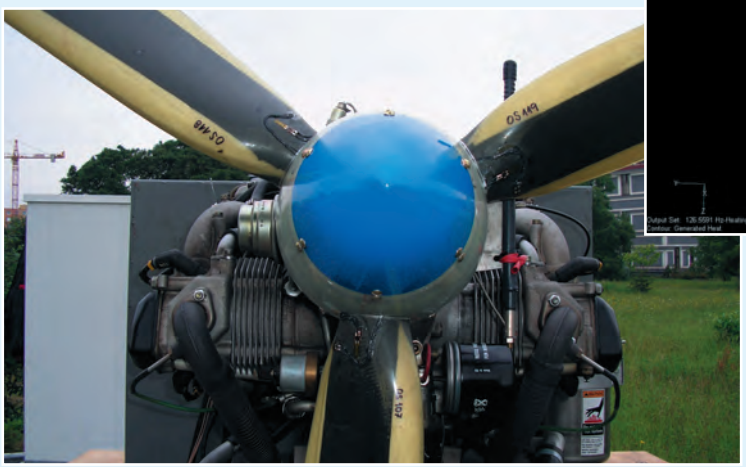

(Left) Strain-gauging of composite blade root section gives important information about stresses and vibration levels

The whole view of the mobile test bed of composite propellers is depicted on title page